

Investigating the performance and behaviour of porous silicon energetic materials

by

Andrew Mark Plummer

*Thesis
Submitted to Flinders University
for the degree of*

Doctor of Philosophy
College of Science and Engineering
November 2017



Approximately 20 mg of porous silicon loaded with sodium perchlorate, initiated using a high voltage spark.

There can be no rainbows without a cloud and a storm.

John Heyl Vincent 1832-1920

CONTENTS

Contents	iii
Abstract	vi
Declaration	ix
Acknowledgments	x
List of figures	xii
List of tables	xvi
List of publications	xvii
Glossary of terms	xviii
Chapter 1 A review of porous silicon energetic materials, their formation, properties and behaviour.	1
1.1 Introduction	2
1.2 Porous silicon formation	2
1.2.1 General aspects of porous silicon etching.....	2
1.2.2 Characterisation of porous silicon surfaces	9
1.2.3 The surface structure of fresh and aged porous silicon.....	10
1.3 Explosives and energetic materials – a general discussion.....	11
1.4 Porous silicon energetic materials	15
1.4.1 The benefits of using porous silicon as the basis for an energetic material.....	15
1.4.2 Porous silicon energetic materials	16
1.4.3 Applications of porous silicon energetic materials	45
1.5 Summary	48
1.6 Aims and scope of Thesis	50
Chapter 2 Experimental techniques.....	51
2.1 Manufacture and characterisation of porous silicon	52
2.1.1 Etching.....	52
2.1.2 Porosity measurement.....	54
2.1.3 Pore size measurement.....	54
2.1.4 Porous layer depth measurement	55
2.1.5 Optimisation of the etching process	56

2.2	Loading of oxidising agents into pSi	61
2.3	Safety relating to handling of manufactured energetic materials	62
Chapter 3	The burning rate of porous silicon energetic materials	65
3.1	Introduction	66
3.2	Materials and experimental methods.....	67
3.2.1	Sample initiation and burning rate measurement.....	68
3.2.2	Oxidising agent distribution	70
3.3	Results and discussion.....	71
3.3.1	Effect of porosity	71
3.3.2	Effect of film thickness	74
3.3.3	Effect of various oxidising agents.....	78
3.3.4	High speed video analysis	82
3.3.5	Distribution of oxidising agents within pSi.....	87
3.4	Conclusions	93
3.5	This Chapter in context with subsequent research.....	95
Chapter 4	Sensitiveness of porous silicon energetic materials	99
4.1	Introduction	100
4.2	Materials and experimental methods.....	102
4.2.1	Porous silicon preparation	102
4.2.2	Loading of oxidant into pSi.....	102
4.2.3	Sensitiveness testing	103
4.3	Results and discussion.....	105
4.3.1	Initial sensitiveness screening	105
4.3.2	Instrumented sensitiveness testing	106
4.4	Conclusions	109
Chapter 5	Laser shock ignition of porous silicon energetic materials	111
5.1	Introduction	112
5.2	Materials and experimental methods.....	115
5.2.1	Porous silicon preparation	115
5.2.2	Photon Doppler Velocimeter	115
5.2.3	Laser shock generation.....	117
5.3	Results and discussion.....	122
5.3.1	Laser shock initiation.....	122

5.3.2	Shock wave characterisation.....	126
5.4	Conclusions	132
Chapter 6	Thermal analysis of porous silicon energetic materials	134
6.1	Introduction	135
6.2	Materials and methods	139
6.2.1	Porous silicon preparation	139
6.2.2	Thermal analysis.....	140
6.2.3	Spectroscopic analysis.....	140
6.3	Results and discussion.....	143
6.3.1	Thermal behaviour of blank pSi	146
6.3.2	Decomposition and reaction of pSi / SP energetic materials.....	148
6.3.3	Decomposition and reaction of pSi / PFPE energetic materials.....	150
6.4	Conclusions	152
Chapter 7	Conclusions.....	155
7.1	Future directions and opportunities	158
Bibliography	162
Appendix A.	Calculation of pore size distribution from SEM images	173
Appendix B.	Detailed correlation between DSC and 2D FTIR data.....	175

ABSTRACT

Nanoporous structures etched into silicon wafers possess versatile and predictable morphology at nanometer scales. Loading these pore structures with an oxidising agent in a suitable carrier solvent forms an intimate fuel / oxidiser mixture able to react explosively with only minor initiating stimuli. Here, porous silicon (pSi) is formed through the electrochemical etching of mildly doped p-type wafers to form highly branched pore networks in the 3-5 nm pore size range, leaving the overall bulk dimensions of the wafer unchanged. The porosity, pore size and layer thickness are easily controlled through selection of etching parameters.

Burning rates of the system were found to be dependent on the choice of oxidising agent, porosity, layer thickness and degree of confinement. Sodium perchlorate demonstrated burning rates as high as $\approx 500 \text{ m.s}^{-1}$ - other nitrate and perchlorate oxidising agents were shown to be suitable alternatives albeit with decreased burning rates. Perfluorinated compounds, notably perfluoropolyether (PFPE), were also considered as viable alternatives to sodium perchlorate.

Analysis of the flame profile by high-speed video is also presented, suggesting that the reaction type is a deflagration rather than a detonation. A strong plume of flame is emitted from the surface, indicating the potential for this material to perform useful work either as an initiator or as a propellant. Erratic burning rates were revealed to be due to material factors associated with the brittleness of the porous silicon, with fissures generated along which the advancing flame could jet.

pSi energetic materials were revealed to be as sensitive as comparable primary explosives. Loaded with sodium perchlorate, pSi was exceedingly sensitive, recording sensitiveness to initiation below the limit of detection for impact, friction and electrostatic discharge. However, the same system loaded with PFPE was insensitive to initiation by friction, yet remained extremely sensitive to impact or electrostatic discharge.

Infrared laser pulses could initiate pSi loaded with sodium perchlorate via either laser thermal ignition or laser-generated shock waves. Using Photon Doppler Velocimetry, it was determined that these waves are weak stress waves with a threshold intensity of 131 MPa in the silicon substrate. Shock generation was achieved through confinement of plasma, generated upon irradiation of an absorptive paint layer held against the substrate side of the wafer. These stress waves were below the threshold required for sample fracturing. Interestingly, the transparency of silicon in the infrared region could be exploited to increase the threshold of initiation by shining the laser through the backside of the supporting wafer, revealing a method of isolating the energetic material both from damaging environmental conditions (i.e. moisture) and from potentially risky electrical initiation trains.

The reaction between pSi and the loaded oxidising agent was studied using correlated differential scanning calorimetry (DSC) and FTIR spectroscopy for samples heated continuously between ambient and 500 °C. It was observed that the energetic reaction between pSi and sodium perchlorate depended on the presence of various hydride species on the surface of freshly etched pSi, and on formation of volatile free radical species released

during either oxidation of the surface in the presence of air at about 200 °C or during desorption of the hydride above 270 °C in the absence of oxygen. However, energetic reactions between pSi and PFPE were delayed until pyrolysis of the PFPE above 390 °C in the absence of oxygen, suggesting PFPE's suitability for pyrotechnics applications. Correlated thermal and spectroscopic methods of analysis gave new insights into the earliest stages of the reaction of these energetic materials.

DECLARATION

I certify that this Thesis does not incorporate without acknowledgment any material previously submitted for a degree or diploma in any university; and that to the best of my knowledge and belief it does not contain any material previously published or written by another person except where due reference is made in the text.

Andrew Mark Plummer

ACKNOWLEDGMENTS

These studies and preparation of this Thesis has been an almost 9 year journey. While this is a highly personal activity, it could not have been achieved without support from a significant number of people who deserve grateful acknowledgement. These include:

- Joe Shapter and Nico Voelcker for their enduring patience, support, guidance, scientific advice and a very strong sales pitch which convinced me to return to study,
- Jason Gascooke and Valerian Kuznetsov for their cheerful encouragement and enthusiasm,
- Rachael Lowe and Steve McInnes for teaching me how to make porous silicon, and general guidance in the earliest stages of my studies,
- Bill Drury, Wayne Peacock and Chris Price for translating my rough sketches and ideas into functional and reliable equipment,
- Ash Slattery, Christopher Gibson and Cameron Shearer for analytical and instrumentation support,
- Chad Prior, Stewart Walker and Ian Lockhart for their support through the Centre of Expertise for Energetic Materials,
- Praveen Gangadharan and Craig Wall for their assistance with the sensitiveness testing of porous silicon, and
- Jon Campbell and Paul Kirkbride for their help with the calorimetric and spectroscopic analysis of porous silicon.

This project was made possible through the funding and support of the Centre of Expertise for Energetic Materials, a collaborative research partnership between Flinders University and the Defence Science and Technology Group.

Finally, I am extremely grateful to my wife Kelli, and my son Declan, for tolerating closed doors when typing, long days split between the lab and work, concentrating on the latest paper at the dinner table, and the giving me the confidence that it will all be worth it in the end.

LIST OF FIGURES

Figure 1-1: (a) Cross sectional, and (b) top-down SEM images of a typical pSi surface(3).....	3
Figure 1-2: Proposed reaction sequence in steps A - E for the electrochemical etching of silicon (4).....	4
Figure 1-3: Effect of crystal orientation on pore formation (3).....	6
Figure 1-4: Proposed model of pore growth in pSi preferentially at the pore tips, adapted from(18).....	8
Figure 1-5: Progressive burning of pSi loaded with SP, displaying the position of the flame front as a function of time, by (22). The images were captured on a Photron Fastcan SA5 high-speed video camera at a rate of 930000 frames per second.	26
Figure 1-6: Gold velocity probes laid across a strip of pSi (45).....	27
Figure 1-7: SEM images of microscopic channels formed and etched with pSi, providing enhanced flame velocity in pSi energetic materials (62).....	37
Figure 1-8: Configuration of patterned channels formed within pSi for flame speed enhancement experiments. Channels were formed either perpendicular or parallel to the direction of travel of the flame (62).....	38
Figure 1-9: Relationship between SSA, porosity and burning rate (22).	40
Figure 1-10: Airbag initiators fabricated by Clément <i>et al.</i> (37).	46
Figure 1-11: Fabricated integrated circuit incorporating a pSi explosive element (63).	47
Figure 2-1: Example of a simple etching cell arrangement including Teflon cell top (1) and base (2), platinum cathode (3), backing anode (4), silicon wafer to be etched (5) and o-ring seal (6).	52
Figure 2-2: High resolution SEM image of pSi etched in 40% HF / ethanol, continuous current @ 22.7 mA.cm^{-2}	55
Figure 2-3: Cross-section SEM image of pSi etched for 30 minutes at 45 mA.cm^{-2} in 10% HF / ACN. The porous layer (Region i) is clearly visible above the supporting unetched Si wafer (Region ii).	56
Figure 2-4: Typical appearance of (a) well-etched and (b) degraded pSi surfaces.	57
Figure 2-5: Pore size distribution of pSi etched under varying current / electrolyte regimes. .	60
Figure 3-1: A) and B) Fibre-optic array consisting of stainless steel block (1) and base (2), sample (3), adjustable spark electrode (4), Teflon insulator (5) and fibre optic probes (6). The	

array is clamped together using retaining bolts through the upper block (7) and may be held away from the sample using spacers (8). C) Representative oscilloscope trace from fibre optic array (collected on DSO-2090 USB oscilloscope for presentation, 40 MHz resolution) for pSi etched at 22.5 mA cm^{-2} , 40% HF electrolyte, 180 duty cycles, initiated in confined configuration. The 5th fibre optic probe failed to trigger the voltage drop from -2.0 to -2.5 V – measured velocity is averaged over the preceding four probes. 70

Figure 3-2: Reaction velocity (under confined and unconfined conditions) as a function of pore depth for pSi etched at 22.5 mA cm^{-2} in 20% HF electrolyte solutions, loaded with SP (n=5). 76

Figure 3-3: Flame development in pSi loaded with $\text{Ba}(\text{ClO}_4)_2$, displaying progression from initial ignition by the spark, radial burning, and development of the inverted-V pattern. Panel increments are in milliseconds, as indicated. Flame speed between images at 4.0 and 8.0 ms is approximately 3.0 m.s^{-1} 84

Figure 3-4: A) pSi sample of $24.9 \mu\text{m}$ thickness (etched at 45 mA cm^{-2} , 90 duty cycles in 20% HF electrolyte), displaying inverted V steady state reaction front. Flame is proceeding toward the camera from the spark electrode at the top of the sample. B) pSi sample of $49.9 \mu\text{m}$ thickness (etched at 45 mA cm^{-2} , 180 duty cycles in 20% HF electrolyte), displaying straight steady state reaction front, advancing toward the camera. 84

Figure 3-5: a) pSi sample of $24.9 \mu\text{m}$ thickness (etched at 45 mA cm^{-2} , 90 duty cycles in 20% HF electrolyte), loaded with SP, and b) diagram of sample cross section. The sample cracked along the longitudinal axis, leaving a free face of pSi unsupported by the surrounding wafer, and displays only half of the inverted V steady state reaction front. 85

Figure 3-6: $49.9 \mu\text{m}$ thick pSi sample, depicting flame break-through ahead of main reaction front. 86

Figure 3-7: a) Cross-section SEM image of pSi (regions i and ii) loaded with CaCl_2 (region ii) supported by the unetched Si wafer (region iii), and b) atomic concentrations of Si and Ca through the depth of the sample into the unetched wafer (the depth reference of $0 \mu\text{m}$ is the top of the pSi layer). 89

Figure 3-8: Selected Raman spectra across the pSi surface loaded with PFPE including blank pSi and PFPE samples for comparison (the depth reference of $0 \mu\text{m}$ is the top of the pSi layer). Peaks unique for pSi (625 cm^{-1}), and PFPE (744 and 810 cm^{-1}) are highlighted. 92

Figure 3-9: Penetration of PFPE into pSi layer. Signal intensity corresponds to the pSi band at $597\text{-}693 \text{ cm}^{-1}$ and the PFPE band at $792\text{-}817 \text{ cm}^{-1}$ (the depth reference of $0 \mu\text{m}$ is the top of the pSi layer). 93

Figure 3-10: Linear burning along convoluted paths of narrow pSi channels loaded with SP (106) 97

Figure 4-1: Sample confinement in Rotter Impact Test. Samples of pSi energetic material were sandwiched between the hardened steel anvil and the brass cap. The 5 kg drop weight falls under gravity, colliding with the striker and thereby impacting on the sample (118). ... 104

Figure 4-2: a) BAM friction apparatus indicating weight suspended on armature, and b) detail view of interface between ceramic pistil and base plate (118).	105
Figure 5-1: Schematic of the home-built PDV system used in this study. The 1550 nm CW laser is aimed at the front surface of the target, via the three port circulator, and is recorded on the digital storage oscilloscope (DSO). The 1064 nm laser pulse (A) is reflected from the rear surface of the target (B) and captured by a second photodetector to function as a timing reference.	115
Figure 5-2: Screen shot of DSO output, depicting Channel 1 (PDV photodetector, yellow trace) and Channel 2 (timing photodetector, blue trace). Variation in the beat frequency recorded by the PDV is directly related to the changing velocity of the surface. Time scale is 50 μ s per division.	116
Figure 5-3: SEM image of the absorbing black paint layer on the glass slide used to generate confinement, showing delamination of the paint from the glass during preparation of the cross-sectional samples for imaging.	118
Figure 5-4: a) Sample assembly for laser shock initiation of pSi samples, b) Sample assembly for “laser thermal” ignition, c) Sample assembly for simultaneous recording of wave and particle velocity of unetched Si (two unetched Si wafers are depicted, however, up to three layers could be effectively assembled in this manner), and d) Sample assembly for recording of wafer acceleration due to exploding pSi.	119
Figure 5-5: PDV system depicting a) location of timing photodetector to rear of sample holder, and b) position of PDV probe (yellow fibre optic cable) near to front side of sample surface through the circular window of the clamping assembly.	121
Figure 5-6: pSi loaded with SP ignited using laser-generated shockwave.	123
Figure 5-7: Cross-sectional SEM images of pSi layer above supporting substrate after laser-induced shock event ((a) low and b) high resolution). These are indistinguishable from the samples not subjected to laser-induced shock.	125
Figure 5-8: Time of arrival of the wave emerging from Si wafers subjected to laser-induced shock wave loading at varying laser pulse energies.	127
Figure 5-9: A) Free surface velocity profile of a 502 μ m thick Si wafer loaded by a shock wave from a 630 mJ laser pulse, depicting the surface acceleration and a peak surface velocity of approximately 52 $\text{m}\cdot\text{s}^{-1}$ (phase i), surface deceleration due to membrane pull-back (phase ii), and bulk movement of the Si wafer at a velocity of between 25 and 30 $\text{m}\cdot\text{s}^{-1}$ (phase iii). B) Free surface velocity of Si wafers subjected to laser-induced shock.	128
Figure 5-10: U_{fs} profiles of a) unloaded sample (375 μ m thick Si wafer with 68 μ m thick pSi layer) and b) sample loaded with SP upon irradiation with a 140 mJ laser pulse. The initial peak U_{fs} of the loaded sample is obscured by the resolution of the Matlab signal processing parameters to increase the velocity range to >100 m/s.	131

Figure 6-1: Linkam FTIR600 hot stage accessory (1) installed within the FTIR instrument, also depicting the purge gas inlet (2) and outlet (3), with a sample of pSi clamped against the heating element (4, inset).....	141
Figure 6-2: Background single beam transmission spectra for unetched Si wafers at elevated temperatures.....	143
Figure 6-3: DSC scans of a) blank pSi in air, b) blank pSi in N ₂ , c) blank SP in air, d) pSi / SP EM in air, e) pSi / SP EM in N ₂ , f) blank PFPE in air, g) pSi / PFPE EM in air, and h) pSi / PFPE in N ₂	144
Figure 6-4: 2D FTIR spectra as a function of temperature of a) blank pSi in air, b) blank pSi in N ₂ , c) blank SP in air, d) pSi / SP EM in air, e) pSi / SP EM in N ₂ , f) blank PFPE in air, g) pSi / PFPE EM in air, and h) pSi / PFPE in N ₂	145
Figure 6-5: FTIR spectra of a) blank pSi, b) blank SP, c) pSi / SP EM, d) blank PFPE, and e) pSi / PFPE EM, collected at 150 °C for samples heated in a N ₂ atmosphere. The triplet of peaks at $\approx 2109\text{ cm}^{-1}$ (Si-H _x vibration) and a single peak at $\approx 910\text{ cm}^{-1}$ (Si-H ₂ scissoring) are specific for the pSi surface and clearly distinguished from a strong absorption band between ≈ 1000 and 1200 cm^{-1} (associated to multiple perchlorate vibration modes) and a sharp absorption peak at $\approx 980\text{ cm}^{-1}$ attributed to overlapping PFPE CF ₂ / CF ₃ vibrations.	146
Figure 7-1: Structures of a) ammonium dinitramide and b) CL-20 energetic materials	159
Figure B-1: Correlated 1D and 2D FTIR and DSC thermographs - blank pSi in air.	176
Figure B-2: Correlated 1D and 2D FTIR and DSC thermographs - Blank pSi in N ₂	177
Figure B-3: Correlated 1D and 2D FTIR and DSC thermographs - blank SP in N ₂	178
Figure B-4: Correlated 1D and 2D FTIR and DSC thermographs - pSi / SP energetic material in air.	179
Figure B-5: Correlated 1D and 2D FTIR and DSC thermographs - pSi / SP energetic material in N ₂	180
Figure B-6: Correlated 1D and 2D FTIR and DSC thermographs - blank PFPE in N ₂	181
Figure B-7: Correlated 1D and 2D FTIR and DSC thermographs - pSi / PFPE energetic material in air.	182
Figure B-8: Correlated 1D and 2D FTIR and DSC thermographs - pSi / PFPE energetic material in N ₂	183

LIST OF TABLES

Table 1-1: Summary of silicon wafer etching conditions.....	30
Table 2-1: Comparison of etching conditions.....	59
Table 3-1 Reaction velocity (under confined and unconfined conditions) as a function of surface porosity and pore size, etched at varying electrolyte concentrations. Displayed errors are 1 standard deviation (n = 5).	72
Table 3-2: Reaction velocity (under confined and unconfined conditions) as a function of pore depth for pSi etched at 22.5 mA.cm^{-2} in 20% HF electrolyte solutions, loaded with SP. Displayed errors are 1 standard deviation (n = 5).	75
Table 3-3: Burning rate of pSi loaded with various oxidising agents.	80
Table 4-1: Initiation sensitivities of pSi loaded with SP or PFPE (n = 6).	107
Table 6-1: Characteristic frequencies of relevant transitions of species encountered during this study.....	142

LIST OF PUBLICATIONS

- [1] Plummer, A., Kuznetsov, V., Joyner, T., Shapter, J., and Voelcker, N.H., 2011, “The burning rate of energetic films of nanostructures porous silicon,” *Small*, 7 (23), pp3392 – 3398.
- [2] Plummer, A., Kuznetsov, V., Gascooke, J., Shapter, J., and Voelcker, N.H, 2014, “Laser shock ignition of porous silicon based nano-energetic films,” *Journal of Applied Physics*, 116, p054912.
- [3] Plummer, A., Kuznetsov, V., Gascooke, J., Shapter, J., and Voelcker, N.H, 2016, “Sensitiveness of porous silicon based nano-energetic films,” *Propellants, Explosives, Pyrotechnics*, 41, pp1029-1035.
- [4] Plummer, A., Kuznetsov, V., Gascooke, J., Shapter, J., and Voelcker, N.H, 2017, “Combined thermal and FTIR analysis of porous silicon based nano-energetic films,” *RSC Advances*, 7, pp7338-7345.

The above publications have been reproduced in this Thesis as follows:

- Chapter 3 contains [1] and parts of [3]
- Chapter 4 contains parts of [3]
- Chapter 5 contains [2]
- Chapter 6 contains [4]

GLOSSARY OF TERMS

DRIE	Deep reactive ion etching
EM	Energetic material
EtOH	Ethanol
HF	Hydrofluoric acid
MeOH	Methanol
PFNA	Perfluorononanoic acid
PFPE	Perfluoropolyether
NEQ	Net explosive quantity
SP	Sodium perchlorate
SSA	Specific surface area
TGA/MS	Thermogravimetric analysis / mass spectroscopy

Chapter 1 A REVIEW OF POROUS SILICON ENERGETIC MATERIALS, THEIR FORMATION, PROPERTIES AND BEHAVIOUR.

Background information describing the formation of porous silicon energetic materials, including relevance and context compared to alternative energetic materials is provided.

1.1 Introduction

Porous silicon (pSi) is an engineered material that has sparked wide interest since its discovery in 1956 (1). Because of the ability to create highly ordered surface structures in a simple and efficient manner, pSi has found numerous applications in fields as diverse as optoelectronics, tissue culture, bio-active sensors, and microelectro-mechanical systems (1). However, the discovery in 1992 (2) that pSi could react explosively in the presence of a strong oxidising agent has sparked interest in its use as an energetic material. The following Chapter will examine some of the properties of porous silicon and how the material has been investigated as an energetic material.

1.2 Porous silicon formation

1.2.1 General aspects of porous silicon etching

Porous silicon is a structure created during the chemical or electrochemical etching of single crystalline silicon wafers, creating a series of cavities in the bulk of the wafer whilst leaving the overall dimensions of that wafer substantially unchanged (3). The morphology of these pores can vary in appearance from disordered sponge-like structures to highly-ordered uniform channels, as depicted in Figure 1-1, and is typically characterised by the dimensions of these pores, the thickness of the layer, the volume fraction of the pores (i.e. porosity) and overall surface area. A large body of work has been carried out in an effort to understand the nature of these surfaces (3–16).

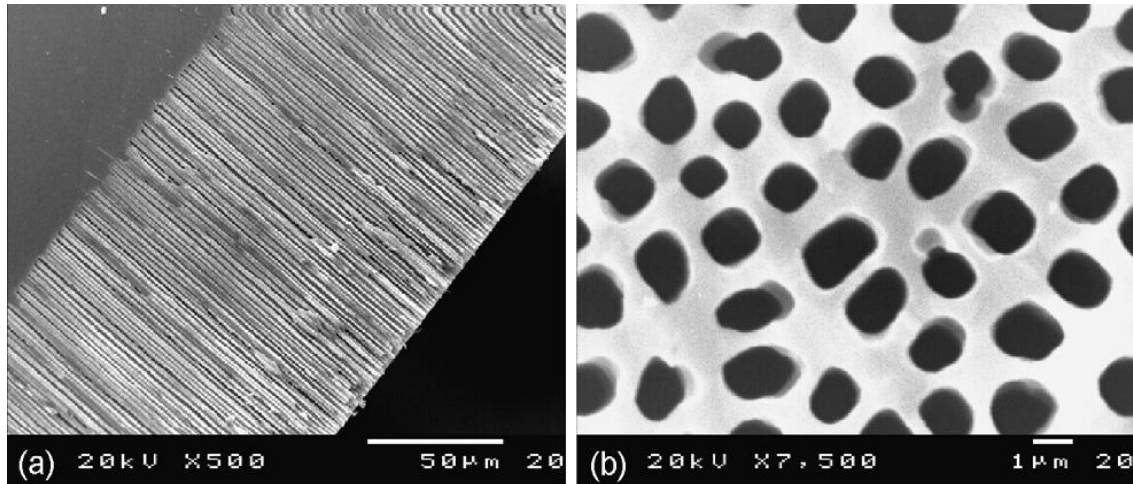


Figure 1-1: (a) Cross sectional, and (b) top-down SEM images of a typical pSi surface(3).

The etching process is most commonly carried out using anodic etching in hydrofluoric acid electrolyte solutions. Whilst an alternative process for pSi formation (termed stain etching) exists, this process produces films far thinner than those produced by anodic etching (7) and does not appear to have been used in energetic material applications of pSi, possibly due to the fact that it is harder to control pore size and porosity in stain etching.

The chemistry of the dissolution of silicon under etching conditions is complex. It is believed that the following reaction sequence occurs (4):

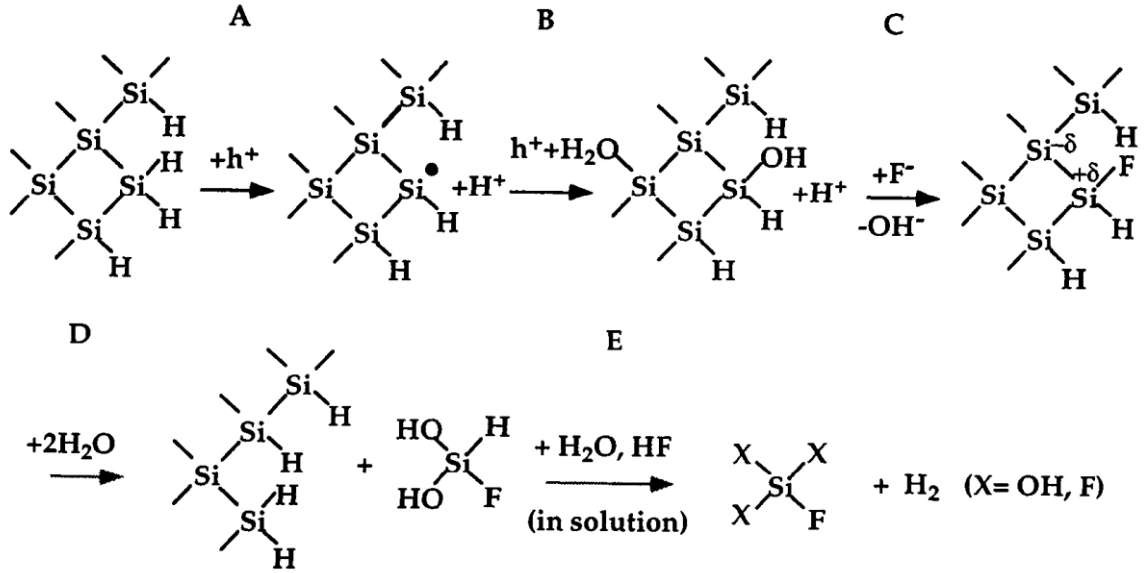


Figure 1-2: Proposed reaction sequence in steps A - E for the electrochemical etching of silicon (4).

Migration of charge holes to the silicon surface enables oxidation of a silicon atom at the surface (Steps A and B). The hydroxide formed is attacked by fluoride ions (Step C) to create a highly polarised Si-Si back bond. This bond is subsequently hydrolysed (Step D) removing the attacked Si atom from the surface, leaving the remaining Si (bound to the surface) terminated with a hydrogen atom. The final stage (Step E) involves further oxidation of the dissolved Si species with evolution of hydrogen gas. Etching progresses essentially as a result of balance between the competing reactions of surface oxidation (influenced by the supplied etching current causing electron hole migration to the surface) and oxide removal (influenced by HF electrolyte concentration) (12).

Partially oxidised silicon surfaces exposed to the air for a period of time (as would be the case for a fresh manufacturer-supplied wafer) will be covered in an oxide layer a few atomic layers thick (14). This surface would be attacked by fluoride ions in the electrolyte solution at

Step C, Figure 1-2, before further participation in the etching process, however without generation of motion of hole carriers to the interface pSi formation will not progress.

Etching electrolytes are based on an aqueous solution of hydrofluoric acid (HF) diluted with either aqueous or organic solvents (eg. ethanol, acetonitrile, dimethyl formamide and dimethylsulfoxide) (3). As freshly prepared etched pSi surfaces are strongly hydrophobic (3), such solvents are added to the electrolyte solution in order to reduce the interfacial tension between the electrolyte and the silicon surface (3, 10), a factor considered essential to producing uniform films for two reasons. Firstly, low interfacial tension electrolytes permit the generated hydrogen bubbles to detach from the surface with greater efficiency, enabling fresh electrolyte to re-cover the surface. Secondly, such electrolytes are able to penetrate deeper into fine pores whereas purely aqueous electrolytes cannot. It has also been suggested that pore formation is influenced through the use of solvents that can contribute to the dissolution reactions rather than merely acting as a surfactant (3, 6), by directly contributing to the oxidation of the silicon surface (Steps A and B, Figure 2).

Anodic etching is primarily carried out under conditions of constant current, permitting greater control over pore geometry and produces more reproducible pSi layers (10). This is due to the fact that above a certain critical current density, the balance between surface oxide formation and oxide dissolution is shifted toward oxidation, resulting in a phenomena known as electropolishing (6). Maintaining a constant current enables one to control the reaction balance, producing a pSi surface having desired properties with a strong degree of

reproducibility (6). Etching is carried out in specially constructed cells able to withstand the HF based electrolyte, primarily Teflon (PTFE) cells with platinum electrodes (3, 10).

Under the conditions necessary for pSi formation, it has been shown that pore growth will occur preferentially at the tip of the pore, causing the pore to grow into the substrate while leaving the overall dimensions of the wafer unchanged (3). Furthermore, it has been shown that pores will grow preferentially in the direction of the (1 0 0) crystal plane (3, 6). However, branching can occur along different planes at a much slower rate, as depicted in Figure 1-3. From this, it can be seen that careful selection of the silicon wafer is necessary to produce the desired results.

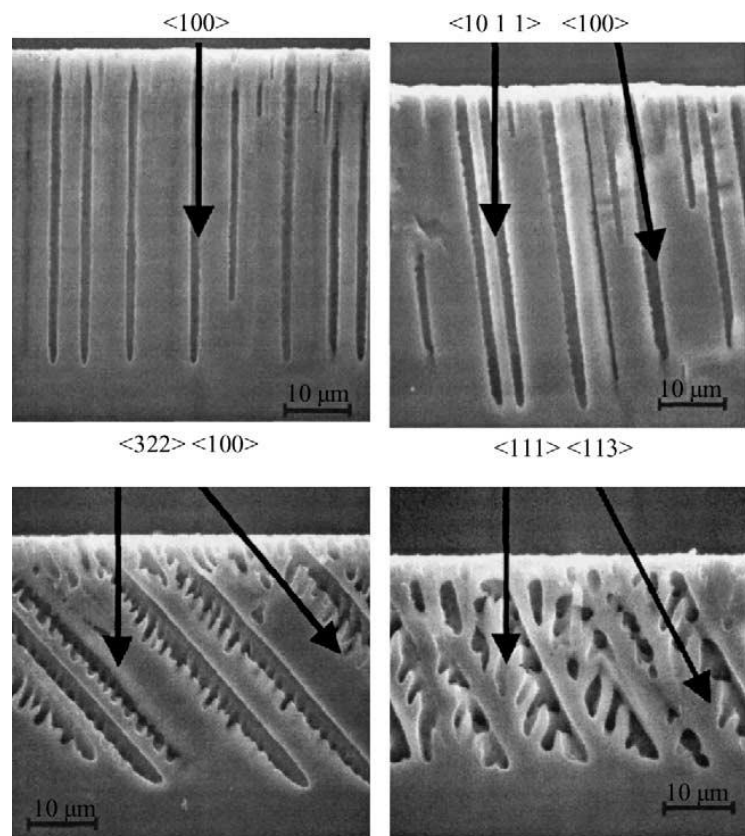


Figure 1-3: Effect of crystal orientation on pore formation (3).

The reason for preferential growth at the tip of the pores in the (1 0 0) direction is not clearly understood. While there would be an expectation that pores would grow directly toward the source of the charge holes, i.e. to follow the path of least resistance, growth along the (1 0 0) direction always dominates (3, 17). Parkhutik (18) extensively reviewed porous silicon formation and growth mechanisms. Ignoring the influence of patterned etching, pores will essentially initiate on the surface randomly at a spatial concentration determined by the dopant concentration in the wafer, charge concentration of the applied current, and diffusion of the reactive fluoride species to the surface (i.e. boundary layer effects). However, once those pores are initiated, it was proposed that pores deepen mainly due to a concentration of the local electrical field at the tip of the pore which either overcomes the Schottky barrier formed at the Si / electrolyte interface or quantitatively increases the oxidation of the Si in this region (18). This does not explain, however, why growth dominates along certain crystal planes, but not others. A supplementary theory that was discussed by Parkhutik (18) is that mechanical stresses created at the tip of the pores created by pressure of the evolved H₂ bubbles, and weakening of the Si matrix by hydride formation, both contribute to mechanical fracture of the Si along the weakest (1 0 0) crystal plane – such a scheme is presented in Figure 1-4. Pore sizes may also influence the balance between pore tip growth and branching growth, with narrower pores restricting ingress of fresh electrolyte (and egress of evolved H₂), thereby enhancing opportunity for branching compared to larger pore structures – such effects are described further in Section 2.1.5.

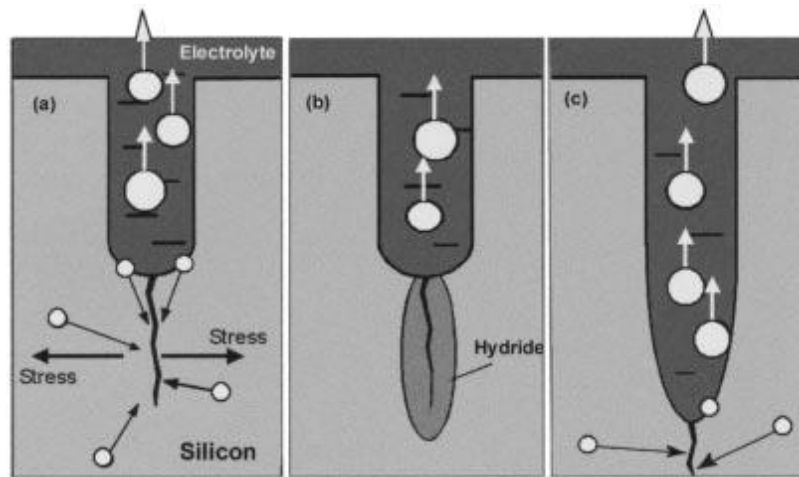


Figure 1-4: Proposed model of pore growth in pSi preferentially at the pore tips, adapted from(18).

The variables that can be adjusted during anodic etching of pSi are 1) electrolyte concentration, 2) etching current density (expressed as $\text{mA}\cdot\text{cm}^{-2}$), 3) etching time, and 4) wafer dopant type and concentration (10, 15). Generally, these factors will influence the final pSi surface as follows:

- It has been found that the etching rate will increase with increasing concentration of HF in the electrolyte (19), however this will decrease porosity.
- Increasing current density will lead to both an increased etching rate and porosity (10). There is a limit to this, however, in that increasing current density above a critical level will lead to the phenomena of electropolishing, or stripping of the porous surface (3, 16). This critical value is dependent on electrolyte concentration and wafer doping level.
- The thickness of the etched layer increases almost linearly with increasing etching time (10), however there is only a minor increase in pore size with increased etching time, supporting the observations that growth occurs at the pore tip preferentially

rather than at pore walls.

- The effect of wafer resistivity is more complicated. Lee *et al.* (12) found that pore growth rates will increase with increasing wafer resistivity up to 150 $\Omega\cdot\text{cm}$, but decreases after this point, indicating that care must be taken when choosing a substrate for a desired application.

These factors are clearly not independent and to create reproducible pSi surfaces one must define and control all of the available variables.

1.2.2 Characterisation of porous silicon surfaces

The most important parameters used to describe a pSi surface are pore size, layer porosity, layer thickness and specific surface area (10).

With respect to pore size, pSi may be described as being macroporous (pore diameters greater than 50 nm), mesoporous (2 to 50 nm pore diameters) or microporous (also known as nanoporous, pores less than 2 nm diameter) (20). Pore size and porous layer thickness, can be measured using standard electron microscopy or atomic force microscopy techniques, while porosity is the volume fraction of voids present within the surface and is determined gravimetrically (10).

Finally, the specific surface area (SSA) is most commonly determined by gas adsorption techniques using Brunauer – Emmett – Teller (BET) theory to determine surface areas (20).

For energetic material applications, it is desirable to have as large a specific surface area as possible to increase the rate of reaction (21). Energetic pSi variants have been reported as low as $191 \text{ m}^2 \cdot \text{g}^{-1}$ to over $900 \text{ m}^2 \cdot \text{g}^{-1}$ (22). High specific surface area can be achieved by decreasing pore size to increase the number of pores (and hence pore surface area) per unit volume. The trade-off is that decreasing pore size to achieve this will hinder impregnation of the oxidising agent into the pore (15). Conversely, increasing porosity to achieve greater impregnation will cause a corresponding decrease in the specific surface area, reducing the silicon available at the surface to react. A more detailed discussion of this relationship is presented in Section 1.4.2

1.2.3 The surface structure of fresh and aged porous silicon

During the etching process, silicon atoms at the surface will be hydride terminated (10, 13), as was indicated by the reaction sequence described in Figure 1-2. Infra-red spectroscopy has identified that Si-H, Si-H₂ and Si-H₃ species are all present at the surface (13). While specific ratios vary, Grossman and Ortega (9) indicated that due to the very high surface area of pSi in the order of 20% of all Si atoms exist at the surface of the pores. Therefore this hydrogen can form an appreciable mass quantity of the bulk surface and contribute to the energetic reaction. Indeed, Lazaruk *et al.*(23) determined that this hydrogen comprises in the order of 4% of the mass of a pSi surface (equivalent to 54 mol %, yielding a ratio of Si-H_{1.17}). In the presence of both oxygen and moisture, the underlying silicon substrate can be oxidised, interspersing Si-Si bonds with Si-O-Si bonds over a period of several hours to days (14), reaching saturation when the oxide layer reaches a thickness of approximately 1 nm. As this oxide layer can take

some time to stabilise, the pSi surface is sometimes artificially aged by annealing it in air at elevated temperatures for short periods of time in an effort to control the properties of that surface (24). A critical point exists, however, at 300 °C. Investigations using infra-red spectroscopy (24) have shown that above this point the bound hydrogen layer is stripped from the surface, leading to hydrophilic silicon oxides and hydroxides directly on the surface. As will be discussed later, workers in the field of pSi energetic materials have used both fresh and annealed pSi, with varying results.

1.3 Explosives and energetic materials – a general discussion

An explosive chemical reaction (as distinct from nuclear and mechanical explosions) is a sudden and violent chemical reaction that liberates chemical energy as heat, light and high pressure gas (25). This process produces gas at such a high rate that it occupies essentially the same volume as the original unreacted material, and the overall energy liberated is often in the order of 3000 – 7000 kJ.kg⁻¹. These factors combine to pressurise the gas produced by the reaction to very high levels (often in the order of giga Pascals) (25), and it is the expansion of these gasses that causes work to be done on the surrounding medium with sufficient speed that it creates a shock wave in that medium. Furthermore, while these reactions often liberate gaseous reaction products, gasless formulations exist which still liberate heat in sufficient quantities and at a high enough rate to pressurise the adjacent atmosphere and thereby perform work on the surrounding medium. Lee (26) broadly classified these energetic materials as explosives, propellants or pyrotechnics based primarily on their behaviour when used as intended.

An explosive reaction can be further classified as either a deflagration or a detonation.

Deflagration is a subsonic combustive process, propagating through the material due to the heat transfer processes of conduction, convection and radiation from the hot reaction products to the cold material (25, 27, 28), with reaction front velocities (termed burning rate for these explosives) typically measured as being less than 1000 m.s^{-1} . Deflagration is susceptible to external influences - specifically the burning rate is exponentially proportional to the external pressure, according to Vielle's law:

$$R = aP^b \quad \text{Equation 1-1}$$

where R is the burning rate, a and b are constants, and P is the gas pressure (resulting from both ambient atmospheric conditions and gas generated during burning) (25). An example of a deflagrating explosive is gunpowder. This substance (nominally 75% potassium nitrate, 10% sulphur and 15% charcoal) will burn rapidly if ignited in the open air. However, if ignited when confined the gaseous reaction products cause the local pressure (inside the confined environment) to rise leading to an exponential increase in the burning rate, the effect of which is that the confined gunpowder will deflagrate.

Detonation, however, is a substantially different and more complex process. In condensed explosives the reaction propagates through the material due to a supersonic shockwave that both initiates and is sustained by the reaction (25, 28). Reaction front velocities (termed detonation velocity for these explosives) are typically measured in the order of 1500 –

9000 m.s⁻¹. Examples of such explosives include lead azide or nitroglycerin. However, for heterogeneous explosive mixtures, especially porous or granular mixtures, the speed of the shockwave can be substantially reduced as energy is consumed in overcoming friction between particles, and material stress to collapse voids (29). Furthermore, pressure at the rear of the reaction front can be so high as to force gaseous reaction products forward, jetting through narrow channels in the porous media at velocities exceeding 1500 m.s⁻¹ (30, 31). Therefore, for porous heterogeneous explosives, material structure and gas permeability are significant factors influencing the behaviour of a detonation wave through the material.

Generally though, when a shockwave strikes these materials, the very rapid compression excites and energises molecules within the shock zone, sometimes due to hotspot creation originating from adiabatic compression of entrained gas bubbles, or from frictional heating and mechanical stresses generated in crystal grains (32). This then initiates chemical reaction of the explosive material, generating gaseous reaction products which then act to maintain a pressurised region behind the reaction zone, driving the shockwave forward and continuing the process until the material is consumed. It should be noted that the original shockwave can originate from some external stimulus (e.g. a conventional detonator or high power laser pulse), or can arise if the material is first ignited to deflagration which accelerates so much that it transitions into detonation (33).

Ultimately however, these reactions are simply exothermic reduction / oxidation reactions between a fuel and an oxidising agent. The reacting agents may occur as a mixture of two or more discrete substances, or can take the form of metastable molecules that break apart into

various reactive species (33). The intimacy of mixing is an important factor which controls both reaction initiation and reaction rate (21, 34). Furthermore, whilst it might be desirable for the explosive mixture or molecule to have a stoichiometric ratio of oxidising and fuel species, this is not a prerequisite for an explosive reaction to occur. For example, the high explosive TNT is 73.9% deficient in the quantity of oxygen required for the reaction to proceed to completeness (28), but it will detonate nevertheless.

The application considered in this Chapter involves the exothermic reaction of the fuel (silicon) with the oxidising agent (e.g. sodium perchlorate (SP)) in the following simplified reaction (35) (surface hydride species omitted due to uncertain ratio with Si):



Ostensibly a gasless exothermic reaction, the presence of both crystallisation water associated with the perchlorate, bound hydride species on the silicon surface, and the differences in stoichiometry able to be achieved due to varying pore geometries will complicate matters (24). In these circumstances, the reaction will likely proceed with incomplete combustion, producing substances which can undergo further reaction with atmospheric oxygen due to the high temperatures present. These secondary reactions will often occur over a significantly longer time scale than the initial reaction, and will tend to support or enhance the effect of the explosive rather than contribute directly to it (36).

1.4 Porous silicon energetic materials

1.4.1 The benefits of using porous silicon as the basis for an energetic material

There are a number of advantages to using pSi as the basis for an energetic material. The infrastructure necessary for mass production of silicon based items is well established, and the techniques for that production are well understood (37). The potential exists to incorporate pSi energetic materials directly onto the surface of electronic components, enabling tiny yet complex energetic devices to be constructed (37). As discussed in Section 1.2, the pSi surface is able to be tailored to a wide variety of pore morphologies, through control of a few simple variables.

Finally, the potential energy yield from such materials is much higher than conventional carbon based explosives. Carbon can be substituted for silicon on a direct molar basis in Reaction 1. This yields a far lower enthalpy of reaction of $-407.5 \text{ kJ}\cdot\text{mol}^{-1}$ for carbon ($5560 \text{ kJ}\cdot\text{kg}^{-1}$ of reactant mixture) compared to the $-924 \text{ kJ}\cdot\text{mol}^{-1}$ for silicon ($10350 \text{ kJ}\cdot\text{kg}^{-1}$ of reactant mixture) (35). For reference, the energy liberated by the explosion of the high explosive trinitrotoluene (TNT) is $4564 \text{ kJ}\cdot\text{kg}^{-1}$ (28).

The pyrotechnics industry regularly uses powdered metals as a component for various energetic mixtures (24). It is well known that the speed of the reaction is directly linked to the intimacy of contact between reacting ingredients (21, 34). The very large specific surface area of pSi, potentially as large as $1000 \text{ m}^2\cdot\text{g}^{-1}$ (22, 38), permits a greater degree of homogeneity

between the silicon and the oxidising agent than would occur if the two materials were mixed as powders.

1.4.2 Porous silicon energetic materials

1.4.2.1 Initial discovery

In 1992 when McCord *et al.* (2) at the University of Texas were studying the effects of chemiluminescence emitted from pSi they accidentally discovered that the addition of a drop of concentrated nitric acid (a strong oxidising agent) to a freshly etched pSi surface caused “... a flash of light with and audible pop.” This was the first report of any sort of explosion involving pSi as a reactant, however it appears that no attempt was made to quantify the event.

These observations languished for several years until 2001 when Kovalev *et al.* (39) applied liquid oxygen to a pSi surface. They observed that filling the pores of a freshly prepared pSi substrate with liquid oxygen condensate would lead to an explosion. These explosions would occur spontaneously at temperatures as low as 4.2 K. It was proposed that the explosion was occurring as a result of a chain reaction between the oxygen and silicon occurring after the initial cleaving of Si-Si or Si-H bonds at or near the surface. Aged samples having an oxidised surface layer were also able to react explosively with liquid oxygen, however the Si-O matrix tended to prevent diffusion of oxygen molecules into the underlying Si matrix, thereby providing a degree of stability. Mechanical impact and ultraviolet laser pulses were successfully used to initiate the explosive reaction of the material with an oxidised surface.

1.4.2.2 Development of stable systems and selection of oxidising agents

These two early reports demonstrated the explosive potential of pSi. However they relied on the spontaneous reaction of the material with two powerful oxidising agents. In order for the material to be of any practical use, the reaction should be delayed indefinitely until desired by the user. The first steps toward this were made in 2002 when Mikulec *et al.* (40) presented work which investigated the development of discrete pSi explosive systems applied to atomic emission spectroscopy (AES) and microelectro-mechanical systems (MEMS). Utilising gadolinium nitrate as the oxidising agent, they aimed to produce a system more stable than that of Kovalev *et al.* (39), enabling controlled initiation. Sample preparation used macroporous pSi (pore size $<1 \mu\text{m}$) layers $25 \mu\text{m}$ thick on n-type silicon ($4 \Omega\cdot\text{cm}$) etched for 15 min at $50 \text{ mA}\cdot\text{cm}^{-2}$ with front-side illumination. The nitrate was added as a solution ($10 \mu\text{L}$, 0.2 M in ethanol) and dried in air for 1 hour. In the AES application, target analytes were added either as solutions ($10 \mu\text{L}$, 0.1 M , solvent not specified) or as slurries in ethanol or tetrahydrofuran, with the explosion of the pSi / nitrate mixture providing the necessary excitation for the analyte in question. They reported that initiation was achieved from a spark generated from a coil charged by a 9 V battery.

Spectra were measured using an Ocean Optics SD2000 spectrometer, demonstrating that pSi impregnated with gadolinium nitrate had no significant spectra in the target wavelength region ($400 - 900 \text{ nm}$), but produced a broad peak emission intensity between 650 and 700 nm estimating that this gave a temperature of explosion of 2000 K. This process excited the target analytes sufficiently to achieve sharp emission spectra suitable for reliable

qualitative and quantitative analysis. Interestingly, Mikulec *et al.* (40) mentioned several times that the system was “detonating,” however there appeared to be no data in their work to substantiate this claim. There may be confusion in the literature between the observation of an explosion with the specific phenomenon of a detonation.

Clément *et al.* (37) studied the effect of different oxidising agents on pSi energetic materials in 2005. Using a variety of pSi surfaces, they introduced various oxidising agents into the porous surface as solutions in methanol, ethanol or acetone. These included a wide variety of nitrate and perchlorate salts, potassium permanganate and potassium dichromate. Filling was achieved by successive loading and drying steps to achieve a stoichiometric ratio of oxidising agent to silicon. They also investigated the use of sulphur as an oxidising agent, loaded into the pores either as a solution in carbon disulphide or directly melted into the pores. These systems were then initiated either thermally (on a hot plate), electrically (using a current pulse through an exploding hot wire) or optically (using a pulsed YAG laser), and the explosion measured simply as an observation of ignition. Their work indicated that the most successful oxidising agents included calcium and sodium perchlorates and sulfur. Only marginal success was achieved using ammonium, lithium, silver, iron or potassium perchlorates, and various nitrate salts (although there was no indication that the gadolinium nitrate investigated by Mikulec (40) was also investigated by Clément *et al.* (37)). In contrast to the work by Lazarouk *et al.* (41), no reaction was observed when potassium nitrate was used as the oxidising agent.

Clément *et al.* (37) used passivated pSi surfaces (pSi annealed in air at 250 °C) rather than freshly prepared surfaces, as an attempt to control the degree of surface oxidation. Furthermore, they observed that annealing the pSi at higher temperatures (up to 700 °C) resulted in a hydrophilic surface with oxygen bound to the exposed surface Si atoms (rather than back-bonded as occurs with low temperature and natural annealing). Whereas others (41, 42) have specifically reported that oxidised pSi surfaces would fail to react, the process of low temperature annealing employed by Clément *et al.* (37) did not appear to adversely affect the performance of the systems, although high temperature annealed surfaces failed to react explosively. Unfortunately little detail was provided as to the exact energy of the various ignition techniques employed. It may be the case that their initiation techniques are simply stronger than those used by others, penetrating the oxidised layers on the pSi surface where others could not. However, as pointed out by Koch and Clément (24) annealing of pSi in air above 300 °C results in loss of surface hydride species, and development of back-bonded silicon oxides. This suggests some support for the theory by Kovalev *et al.* (39) that hydride terminated pSi surfaces are necessary for the explosive reaction to occur.

While a variety of oxidising agents have been trialled, SP stands out as having received the most attention(19, 22, 43–73).

Du Plessis (65) compared SP, gadolinium nitrate and elemental sulphur as oxidising agents for pSi ignited by a small electrical spark, finding that SP displayed a distinct explosion compared to visible burning reactions for sulphur and gadolinium nitrate. Recording the optical intensity of the resulting flame, he found that the duration of the reaction for pSi / SP

was complete in less than 10 ms, compared to over 25 and 50 ms for $\text{Gd}(\text{NO}_3)_3$ and S, respectively, and noting that the sample loaded with SP was effectively destroyed upon initiation. Abraham *et al.* (43) compared pSi loaded with a variety of perchlorate and nitrate salts. They determined that SP systems achieved burning rates in the order of 3000 m.s^{-1} , whereas when loaded with sulphur, $\text{Gd}(\text{NO}_3)_3$, $\text{Mg}(\text{NO}_3)_2$, $\text{Ca}(\text{NO}_3)_2$ or the systems achieved burning rates in the order of 2 to 10 m.s^{-1} , and up to 21 m.s^{-1} for $\text{Mn}(\text{NO}_3)_2$. Clearly then, the relative intensity of the explosion and reaction between SP and pSi, compared to other oxidising agents, has fostered the most interest in SP as the oxidiser of choice for further investigations.

An interesting alternative to traditional inorganic oxidising agents has been the use of fully fluorinated polymers, already well known as oxidising agents for energetic materials applications (74, 75). Mason *et al.* (76) reported the use of liquid perfluoropolyether impregnated into a pSi surface. Ignition was impossible using a heating wire applied to the surface, but could be achieved by sustained application of a naked flame to the surface for 10 to 20 s. Burning rates for a thick layer of pSi (layer thickness not specified) at approximately 80-90% porosity were reported as 0.014 m.s^{-1} (1.4 cm.s^{-1}). This is very low compared to the burning rates described for SP systems, nevertheless it does demonstrate the potential for fluoropolymers to be applied to pSi energetic material systems.

1.4.2.3 Burning rates and characterisation of the energetic reaction

Significantly, Kovalev *et al.* (39) made the first measurements to try to characterise the explosion in 2001. The time-resolved light emission of the reaction was measured using the

signal from an amplified photodiode, recorded on a digital oscilloscope. This indicated that the onset of explosion occurred in the order of $0.2 \mu\text{s}$, with peak intensity occurring in the order of $1 \mu\text{s}$, estimating that the reaction front velocity is in the order of $10000 \text{ m}\cdot\text{s}^{-1}$. This is significant in that it places pSi explosives firmly in the realm of high explosives, described in Section 1.3.

This method was also used by several authors in the early history of pSi energetic materials research, including Clément *et al.* (37), du Plessis *et al.* (19, 64, 65), Lazarouk *et al.* (41) and Lazaruk *et al.* (23). In all instances, these groups recorded the optical intensity of the explosion as a function of time by means of some amplified photodetector.

The next major stepping stone in the investigation of pSi energetic materials was conducted by Lazarouk *et al.* in 2005 (41). They presented a systematic study on the effects of the nature of the porous layer on the reaction kinetics. p-type silicon subjected to anodic etching in a 48% HF electrolyte solution was loaded with potassium nitrate, with etching time and current altered to produce a variety of porous layer morphologies. The progress of the reaction was measured using a photodiode and a high-speed video camera. These measurements indicated that the nature of the combustion process changed when the porous layer thickness was increased to beyond $60 \mu\text{m}$. Below this point, the reaction reached a peak in light emission in approximately 10 ms with a delay between initiation and the onset of light emission of approximately 1 ms, measured using a photodiode and oscilloscope to collect and measure optical emissions. However, when the layer was increased to $60 \mu\text{m}$ or more, the light emission commenced in less than 50 ns reaching a peak in 1 ms. Subjectively, this group

noted a significant change in the sound emitted during the event, changing from a “*muted popping*” below 50 μm to a sharp sound that “*...resembles a pistol shot*” above 60 μm , an astute observation of the change in the nature of the events occurring.

Lazaruk *et al.* (23) further studied this process in 2007, quantifying the explosion intensity in terms of the diameter of the flash produced using a video camera. Again, freshly etched pSi surfaces were impregnated with a 10% aqueous KNO_3 solution. However this work made reference to the use of a centrifuge to assist impregnation of the oxidising agent into the pores. Whilst not stated explicitly, centrifuging is presumably used to overcome the bridging of pore openings due to the high surface tension of aqueous solvents compared to alcoholic (ethanol / methanol) solvents on the hydrophobic pSi surface. Their results indicated that explosive intensity (flash diameter) increased almost linearly with increasing pSi layer thickness, with complete destruction of the Si backing substrate occurring at thickness beyond 100 μm .

Additionally, Lazaruk *et al.* (23) studied the effects of storage on such loaded pSi samples, examining the explosive intensity at 24 and 48 h after loading. The authors demonstrated that explosive performance decreased with increasing storage time, an observation that was attributed to the oxidation of the pSi surface involving replacement of the Si-H groups with Si-O groups. Indeed, Lazaruk *et al.* (23) found that for each 1 cm^2 of a 100 μm thick etched surface, up to 5 cm^3 of hydrogen gas can be desorbed from the surface in as little as 2 h, calculating that hydrogen atoms comprised up to 4% by weight of the pSi surface.

Du Plessis and Conradie (19) studied the effects of pore dimensions on explosive performance. Using p-type silicon wafers having different resistivities, they prepared pSi surfaces having porosities in the order of 70%. This process produced pores having specific surface areas of 180, 440 and 650 m².cm⁻³ for high, medium and low resistivity wafers, respectively. These were loaded with sodium perchlorate or gadolinium nitrate solutions in methanol or ethanol, or a sulphur solution in CS₂. The amount of oxidising agent loaded into the surface was determined gravimetrically. Explosions were characterised by measuring the time resolved intensity of light emission using a photodiode. Ignition was achieved by placing the loaded wafer onto a hotplate, with ignition temperatures ranging from 243 to 313 °C for the various oxidants. In an extension of the work described in (19), du Plessis (65) further developed the subjective analysis of pSi energetic materials using a factor described as a Figure of Merit (FOM), which gives weighted scores to a variety of objective and subjective observations including the sound produced, distance of ejected particles and integrated area of light emission (measured by the photodiode technique). In both these reports (19, 65), du Plessis *et al.* determined that the optimum conditions for explosion were a pSi surface having pore diameter in the order of 3 nm and utilising sodium perchlorate as the oxidiser. As with other groups, du Plessis and Conradie (19) have claimed that detonation is occurring, without actually providing data to support the assertion.

Dawson (42) investigated the effects of varying oxidising agents on the properties of the explosion of pSi, and the effect that aging the surface would have on the resulting explosion. Analysing time resolved light emission, collected using an amplified photodiode, Dawson

determined that the oxidising agent sodium perchlorate produced a stronger explosion than gadolinium or aluminium nitrates, both in terms of peak light output and total (integrated) light output. Dawson also found that after the pores had been filled to capacity with oxidising agent, further loading of that agent would result in a decrease in explosive performance due to wasting of explosive energy in ejecting non-reacting material from the surface. Similarly, a peak in explosive performance was determined to occur with pores having a mean size of 11.8 nm (aluminium nitrate oxidising agent), inferring that there is an optimum balance between pore size, specific surface area and the ability of the oxidising agent to intimately mix with the silicon fuel. Dawson further found that samples exposed to a humid atmosphere for more than 44 h would fail to react explosively, due to accumulation of the oxide layer on the pSi surface.

Two other results from this work were of interest. Firstly, using pSi loaded with aluminium nitrate, Dawson (42) determined through differential scanning calorimetry that the energy released by the explosion is 8.67 kJ.g^{-1} , significantly higher than the energy released by the explosion of TNT (4.6 kJ.g^{-1} (28)). This supports the estimates of the high theoretical energy output of a pSi and SP system described in Section 1.3. Secondly, Dawson attempted to introduce the high explosive RDX into the pSi surface both instead of, and in conjunction to, an oxidising agent. This composite explosive was found to react explosively, although with only one third of the light output when compared to aluminium nitrate systems.

Whilst it might seem intuitive to compare optical emission as a means to compare samples, such an approach is somewhat flawed. None of these experiments appeared to have controlled

for use of the same photodetector, nor to have accounted for the different spectral response of various photodetectors on the market, an effect exacerbated when different oxidising agents (each having different spectral emission) are used. Additionally, by not specifying the amplification circuitry used, the actual amount of amplification is somewhat arbitrary, preventing intercomparison of results with other groups. It is argued, therefore, that use of optical emission may be useful for internal comparison of samples within one laboratory, but that it is of very limited value when comparing different works. Finally, optical emission is rarely used in the broader energetic materials discipline to characterise and compare different EM's for any particular application.

A more traditional approach in the energetic materials discipline is to characterise a material by some physio-chemical characteristic that is independent of the measurement method. Commonly, EM's are described in terms of their burning rate or detonation velocity (25).

The first attempt to record the burning rate was documented in 2005 by Clément *et al.* (37). By initiating the sample using a laser at one point and measuring the time taken for the reaction front to interrupt reflection of a second laser a known distance away, Clément *et al.* (37) “...estimated the propagation velocity of the one-dimensional detonation wave to be $>2000 \text{ m.s}^{-1}$.” Again the claim is made that the event is a “detonation”, however apart from reaction velocity, no evidence is put forward to support this assertion.

In 2008 and 2009, three groups almost simultaneously reported the use of high-speed video as

a means to independently measure the burning rate. In 2008, Subramanian *et al.* (68) reported pSi particles prepared by stain etching (up to 11 μm diameter, 4.9 \AA pore diameter) loaded with SP burnt along a loose channel with a velocity of $2484 \text{ m}\cdot\text{s}^{-1}$. Similarly, Mason *et al.* (76) used high-speed videography to study the performance of strips of pSi loaded with various oxidising agents, including SP ($216 - 349 \text{ m}\cdot\text{s}^{-1}$), calcium perchlorate ($144 - 275 \text{ m}\cdot\text{s}^{-1}$) and perfluoropolyether (PFPE) ($0.014 \text{ m}\cdot\text{s}^{-1}$). Currano and Churaman (53) also used high-speed videography to document the velocity of pSi loaded with SP across a pSi surface (33 μm thick layer, 67% porosity, 3.4 nm pores) to be $600 \text{ m}\cdot\text{s}^{-1}$. These three reports are notable in that they strove to characterise the system independent of any material effects, and in a manner which was comparable to other works in this field and to more traditional EM's generally. However, as can be seen from Figure 1-5, resolution of high-speed video cameras will be limited when operating at very high frame rates (77), and the high contrast generated between the illuminated sample and the very high brightness flame, are two factors which may tend to limit precise detection of the position of the flame front.

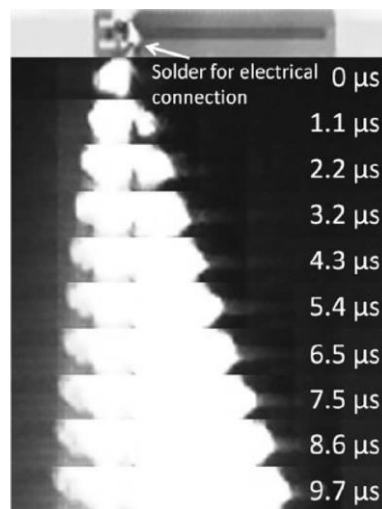


Figure 1-5: Progressive burning of pSi loaded with SP, displaying the position of the flame front as a function of time, by (22). The images were captured on a Photron Fastcan SA5 high-speed video camera at a rate of 930000 frames per second.

An alternative approach was used in 2010 by Becker *et al.* (45) who applied thin gold wires across a strip of masked pSi at 5 mm spacing's (Figure 1-6). Detecting when these wires were broken by the advancing flame along the pSi strip (the “wire-break” method) permitted far more accurate recording of the velocity of the flame front, with measured velocities averaging 3050 m.s^{-1} for pSi loaded with SP (65 – 95 μm layers, $\approx 66\%$ porosity). This was supplemented by high speed videography to help qualitatively analyse the nature of the flame front. Here, they noted that the burning front was erratic and flame break-outs would occasionally appear several mm ahead of the main flame front, giving an apparent velocity in the order of 7000 m/s. Becker *et al.* (45) proposed this as evidence of possible shock wave transmission through the material which would be evidence of a detonation phenomenon, instead of mere deflagration. The use of pre-spaced velocity probes is valuable because it provides a means to record the position of the burning front independent of any subjective effects which might occur if one attempts to interpret the position of the flame from high-speed videography.

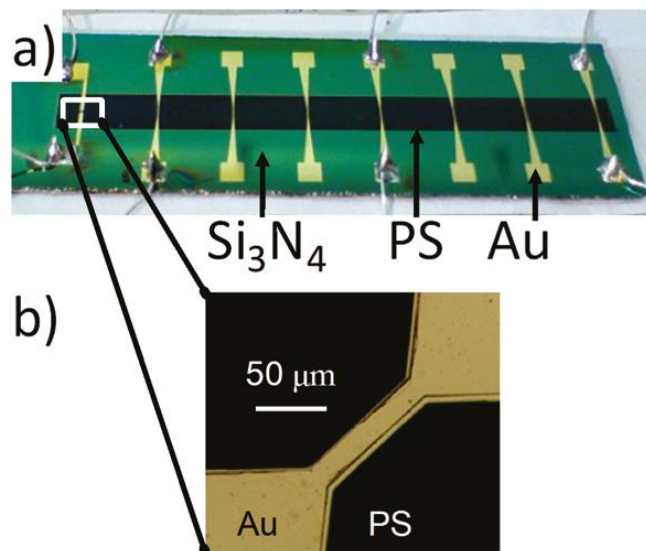


Figure 1-6: Gold velocity probes laid across a strip of pSi (45).

Supplementing their high-speed video work, Subramanian *et al.* (68) used pairs of conductors at the end of a channel to investigate the performance of pSi particles loaded with SP. Here, the open-circuit conductors interacted with the ionised gases of the flame front to complete the circuit (the “wire-make” method), enabling detection of the time of arrival and calculation of the velocity of the system to be 2484 m.s^{-1} .

Thiruvengadathan *et al.* (69) took an alternative approach to burn rate determination by preparing amorphous and crystalline Si nanoparticles (prepared in a DC arc discharge reactor) and mixed with SP particles by ultrasonic mixing. These energetic mixtures of nanometric sized Si particles were confined within a transparent tube (3.2 mm internal diameter) and initiated by a high voltage spark at one end. The reacting front was monitored by a series of fibre-optic probes placed laterally against the side of the tube, and with the time-of-arrival at each probe recorded via an amplified photodiode. This technique yielded burning rates between 200 and 1400 m.s^{-1} depending on the particular formulation tested. While the use of a single photodetector to record the time response of optical emission from the burning pSi yields little valuable information, the strong emission from the reaction combined with multiple probes at known distances provides for a simple measurement technique able to be employed at laboratory scale, as has been clearly demonstrated by Thiruvengadathan *et al.* (69).

An interesting method of characterising the performance of pSi energetics was put forward by Nguyen *et al.* (78). Confining wafers of pSi loaded with SP in a Teflon cell (internal volume 5.6 cm^3) with a venting nozzle of variable diameter, they exploited the production of gas

generated upon combustion of the pSi EM to effectively generate a propulsion system akin to a rocket motor. Varying both the quantity of energetic material present, and nozzle diameter, they recorded the vertical height that the cell would jump to upon ignition, thereby calculating the impulse of the system. While this is an unconventional method of analysis, it does demonstrate the potential for pSi EM's to function as a small rocket thruster, without measuring the actual burning rate directly.

Of the methods of analysis described, time-resolved optical emission seems to have not been used since about 2008. Since then use of high-speed video has dominated the published research. In addition to the works cited here previously, this technique has formed the major analytical basis for research by Abraham *et al.* (43), Parimi *et al.* (57, 58, 60), Piekel *et al.* (22, 61, 62), Terry *et al.* (79), and Yarrington *et al.* (80). The use of spaced velocity probes has been limited to Becker *et al.* (45) and Thiruvengadathan *et al.* (69).

1.4.2.4 Microstructural influences on the behaviour of pSi energetic materials

It is evident from the preceding discussion that the morphology of the pSi surface influences the performance of the energetic material. Altering the etching conditions will alter the diameter and density of the pores, the thickness of the porous layer, the specific surface area able to react with the oxidising agent, and the ability to infiltrate the oxidising agent into the pores. A summary of the etching conditions used in the works surveyed for this Chapter is presented in Table 1-1. Together these parameters will strongly influence the ability for an oxidising agent to infiltrate the pores, to control the final stoichiometric ratio of the mixture and the intimacy of mixing of the two reactants.

Table 1-1: Summary of silicon wafer etching conditions.

Source	Si type (dopant)	Resistivity ($\Omega\cdot\text{cm}$)	Etchant ^a (% HF v/v)	Etch current ($\text{mA}\cdot\text{cm}^{-2}$)	Etch time (min)	Porosity (%)	Pore size (nm)	SSA ($\text{m}^2\cdot\text{g}^{-1}$)	Thickness micron	Oxidising agent
Abraham <i>et al.</i> (43)	p (boron)	1-10	36 (with addition of 2.5% H_2O_2)		5-30	63-72	2.7-3.1	777-983	24-26	SP, S, $\text{Gd}(\text{NO}_3)_3$, $\text{Mg}(\text{NO}_3)_2$, $\text{Ca}(\text{NO}_3)_2$, $\text{Mn}(\text{NO}_3)_2$, KIO_4 , NaIO_4 , I_2O_5
Becker <i>et al.</i> (44)	p	1-30	25 and 33	9-36	30	59-70	2.5-4.4		17	SP
Becker <i>et al.</i> (45)	p	1-20	36 and 32 (with addition of 2.5% H_2O_2)	18.5	30	65-83	2.4-2.9	830-910	65-95	SP
Becker <i>et al.</i> (46)	p	1-20	36 (with addition of 2.5% H_2O_2)	(galvanic 170 nm Pt layer sputter coated to surface)	30 or 60	62-69	2.6-3.0	680-710	63 or 156	SP
Bezuidenhout <i>et al.</i> (47)			HF / MeOH (unspecified concentration)	245-305						SP and PETN
Churaman <i>et al.</i> (50)	p (boron)	1-30	25 & 33	20	5-37	52-77	2.4-4.4			SP
Churaman <i>et al.</i> (51)	p (boron)	1-10	25	20	30		4		40	SP
Churaman <i>et al.</i> (49)	p (boron)	1-20	25 & 33	18.4 & 110-70	15-30	67 – 74	3.8	4.07 - 757		SP
Churaman <i>et al.</i> (48)	p (Boron)	1-20	33			74			130	SP
Clément <i>et al.</i> (37)	p	0.001-0.015		43.5-87	30-60	59-71			70-193	Perchlorates (Li, Ca, NH_4 , Na, Ag, Fe & K)
		10-30			30-60	54-67			72-160	Nitrates (Ca, NH_4 , Li, Ag, K)
		1-1000			20-80	49-59			57-125	KMnO_4 , $\text{K}_2\text{Cr}_2\text{O}_7$, S, HClO_4
Currano and Churaman (53)	p (boron)	1-10	25	18.5	30				33	SP
Currano <i>et al.</i> (52)	p (boron)	1-10	25	10-40	< 30	59-76	3.3-4.3	470-728		SP
Dawson (42)	p (boron)	3-6	40	11-45	30	56	9.7-14.7		15-20	SP, $\text{Al}(\text{NO}_3)_3$ and $\text{Gd}(\text{NO}_3)_3$, RDX

Source	Si type (dopant)	Resistivity ($\Omega\cdot\text{cm}$)	Etchant ^a (% HF v/v)	Etch current ($\text{mA}\cdot\text{cm}^{-2}$)	Etch time (min)	Porosity (%)	Pore size (nm)	SSA ($\text{m}^2\cdot\text{g}^{-1}$)	Thickness micron	Oxidising agent		
Du Plessis and Conradie (19)	p	0.01-0.02	15, 25 & 35	25-80		70	2.3	279	52	SP, Gd(NO ₃) ₃ , S		
		0.2-0.3					3.4	188	57			
		20-100					8.2	78	39			
Du Plessis (63)	p	0.01-0.02	15-35	76		60-90	2.3	279		SP, Gd(NO ₃) ₃ , S		
		0.2-0.3					3.4	188				
		20-100					8.2	78				
Du Plessis (64)	p	0.01-0.02	15-35	76		82	3.0	181	30	SP, Gd(NO ₃) ₃ , S		
		0.2-0.3					68-81	2.3-6.3	89-260			
		20-100					68-91	4.2-7.7	59-143			
Du Plessis (65)	p	0.01-0.02	20	76		70	2.3	279	52	SP, Gd(NO ₃) ₃ , S		
		0.2-0.3					65	3.4	189		57	
		20-100					85	8.2	77		39	
Lazarouk <i>et al.</i> (41)	p (boron)		48	10-100					15-100	KNO ₃		
Lazaruk <i>et al.</i> (23)	p (boron)		48	10-100	10-60				5-175	KNO ₃		
Mason <i>et al.</i> (76)	p	0.001-0.005	25	60.1-76.5	60	55-90			125-141	SP, Ca(ClO ₄) ₂ , S, PFPE		
Mikulec <i>et al.</i> (40)	n (phosphorous)	4	25	50 ^b	15		1000		25	Gd(NO ₃) ₃		
Morris <i>et al.</i> (54)			45 (with addition of 2.5% H ₂ O ₂)	(Galvanic)	20		3-5	1000	75	SP		
Nguyen <i>et al.</i> (78)	p		43	80	7-25	60-75	2-5		45-118	SP		
Ohkura <i>et al.</i> (56)	p	0.1-0.9	24-32	50	2-40	50-70	4-12		5-50	Nil (freestanding film only)		
Parimi <i>et al.</i> (57)	p (boron)	0.001-0.005	25			60	30	310	140	SP, Mg(ClO ₄) ₂ , Ca(ClO ₄) ₂		
	n (arsenic)	0.001-0.005									62	423
	p (boron)	10-20										145
	n (phosphorous)	2-5									(front side illumination)	644

Source	Si type (dopant)	Resistivity ($\Omega\cdot\text{cm}$)	Etchant ^a (% HF v/v)	Etch current ($\text{mA}\cdot\text{cm}^{-2}$)	Etch time (min)	Porosity (%)	Pore size (nm)	SSA ($\text{m}^2\cdot\text{g}^{-1}$)	Thickness micron	Oxidising agent
Parimi <i>et al.</i> (58)	p	>1	30			67		730	35	SP
Parimi <i>et al.</i> (59)	p (boron)	0.001-0.005	25	40-80	60-90	73-75	17.1-18.9	271-284		SP, Mg(ClO ₄) ₂ , LiClO ₄
	n (arsenic)	0.001-0.005		40	90	74	5.2	439		
	p (boron)	10-20		40-60	30-60	62	11.2	522-644		
	n (phosphorous)	2-5		20 (FSI)	60	42	5.4	236		
Parimi <i>et al.</i> (60)	p (boron)	0.001-0.005	25	20-100	45-60	72-75		312	170	Mg(ClO ₄) ₂
Piekel <i>et al.</i> (22)	p (boron)	<0.01	12-36	(galvanic etching)	10	49-75	6.4-14.9	191-475	17-54	SP
		1-10	25-47			63-80	2.6-5.1	770-901	21-67	All etchants included 2.5% H ₂ O ₂
		>30	25-46			56-69	2.6-4.8	307-686	26-61	
Piekel <i>et al.</i> (61)	p (boron)	1-10	25-47	(galvanic etching)	10	63-80	2.6-5.1	770-910		SP
										All etchants included 2.5% H ₂ O ₂
Piekel <i>et al.</i> (62)	p (boron)	1-10	36	(galvanic etching)	10	70-72	3.1-3.3	850-900	19-47	SP
										Etchant included 2.5% H ₂ O ₂
Subramanian <i>et al.</i> (68)			HF / HNO ₃	(stain etching)			0.5-0.8	41-143		SP, Fe(NO ₃) ₂ , CuO, Bi ₂ O ₃ , pSi produced by stain etching of unspecified Si microparticles.
Wang <i>et al.</i> (70)	p (boron)	0.1-0.3	30	200	20-240	71	2-6	587	100-400	SP
Wang <i>et al.</i> (71)	p (boron)	0.1-0.3	30	100	15		2-7		80-86	SP
Wang <i>et al.</i> (72)	p (boron)	0.1-0.3	30	104	10	71	2-7	587	34-35	SP, NH ₄ ClO ₄

a. Unless specified, all etchants consist of HF diluted with ethanol, expressed as the volumetric percentage for HF.

b. Samples etched by Mickulec *et al* on n-type silicon were assisted by front-side illumination from a tungsten lamp at an intensity of 50 mW/cm².

Lazarouk *et al.* (41) noted that for pSi loaded with potassium nitrate the intensity of the reaction (measured by time resolved optical emission) increased significantly when the samples were etched deeper than approximately 60 μm , changing from a burn to an explosion. It was concluded that the thicker layers of pSi were able to more effectively trap the heat released by the energetic reaction (instead of the heat conducting quickly away to the supporting substrate in thinner samples), thereby contributing to self-heating of the system and enhanced reaction intensity. This was continued when they found that intensity of the explosion (inferred from the maximum diameter of the fireball recorded on high speed video) increased linearly as the thickness of the pSi layer increased from 5 to 175 μm (23). They further noted that the intensity of the reaction was greatly influenced by the age of the sample. Freshly etched samples exhibited fireball diameters approximately four times larger than the same samples stored in sealed vessels at 100% humidity, attributing the reduced performance of the aged samples to desorption of hydrogen from the porous surface accompanied by partial oxidation.

Becker *et al.* (44) found that p-type Si (1-30 $\Omega\cdot\text{cm}$) etched with either 25 or 33% HF diluted with ethanol produced pSi with pore diameters between 3.5 and 4.4 nm. They observed that porous layers etched at 36 $\text{mA}\cdot\text{cm}^{-2}$ became unstable and were subject to spontaneous flaking at thicknesses approaching 57 μm , noting that this effect was more pronounced for samples with larger pore diameters. They further found that the effect was minimised if the samples were either annealed at 300 $^{\circ}\text{C}$ for 1 h, or using pentane as the final solvent to wash the samples at the end of the etching process. Bouchaour *et al.* (81) had already determined that mechanical stresses within the porous layer could be strong enough to cause the pSi layer to

crack and break-up during drying, and that choosing a low surface tension volatile solvent significantly minimised these effects.

Du Plessis (63–65) studied the influence of pore diameter on the energetic reaction of pSi, across the range 2.3 to 8.2 nm, finding 3-4 nm pores produced the most intense reactions for sodium perchlorate, gadolinium nitrate and sulphur. This was found to be optimised for low-doped p-type Si (0.2-0.3 Ω .cm), etched in 30% HF diluted in ethanol to produce 3.4 nm pores, 65% porosity and with a layer thickness of 57 μ m.

Mason *et al.* (76) found that highly doped p-type Si (1-5 m Ω .cm) samples etched at current densities of between 60 and 75 mA.cm⁻² for up to 1 h would produce pSi layers up to 141 μ m thick and with porosities between 55 and 90%. It was found that samples with porosities greater than 80% were highly unstable, exhibiting the same microscopic fracturing and flaking described by Becker *et al.* (44). They found that this could be alleviated by using a paused etching regime, whereby current was applied for 10 min, followed by a 3 min pause to allow H₂ gas generated during etching to escape the pores, with accompanying ingress of fresh electrolyte. Both SP and calcium perchlorates were investigated as oxidising agents, with velocities recorded to be between 222 and 287 m.s⁻¹. Interestingly, Mason *et al.* (76) also investigated the effect that confinement would have on the system. By placing a glass microscope slide against the burning face of the pSi, they were able to observe a slight increase in the burning rate – pSi (55% porosity) loaded with SP increased from 284 to 327 m.s⁻¹. In this instance, the confining layer was not clamped to the surface, being held in place only by its own weight. Such confinement could be considered to be quite weak, and may not

offer as much of an enhancement in the burning rate as could otherwise be achieved from a more rigid system.

Churaman *et al.* (49) found that samples of pSi prepared at 67 and 74% porosity, displaying otherwise very similar pore diameters (3.4 and 3.8 nm respectively), recorded burning rates up to $1000 \text{ m}\cdot\text{s}^{-1}$ for the lower porosity and up to 2000 m/s for the higher porosity. Using frame-by-frame analysis of high-speed video, they observed occasional spikes in the velocity of these samples, peaking at $6710 \text{ m}\cdot\text{s}^{-1}$ for one sample. However this was inconsistent with the average velocity across the entire of the sample length. Such spikes were attributed to interaction of a longitudinal reaction wave progressing through the sample, but no specific mechanism was proposed.

Churaman *et al.* (51) studied pSi surfaces (4 nm pores, $40 \mu\text{m}$ thick layer) loaded with SP in an attempt to discover the mechanism of the reactions. Samples were studied using time resolved light output (recorded by photodiode), differential scanning calorimetry, and infrared spectroscopy. Their results indicate that at low temperatures, the explosive oxidation reaction of the pSi surface occurs as a result of reaction of radical silicon species. Since the Si-Si backbond is weaker than the Si-H bond, oxidation will occur preferentially at this location. However, this hydride layer prevents migration of oxygen species into the bulk, thereby acting as a protective stabilising layer. Churaman *et al.* (51) reasoned that in order for the energetic reaction to initiate, the surface hydride layer must be breached, an observation that supports the earlier theory proposed by Kovalev *et al.* (39). Once breached, unsaturated Si radical species will react further with O and OH radicals, progressing into the silicon

material in a chain reaction accelerating to explosive speeds, forming Si-O, SiO₂, Si-OH and H₂O. The oxygen reacting with the silicon is believed to originate from either dissociation of the SP itself or dissociation of the water of crystallisation associated with this particular oxidising agent.

Parimi *et al.* (60) appeared to be the first group to exploit the hierarchical structure of a pSi surface to control the behaviour of the burning. Initially they found that pSi (produced from heavily doped p-type Si (boron doped, 1-5 mΩ.cm) yielded burning rates of between 1 to 8 m.s⁻¹, whereas low doped p-type Si (phosphorous doped, 2-5 Ω.cm) yielded burning rates of “...several hundreds of metres per second.” Here, samples were etched to depths of approximately 170 μm, porosities 72 to 75% with SSA of ≈ 312 m².g⁻¹, and used Mg(ClO₄)₂ as the oxidising agent. They observed that heavily-doped silicon would often produce neat pSi layers free of defects, whereas low doped wafers had a propensity for producing highly cracked pSi layers. Their theory was that “.... *the nanoporous silicon structure, in combination with the micron scale crack pattern resulted in the enhanced propagation speeds observed.*”

Noting that most previous work concentrated on monolithic bulk structures of pSi, Parimi *et al.* (60) employed deep reactive ion etching (DRIE) to form an array of micro pillars in the heavily-doped Si wafer, approximately 35 micron tall, 20 x 20 μm² spacing, prior to etching in HF / EtOH. In this way, they induced micron scale defects in the heavily-doped substrate to replicate the naturally occurring defects observed in the low-doped substrate. The flame velocity in the unpatterned areas of the pSi was recorded at <3 m.s⁻¹, but accelerated to over

500 m.s⁻¹ in the patterned areas. This enabled them to conclude that convective burning was the dominant force driving flame propagation through pSi, an effect enhanced by structural defects within the pSi structure. They further proposed that such an effect might be exploited by designing pSi patterned arrays to tailor the behaviour of the system to a desired application.

This work was followed by Piekel *et al.* (62) who used pattern etching to create a series of microchannels through the pSi. Using DRIE, channels approximately 50 µm wide and 50-60 µm deep were formed in the Si wafer prior to etching pSi. Such channels were formed either parallel or perpendicular to the direction of the intended flame travel. The pSi layer had a depth of ≈20 µm, 70-72% porosity, 3.1-3.3 nm pore diameter, and a SSA of between 850 – 900 m².g⁻¹. These configurations are depicted in Figure 1-7 and Figure 1-8.

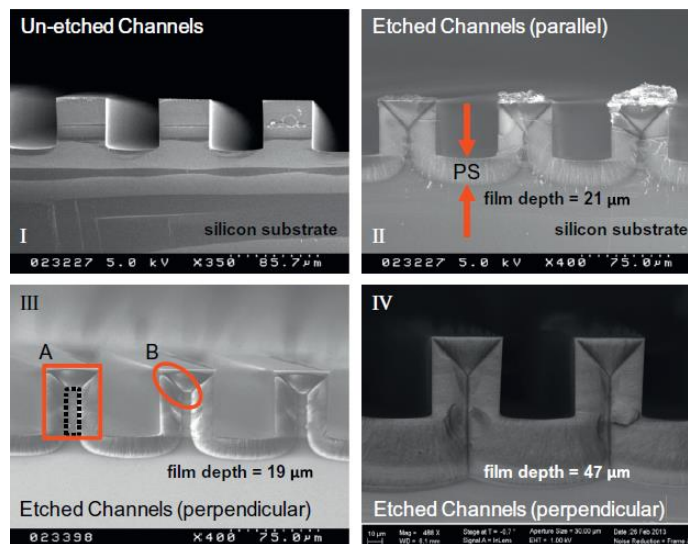


Figure 1-7: SEM images of microscopic channels formed and etched with pSi, providing enhanced flame velocity in pSi energetic materials (62).

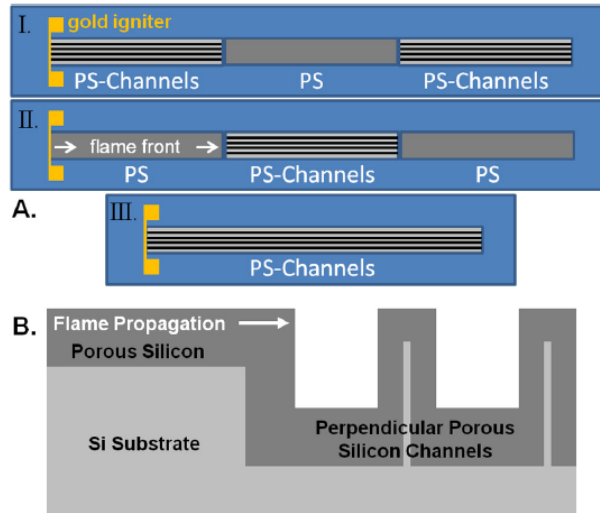


Figure 1-8: Configuration of patterned channels formed within pSi for flame speed enhancement experiments. Channels were formed either perpendicular or parallel to the direction of travel of the flame (62).

They observed that the flame speed increased by approximately 900 m.s^{-1} through either channel configuration compared to neat pSi ($1950 - 2480 \text{ m.s}^{-1}$ for various samples) (62). The enhancement along parallel channels could be explained by convective processes guiding the flame along the channels. However the enhanced flame speed was equal to that across the perpendicular channels. It was proposed that the flame could skip across the tops of the perpendicular channels instead of through the convoluted path along the walls and base of the channel, but they concluded that this could not adequately explain the equal enhancement for either configuration. Correlating this to the acoustic velocity through pSi at these porosities ($1600 - 2400 \text{ m.s}^{-1}$ depending in the type of wave), they concluded that the enhancement was not due simply to convective processes of flame travelling along the channels, but that the etched channels were able to mechanically weaken the bulk structure permitting passage of an acoustic wave in a manner not possible in unpatterned pSi with greater mechanical stability. That the energy transmitted by this wave was sufficient to ignite the pSi suggests the material

is undergoing either true detonation or some form of semi-stable pre-detonation process, instead of a mere deflagration, under these conditions, driven by enhancement of the acoustic velocity within the microchannels.

Piekel *et al.* (22) later conducted an extensive survey of the influence of porous microstructure on the performance of pSi energetic materials. Studying pSi loaded with SP at porosities between 49 and 80%, SSA's of between 191 and 901 $\text{m}^2.\text{g}^{-1}$, pore diameters between 2.6 and 14.9 nm, and depths of between 17 and 67 μm , they drew the following main conclusions:

- That the smallest pore sizes inhibited oxidant penetration and thereby produced slower flame speeds;
- That high flame speeds were directly correlated to high specific surface area of the pSi, but were poorly related to porosity alone, and
- That under the etching conditions studied, there is a highly interdependent relationship between pore size, porosity, pore depth and SSA.

These relationships are presented in Figure 1-9. The peak velocity measured here was 1950 $\text{m}.\text{s}^{-1}$ for a sample at 72% porosity, 3.2 nm diameter pores, SSA of 895 $\text{m}^2.\text{g}^{-1}$ and depth of 36 μm .

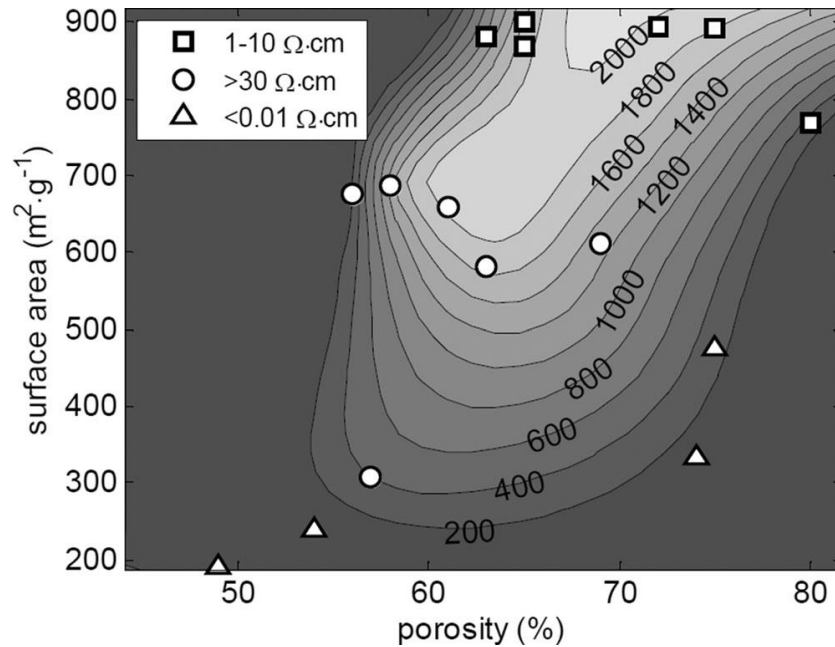


Figure 1-9: Relationship between SSA, porosity and burning rate (22).

In this work, Piekel *et al.* (22) noted that the sample with the highest porosity (80%) achieved a flame velocity of only $330 \text{ m}\cdot\text{s}^{-1}$. While it might seem favourable to have a higher porosity to permit a greater volume into which more oxidising agent can be loaded (thereby moving the system to a more balanced stoichiometry), the velocity was clearly much lower than more fuel rich samples at lower porosities. They attributed this lower velocity to cracks and fissures observed in the pSi layer believed to form channels into which the oxidising agent would preferentially deposit. These cracks were not measured but appeared to be micron sized, compared to the nanometre scale of the pores. It was thought that such relatively thick layers of SP deposited within the pores would provide a barrier to flame transmission, thereby reducing the velocity.

Wang *et al.* (70) demonstrated that production of thick layers of uncracked pSi were able to be produced reliably by etching p-type Si (0.1-0.3 $\Omega\cdot\text{cm}$) in 25% HF / EtOH at a relatively high current density of 200 $\text{mA}\cdot\text{cm}^{-2}$. Etch durations of up to 60 min were able to produce pSi layers approximately 205 μm thick, 4.3 nm average pore diameter, 71% porosity with SSA of 587 $\text{m}^2\cdot\text{g}^{-1}$. The high quality of their surfaces appeared to be related to careful drying of the substrate having been cleaned with EtOH after etching. Clearly, thick layers of pSi are able to be produced in a manner which are stable and of high quality.

1.4.2.5 Investigations of the reaction mechanisms and the deflagration vs detonation debate

Yarrington *et al.* (80), examined the burning behaviour of Si microparticles (i.e. unetched Si powder with average particle size 2.5-3.0 μm) mixed with PTFE particles as the oxidising agent (having a composition of Si:PTFE of 26:74 wt.%). The reactivity of the mixture was determined by measuring the burning rate and further inferred using differential scanning calorimetry to determine the activation energy of the system by applying the Kissinger method (82). They concluded that the type of the dopant used for the Si powder (i.e. n-type or p-type dopants) had no effect on reactivity. However, increasing the concentration of the dopant increased the reactivity by increasing the burning rate from 2.1 to 3.0 $\text{mm}\cdot\text{s}^{-1}$ for low and high doped substrates. While not directly comparable to a pSi system, these results are interesting in that they demonstrate the influence dopant atoms have on the combustion process. Although they could not clearly explain this process, they proposed that increasing the dopant concentration would either increase the thermal diffusivity of the system, or alternatively increase the redox potential of the Si particles to permit greater electron interaction with oxidant species.

Parimi *et al.* (57) followed this and considered the effect of dopant type and concentration on the burning of pSi. Samples of low- and highly-doped Si were etched to produce pSi of various morphologies. Similar to their previous work (60), they again noted that low-doped substrates (of either n- or p-type) produced surfaces prone to cracking and thereby demonstrated the highest burning rate, when compared to heavily doped counterparts. It was therefore concluded that dopant type and concentration had most influence on the burning rate by affecting the nature of the pSi pore morphology instead of any other factor. They developed this further by considering the concentration of oxidising agent within the pores (i.e. the bulk concentration of the mixture in total). Porous layers were loaded to varying degrees up to 100% of their volumetric capacity. They found that for otherwise equivalent pSi samples loaded with $\text{Ca}(\text{ClO}_4)_2$, those which were loaded to 56% of their maximum capacity had burning rates $0.7\text{-}1.2 \text{ m}\cdot\text{s}^{-1}$, compared to samples loaded to only 12 % of their final capacity yielded burning rates of $4.2 - 4.3 \text{ m}\cdot\text{s}^{-1}$. It was proposed that this apparent enhancement achieved by under-loading a sample could be considered as follows:

- Reaction between Si and the oxidising species occurs at a temperature far below the melting point of either component,
- Reactions between the species will occur quickly in a thin reaction zone at the interface of the pore and the solid oxidising agent,
- Further reactions between the species beneath this interface is diffusion limited at a rate governed by expulsion of gaseous reaction products (specifically SiO gas) to expose fresh surfaces, and that this occurs on significantly longer time scales than the reaction at the interface zone,

- That the energy absorbed by the mass of unreacted oxidising agent within the pores will lower the temperature of the system. In other words, completely filling the pores provides a greater thermal mass able to absorb the heat of the reacting interfacial zone, reducing the temperature gradient able to drive the reaction through the bulk of the material.

This is important because while it seems counterintuitive that less oxidising agent will contribute to higher burning rates, the analysis by Parimi *et al.* (57) demonstrates that the major driving force behind the high burning rate sometimes observed is directly related to the intimacy of the contact between the oxidising agent and the pSi fuel. This can be extended to observations that for uniform (uncracked) pSi surfaces, the highest velocities are observed at high specific surface areas. Heat released in this initial reaction drives a conductive burning process through the material, supported by slower convective processes through unfilled pore voids or through the microscale structure.

The same group continued their examination with patterned microstructures within the pSi surface, applying shadowgraphy to directly observe transit of both shockwaves and flame through pSi loaded with SP (58). Again, patterned micropillars were formed within the heavily doped Si using DRIE prior to pSi etching. Burning rates were recorded to be 4.6 m.s^{-1} in unpatterned regions, but up to 137 m.s^{-1} across the micropillars. Simultaneously the shock created by the explosion in the air above the pSi was directly observed, and was measured to be propagating with a velocity of 419 m.s^{-1} . Decoupling of the shockwave from the flame front in this manner was interpreted as strong evidence for convective heat transfer driving progress of the flame front, instead of interaction with the shockwave (i.e. detonation).

Parimi *et al.* (58) extended this research and etched low doped Si substrates (SSA 730 m².g⁻¹, 67% porosity, 35 μm thick), loaded with SP. No difference was observed when they reduced the atmospheric pressure in the explosion chamber to 0.1 atm, or replacing air with He (to lower the density and thereby reduce the Mach number of the external shockwave). Burning rates were recorded to be 1162 m.s⁻¹ in air (1 atm), 1324 m.s⁻¹ in air (0.1 atm), and 1279 m.s⁻¹ in He. It was therefore concluded that because the burning rate was substantially independent to the shockwave above the surface, intrinsic factors within the pSi layer were dominant factors driving flame progress through the material. The longitudinal speed of sound in their pSi surfaces, measured by acoustic microscopy, was determined to be between 2169 and 2479 m.s⁻¹, far higher than the burning rate of the reacting pSi (1162 m.s⁻¹ in air). This observation is strong evidence for a sub-sonic deflagration within the pSi instead of a supersonic pre-detonation process as concluded by Piekel *et al.* (62) and Becker *et al.*(45). Parimi *et al.* (58) further concluded that the combination of conductive and convective burning within pSi are enhanced by mechanical fracture of the pSi due to internally generated gas pressure, permitting the flame to progress through these fissures combined with creation of free radicals within the pSi at the fractured faces.

Abraham *et al.* (43) examined a variety of nitrates and sulphur loaded into pSi surfaces (63-72% porosity, 730-900 m².g⁻¹, 2.8-3.2 nm diameter pores, ≈26 μm thick pSi layer). Here, burning rates were typically less than 10 m.s⁻¹, except for Mn(NO₃)₂ which displayed a burning rate of 21 m.s⁻¹. Interestingly they ignited the sulphur based system in both air and inert (N₂) atmospheres. They noted that there was significantly less flame emitted from the

system ignited in N₂, compared to when ignited in air, but that the burning rates were the same (2.9 and 3.0 m.s⁻¹, respectively). This flame was attributed to afterburning reactions of the initial reaction products combusting with atmospheric oxygen. Whilst the afterburning will contribute to the bulk performance of a discrete device it does not alter the intrinsic properties of the burning pSi itself. So, comparing this to the observations by Parimi *et al.* (57) that sub-optimal loading provided enhanced burning compared to a maximally loaded sample, bulk performance might actually be enhanced if pores are maximally loaded to provide sufficient oxidising agent to contribute to afterburning in a hermetically sealed device.

1.4.3 Applications of porous silicon energetic materials

Common to all of the recent work is a desire to apply pSi energetic materials to micro-electromechanical systems. Such systems are of enormous importance to a wide variety of end users in the private and defence industries (83). As outlined by du Plessis (84), the advantage of using existing silicon industry manufacturing techniques enables production of complex yet low cost miniaturised explosive elements.

One of the earliest applications of pSi energetic materials, proposed by Mikulec *et al.* (40), was to use the heat released during the reaction to form the basis for a field portable atomic emission spectrometer. Here, reaction of the pSi energetic material could be used to energise analytes loaded onto the surface sufficiently to cause emission which could then be recorded, as described in their patent (85).

Clément *et al.* (37) used patterned mask etching to produce a series of small (approx. 5 mm²) elements which were etched to form pSi. Individual elements were cut and fabricated into prototype airbag initiator elements.

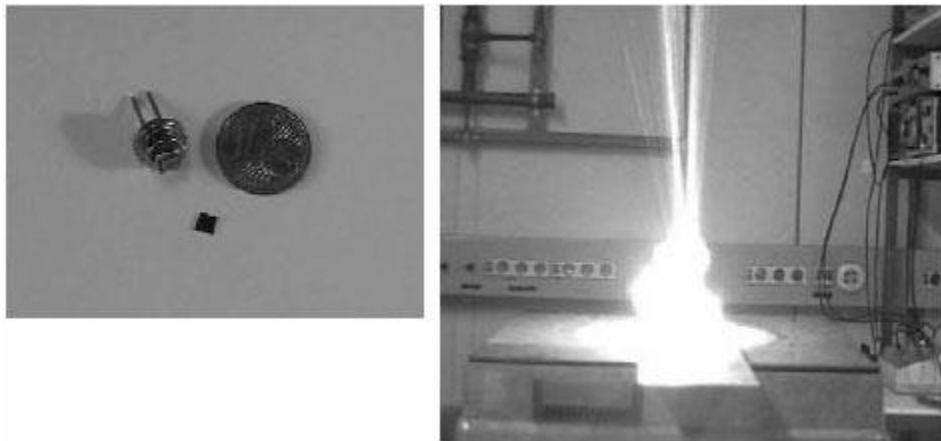


Figure 1-10: Airbag initiators fabricated by Clément *et al.* (37).

Du Plessis and Conradi (19) first described their use of pSi energetic elements for initiation systems, and further described this as an energetic element on the back side of an integrated circuit fabrication (63). Here, the application considered was to create the initiation element for electronically controlled delay detonators for use in the mining industry. In this case, an aluminium bridgewire (150 µm wide, 1 µm thick, 600 µm long) was used to initiate pSi loaded with SP in less than 100 µs with low power electric pulses (800 µJ @ 20A for 10 µs), providing better precision compared to conventional bridgewire systems.

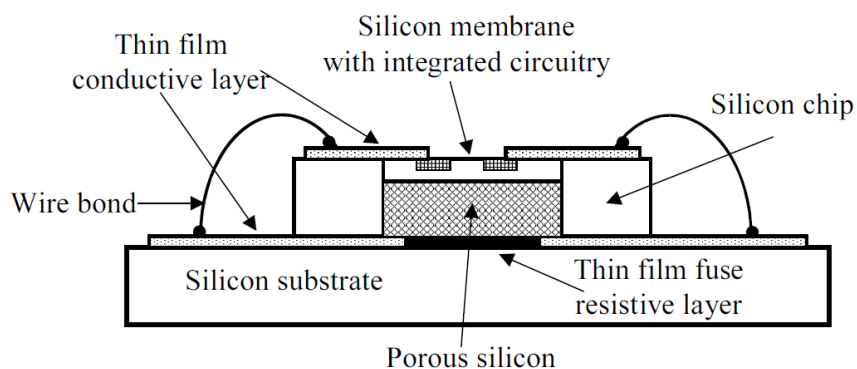


Figure 1-11: Fabricated integrated circuit incorporating a pSi explosive element (63).

The Churaman group also described energetic devices incorporating integrated pSi elements (49, 50). Here, they found strong prompt ignition of the pSi by heating a gold or platinum bridgewires (12.5 to 50 μm wide, up to 125 μm long, 2 μm thick) sputter-coated onto the surface of the pSi. Voltages as low as 2.8 V were sufficient to heat the bridgewire sufficiently to cause ignition of the pSi. Currano and Churaman (53) continued this work and improved the system by fabrication using layers of chromium, platinum and gold, combining increased adhesion to the pSi (due to the Cr) with enhanced thermal and electrical properties of the Au / Pt. This system was able to produce prompt ignition of pSi loaded with SP to generate pressure pulses of up to 3.5 kPa, ejecting hot particles and flames able to ignite further parts of the explosive train.

As an alternative to electrical bridgewires, Churaman *et al.* (48) created ignition systems incorporating pSi energetic materials that could be initiated using focussed lasers at 514 nm (continuous wave, 37.7 mW) as the first element in an ignition train. By isolating the

energetic material from physical contact, such as is required by attaching a bridgewire to the surface, they felt that this could afford improvements in the safety and security of the system.

Common to all of these applications is recognition that pSi energetic materials are used as the primary energetic material in some explosive train (28).

1.5 Summary

Porous silicon is a highly ordered surface that is formed as a result of the electrolytic etching of a silicon wafer in a hydrofluoric acid electrolyte. Through the control of simple parameters such as wafer resistivity, electrolyte concentration, etching current and etching time, one can create a tailored surface with a very high internal surface area. The exothermic reaction of the pSi with an oxidising agent impregnated into the pore network proceeds at very high rates resulting in an explosion of the bulk sample.

From the work reviewed above, the following can be summarised about the system:

- n-type silicon has found application in pSi energetic materials, however p-type substrates dominate the published research;
- Low doped substrates tend to produce surfaces with the highest porosities and finest pore structures (small pore diameter and high SSA), but these surfaces are prone to degradation after etching, causing the surface to disintegrate into tiny flakes;

- While sodium perchlorate is the dominant oxidiser in use in combination with pSi, various oxidising agents are available, most commonly impregnated into the pores as a solution in a volatile low viscosity solvent (e.g. methanol);
- Burning through the surface takes place as a combination of conductive and convective processes leading to an explosive behaviour known as deflagration. Burning rates vary from as low as a few metres per second to over 1000 m.s^{-1} ;
- Micron-scale structural defects in the pSi formed either as a result of post-etching degradation or deliberately through patterned etching techniques create fissures which promote convective burning and may lead to substantial increases in the burning rate to several thousand metres per second. Such high burning rates have been used as evidence of detonation within the material;
- Reaction between the pSi and oxidising agent occurs at the immediate interface of the two materials, often in the solid phase until gaseous reaction products are produced to drive the reaction forward through the bulk mixture;
- Accordingly, samples with high SSA demonstrate higher burning rates compared to lower SSA samples, and the burning rate is largely governed by the intimacy of contact between the two solid phase reactants;
- Filling the available pore volume with oxidising agent may decrease linear burning rates, however this is offset by an enhancement of the overall bulk scale properties of the energetic system;
- Pore sizes of $<10 \text{ nm}$ in diameter dominate the research into pSi energetic materials, and most work is carried out on samples within the 2 to 5 nm diameter range. Pores finer than 2 nm in diameter have proven to hamper oxidising agent infiltration and are therefore considered a poor choice for these applications.

1.6 Aims and scope of Thesis

A considerable body of work has demonstrated that energetic materials based on pSi are both simple and reliable. However there are a number of questions that remain unanswered. These materials appear to have been poorly characterised in the context of other materials used in real-world applications. Behaviours such as the sensitivity of the material, response to initiation stimuli, and the nature of the chemical reactions form an important part of the understanding of these materials. It is the aim of this Thesis to further explore the nature and behaviour of the energetic reaction between pSi and selected oxidising agents.

Some of the work presented in the following chapters has been cited by work discussed in this introduction, most notably in the field of burning rate measurements. Experimental techniques common to all aspects of this work are described in Chapter 2. Chapter 3 details work carried out to measure the burning rate of the system and the influence of microstructure on the burning rate. The response of pSi energetic materials to various stimuli, including characterisation of industry standard safety parameters is reported in Chapter 4, and a detailed examination of the response of the system to laser-based initiation is reported in Chapter 5. Chapter 6 presents an examination of the system with a view to determining the mechanism by which the reaction commences, including a novel correlation of calorimetric (DSC) and spectroscopic (FTIR) experiments. Chapter 7 presents a summary of the work and some thoughts on future research directions.

Chapter 2 EXPERIMENTAL TECHNIQUES

Experimental techniques relating to the preparation and characterisation of porous silicon energetic materials are described here. These techniques are common to all following chapters in this Thesis. Those techniques which are used and reported in only one of the following chapters, but have no applicability elsewhere, will be described in the relevant sections.

2.1 Manufacture and characterisation of porous silicon

2.1.1 Etching

Porous silicon (pSi) was manufactured using anodic electrochemical etching, in a technique described by Foll (3) and Halimaoui (10). Custom Teflon etching cells were manufactured to produce either circular (15mm diameter, 1.76 cm²) or elongated (8 x 45 mm, 3.79 cm²) etching areas. Figure 2-1 depicts a typical etching cell.

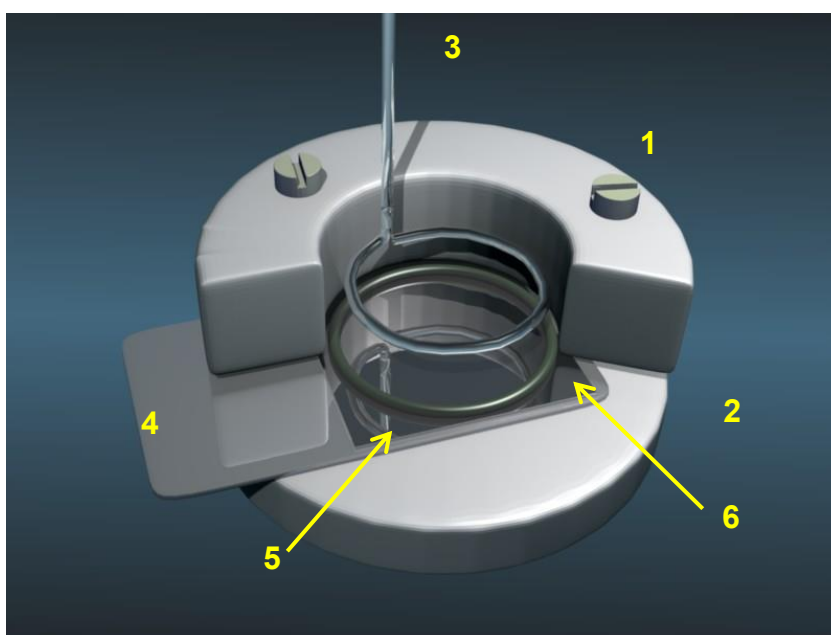


Figure 2-1: Example of a simple etching cell arrangement including Teflon cell top (1) and base (2), platinum cathode (3), backing anode (4), silicon wafer to be etched (5) and o-ring seal (6).

Silicon wafers (p-type boron doped, 3-6 Ω .cm, 385 ± 25 μ m thickness, <100> orientation, single side polished) were scribed and cut to a suitable size and assembled into the etching cell using a polished stainless steel anode and a platinum wire cathode. A Viton rubber O-ring was used to form a liquid seal on the front polished face of the wafer. Contact with the stainless steel anode was made simply by the force of clamping the etching cell together

without aid of any back-side treatment for the wafer (e.g sputter coated Ti / Pt layers , described by Churaman *et al.* (49)). The platinum cathode was maintained at a height of approximately 5 mm above the wafer.

Current was supplied either by Keithley 2612 or TTI PLH-250 laboratory power supplies, operated under constant-current mode, typically delivering current densities of up to 50 mA.cm^{-2} . The source meters were controlled using a custom Labview based software interface. During etching, the etching cell was operated within a PVC box, the hinged lid of which was fitted with electrical isolation connectors in order to disconnect the current if the lid was opened, thereby ceasing the etching immediately and preventing a safety hazard from the internal electrical connections.

Electrolytes were prepared from hydrofluoric acid (48% aqueous stock solution, Merck Chemicals), diluted to a final volumetric percentage concentration determined by the experimental parameters. Wafers were washed with ethanol (EtOH) (99% undenatured, AR grade) and acetone immediately prior to and after the etching process, and were dried in a stream of N_2 gas prior to being stored in a desiccator.

In order to create a separated film of pSi detached from the supporting wafer, it was necessary to implement an electropolishing step at the end of the main etch period. Here, the electrolyte would be removed and replaced with 5% HF diluted with ethanol. The etching current would be increased to 100 mA.cm^{-2} for a period of 5 seconds, in the manner described by

Salonen *et al.* (86). This step had the effect of aggressively etching the pSi at the base of the layer sufficiently to undercut the pores, thereby detaching the pSi from the supporting wafer.

2.1.2 Porosity measurement

Sample porosity represents the volume fraction of pores within the etched surface. This is determined gravimetrically using the technique described by Halimaoui (10):

$$P = \frac{m_1 - m_2}{m_1 - m_3} \quad \text{Equation 2-1}$$

where P is the porosity (expressed as a percentage), m_1 is the silicon wafer mass prior to etching, m_2 is the wafer mass after etching, and m_3 is the wafer mass after the etched layer is stripped away using a dilute potassium hydroxide solution.

2.1.3 Pore size measurement

Etched wafers were imaged on a Helios Nanolabs high resolution SEM. Samples were mounted onto aluminium stubs using conductive paste to minimise movement and drift during the image capture process. The instrument was typically operated at 10 to 15 kV with a working distance of between 2 to 4 mm. As pores under investigation were very fine (often less than 5 nm), samples were not prepared with a sputter coated conductive layer (e.g. platinum), and care needed to be taken to prevent interference from surface charging. A representative image of an etched surface is presented in Figure 2-2.

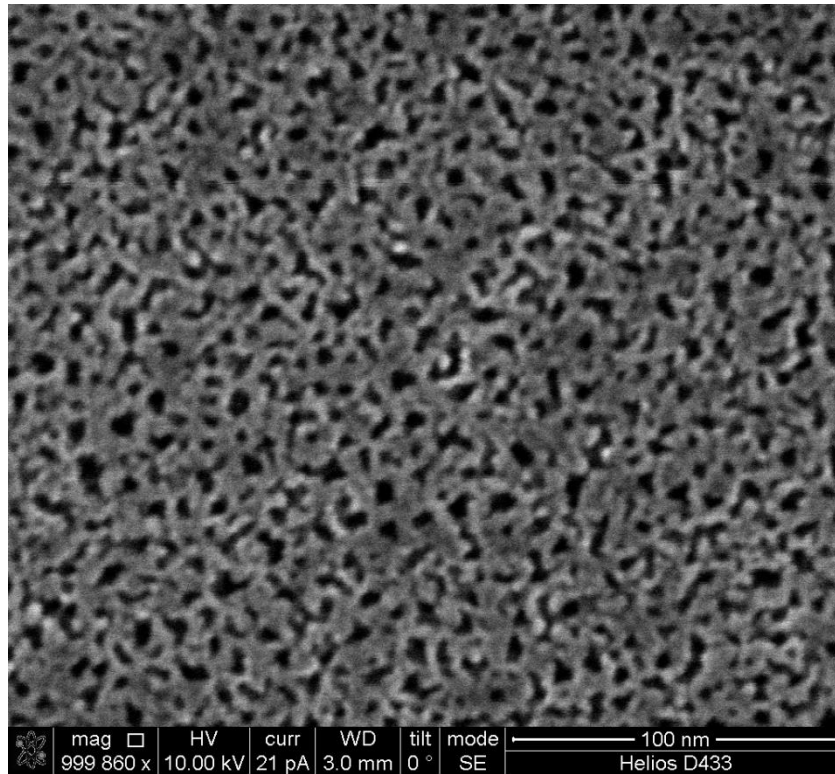


Figure 2-2: High resolution SEM image of pSi etched in 40% HF / ethanol, continuous current @ 22.7 mA.cm^{-2}

Each image was then processed using JMicrovision software to measure the perimeter of pore edges and calculate an equivalent circular diameter of the pores (87). Calculation of the pore diameter across a large number of pores within the image enabled the pore size distribution for that sample to be calculated. A detailed description of determining pore size distribution is presented in Appendix A.

2.1.4 Porous layer depth measurement

Etched wafers were snapped using a diamond scribe, and mounted vertically on an aluminium stub. These cross-sections were then imaged using a FEI Phenom SEM with the porous layer thickness measured directly using the operating software. A representative image is presented in Figure 2-3.

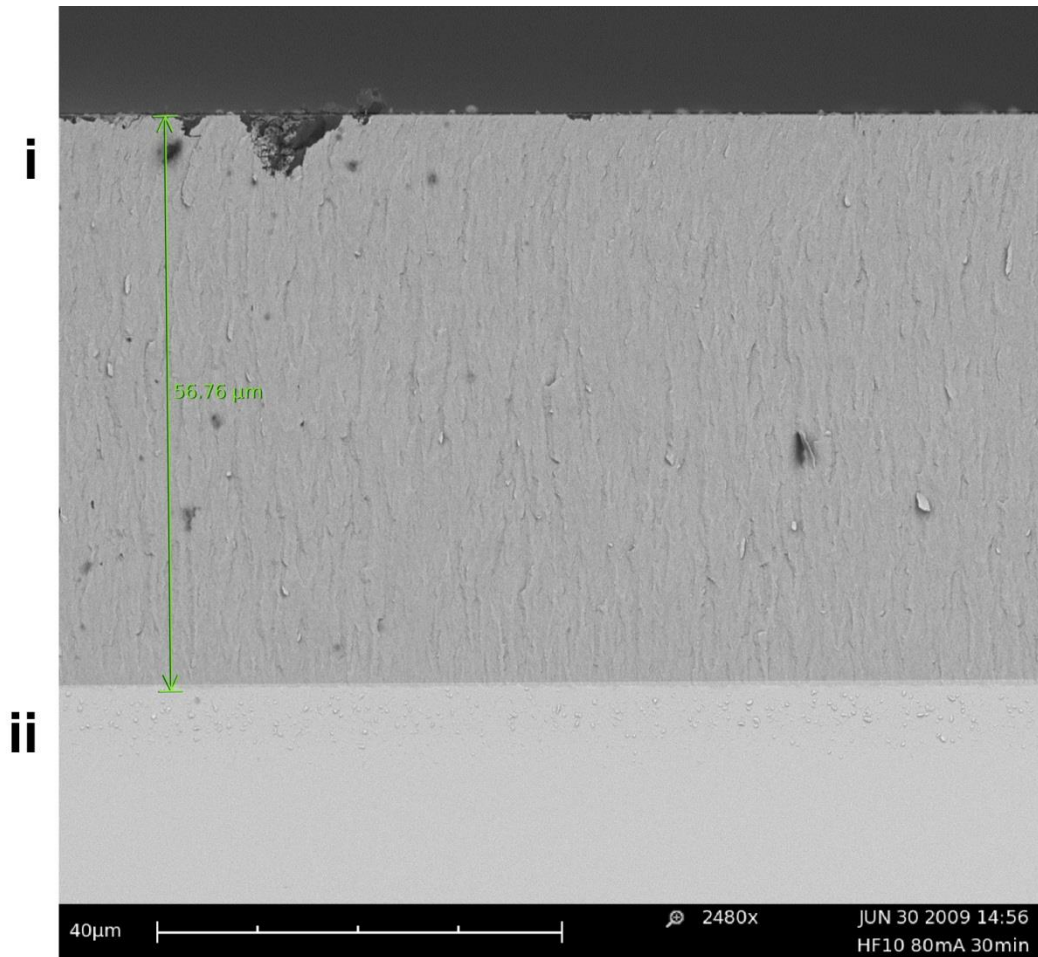


Figure 2-3: Cross-section SEM image of pSi etched for 30 minutes at $45 \text{ mA}\cdot\text{cm}^{-2}$ in 10% HF / ACN. The porous layer (Region i) is clearly visible above the supporting unetched Si wafer (Region ii).

2.1.5 Optimisation of the etching process

Initial efforts to produce high quality thick surfaces suitable for pSi energetic materials were problematic.

Small creases in the aluminium foil initially used as the anode to contact the backside of the Si wafer formed incomplete contact - this produced etched pSi of varying thickness and occasionally burnt through the entire thickness of the wafer as current was concentrated at and

around the high spots. It was found through trial and error that the use of a stainless steel plate (approximately 3 mm thick) was advantageous as the backing electrode compared to aluminium foil. The stainless steel electrode was able to be polished repeatedly with fine sandpaper against a hard flat surface to produce a face that was flat, uniform, and free of corrosion that would otherwise resist the applied current. Furthermore, the relatively large mass of the electrode acted as a heat-sink to help maintain evenly cool temperatures of the samples throughout the etching process. These factors helped to contribute to producing high quality reproducible pSi surfaces for the duration of the project.

The most common solvent used to dilute the HF electrolytes is EtOH (see Table 1-1). Initial efforts found that for long duration etches (e.g. >60 minutes of applied current) the porosity of the sample at base layers would increase due to depletion of HF in the electrolyte, degrading the pSi into a fragile flaky surface (Figure 2-4).

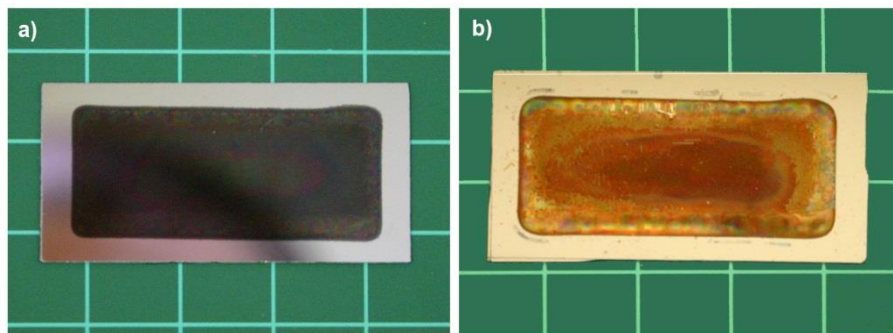


Figure 2-4: Typical appearance of (a) well-etched and (b) degraded pSi surfaces.

Kang *et al.* (11) investigated the use of acetonitrile (ACN) as an alternative to ethanol in the production of nanoporous silicon surfaces, concluding that more uniform and higher quality surfaces were produced in ACN based electrolytes.

An additional variable to consider was the use of pulsed current etching. As described by Escoria and Agarwal (88), and indicated by the reaction scheme shown in Figure 1-2, applied current which creates charge transfer holes within the Si is only relevant for one of the multiple reactions involved in pSi formation. By considering that these reactions occur predominately at the pore tip, combined with the difficulty in removing the evolved H₂ gas from high aspect-ratio pore structures (which will tend to insulate the surface of the pores), Escoria and Agarwal (88) found that low frequency pulsing of the applied current (1 to 100 Hz, 5 to 60% duty cycle) would permit the H₂ gas to escape the surface, refilling the pores with fresh electrolyte. This resulted in pSi surfaces which were deeper and had lower surface roughness compared to a constant DC profile.

To optimise the etching regime, pSi was prepared using 40% HF in either EtOH or ACN, and using either constant or pulsed current. Here, the current was pulsed at 66% duty cycle with a 15 second period (10 seconds on followed by 5 seconds off). Etching time was adjusted to equal 30 minutes of applied current. It is noted here that this pulsed current regime was selected due to convenience for calculation of experiment operational times, and that a full investigation of duty cycle optimisation for this system was beyond the scope of this Thesis. The porosity, pore depth and pore size distribution of these samples were determined using

the techniques detailed earlier in Section 2.1, and are presented in Table 2-1. Pore size distributions for these four conditions are presented in Figure 2-5.

Table 2-1: Comparison of etching conditions.

	Porosity (%) (n=3)	Pore size (nm)	pSi layer depth (μm) (n=3)
HF / EtOH, continuous current	54.2	5.2 \pm 1.7	24.7
HF / EtOH, pulsed current	53.6	5.2 \pm 1.5	28.7
HF / ACN, continuous current	53.0	5.0 \pm 1.3	27.5
HF / ACN, pulsed current	51.8	4.0 \pm 1.1	35.1

Compared to samples etched in EtOH based electrolytes, samples etched in ACN based electrolytes displayed marginally finer pores with a narrower pore size distribution, and a slightly lower porosity. However, samples etched in ACN yielded significantly thicker pSi layers. Furthermore, for both electrolytes, samples etched under conditions of pulsed current displayed slightly narrower pore size distributions and smaller median pore diameters coupled with increased layer thickness.

Accordingly, for all work in the following chapters, ACN was used as the diluting solvent for the HF, and all etching currents were pulsed with a 66% duty cycle and 15 second period.

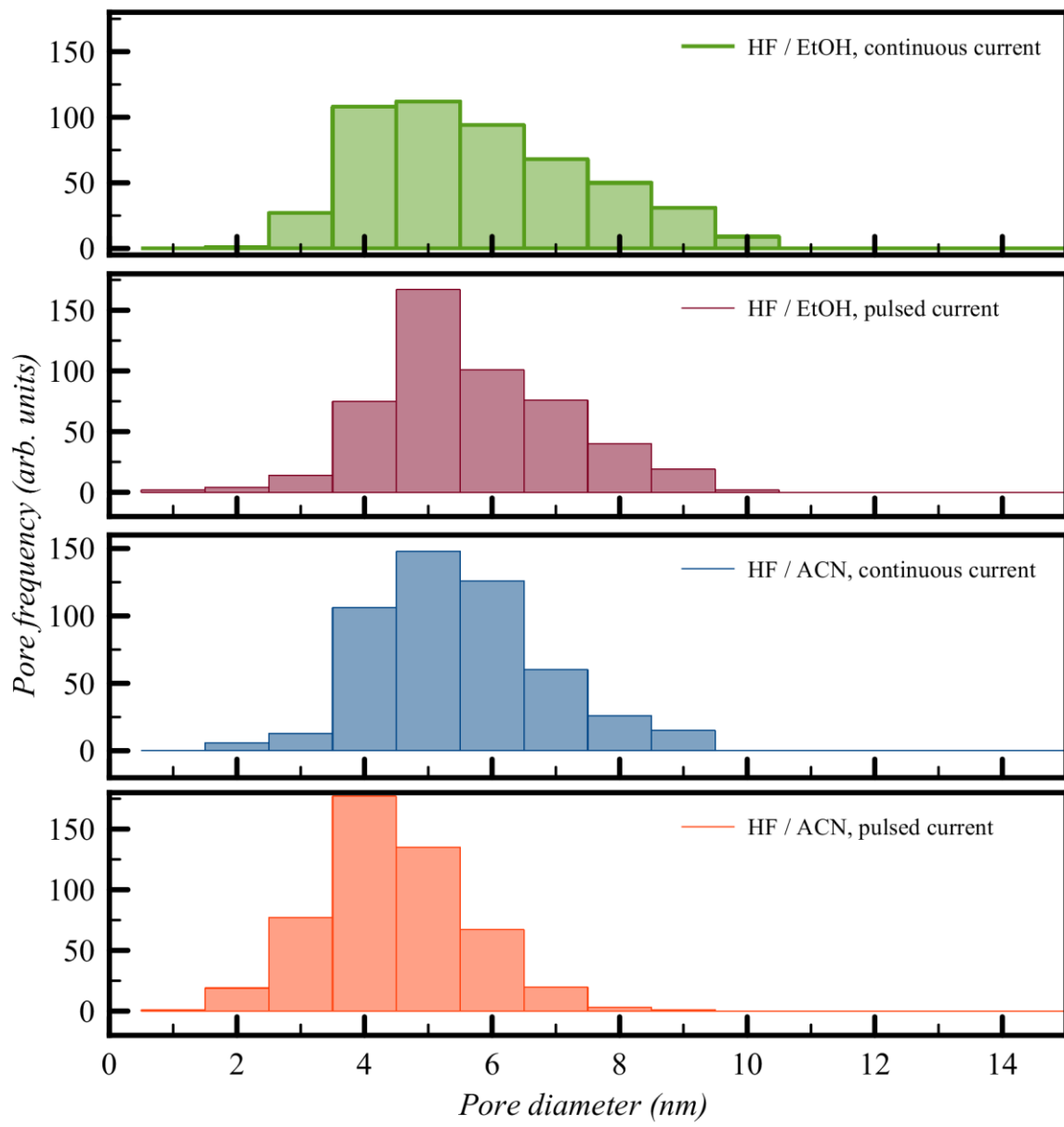


Figure 2-5: Pore size distribution of pSi etched under varying current / electrolyte regimes.

2.2 Loading of oxidising agents into pSi

Stock solutions of the oxidising agent under investigation were prepared by dissolving the solid salt into methanol at a concentration near the saturation point. The solution of the selected oxidising agent was micropipetted onto the etched wafer and impregnated the pSi by capillary forces. The solvent was evaporated in a gentle stream of N₂ gas, depositing the solid agent within the pores.

Conveniently, the actual volume of solution added to the wafer was able to be calculated for each individual sample to completely fill the pores from the following relationship:

$$V_{ox} = (m_1 - m_2) * \frac{\rho_{ox}}{\rho_{Si}} * \frac{1000}{[ox]} \quad \text{Equation 2-2}$$

where V_{ox} is the volume of oxidising agent added to the sample (μL), m_1 and m_2 are the wafer masses before and after etching respectively (mg), ρ_{ox} and ρ_{Si} are the densities of the solid oxidising agent and silicon, respectively, and $[ox]$ is the concentration of the oxidising agent stock solution (mg.mL^{-1}). This relationship enabled samples to be prepared with the pore volume filled as close as possible to their maximum available capacity.

In all cases, samples were stored in a desiccator prior to analysis. The desiccator was not kept under vacuum, but contained silica gel desiccant to remove atmospheric moisture within the container.

2.3 Safety relating to handling of manufactured energetic materials

It was apparent through both the reviewed literature and experience during this work that pSi energetic materials were very sensitive to initiation. For many of the pSi / oxidising agent combinations investigated, the material was so sensitive that any mechanical disruption of the surface would cause initiation, and this led to a strong propensity for accidental ignition during handling.

Two notable incidents occurred during this project. In the first, a set of samples stored in a vacuum desiccator initiated possibly as a result of vibrations from the vacuum pump transmitted through the bench and connecting hoses. In the second, a set of samples initiated within a plastic Petri dish while being handled in a laboratory setting – the cause of this was attributed to either electrostatic discharge or due to two samples rubbing together (causing a friction-driven initiation). In neither of these cases, no person was injured due to use of appropriate personal protective equipment and implementation of various administrative controls.

Partly as a result of these incidents, safety procedures evolved through the life of the project. Persons handling these energetic materials wore low-flammability clothing, and cotton laboratory coats. Standard safety glasses and hearing protection were to be worn at all times. Cut-resistant gloves were also worn to minimise the risk of injury from sharp fragments of material ejected from exploding pSi.

A conductive rubber mat, earthed to a standard electrical wall outlet, and fitted with a conductive wrist-strap, was used on the main laboratory work surface to provide a path for dissipation of static electricity from both the surface and staff. A smaller portable mat was provided for use in other laboratories when required. Samples were stored in individual conductive containers designed for handling static sensitive electrical components, containing an internal soft conductive foam liner. These individual sample containers were packaged in a metal carry box when required for inter-laboratory transport. In no instances were samples of energetic materials transported by road or in another public place outside of the laboratory environment.

Porous silicon energetic materials were prepared only as required, and only in sufficient quantity to complete a discrete series of experiments without the samples being stored overnight. As a general rule, samples would not be stored but would be initiated within one hour of preparation. During temporary storage, individual samples were limited to a maximum net explosive quantity (NEQ) of 100 mg, with a maximum total NEQ of 500 mg.

Wherever possible, plastic tools (e.g. tweezers, spatulas) were used – metal tools were avoided due to the risk of initiation from impact or friction. During planned initiation of pSi energetic materials, experiments were conducted behind or underneath a suitable safety shield, and work times were chosen to avoid the presence of other staff within the same laboratory.

All manufacture of energetic materials was conducted under the auspices of a Permit to Purchase Explosives, issued by the Inspector of Explosives, SafeWork SA, in compliance with the Explosives Act, 1936.

Chapter 3 THE BURNING RATE OF POROUS SILICON ENERGETIC MATERIALS

Measurement of the burning rate of pSi energetic materials is presented. The influence of the sample porosity and pSi layer thickness is examined, as are the different performances of various oxidising agents. Erratic burning rates were further investigated using high speed videography. The basic assumption that the oxidising agent is evenly distributed within the pores is challenged.

These results were published in:

Plummer, A., Kuznetsov, V., Joyner, T., Shapter, J., and Voelcker, N.H., 2011, “The burning rate of energetic films of nanostructures porous silicon,” *Small*, 7 (23), pp3392 – 3398,

and partly in:

Plummer, A., Kuznetsov, V., Gascooke, J., Shapter, J., and Voelcker, N.H, 2016, “Sensitiveness of porous silicon based nano-energetic films,” *Propellants, Explosives, Pyrotechnics*, 41, pp1029-1035.

3.1 Introduction

The explosive performance of pSi energetic materials has been shown to depend on the size and depth of the pores (in turn influenced by the etching variables of HF concentration, wafer properties, etching current and time), the choice of oxidising agent and ratio of Si to oxidising agent (19, 23, 39, 65). Traditionally, the pSi energetic material research to date has presented experimental data based on the luminous intensity of the reaction, measured by photodiodes (19, 23, 39, 65). A significant disadvantage of this approach is that it is difficult to compare the results to other energetic materials, which typically use data such as burning rates or detonation velocities for comparative analysis. There is a conspicuous lack of such data in the published literature concerning pSi energetic materials. Two reports (37, 39) however, presented reaction velocities. Kovalev *et al.*(39) estimated that the reaction front velocity for pSi reacting with liquid oxygen was in the order of $10,000 \text{ m}\cdot\text{s}^{-1}$, based on the rise time of the photodiode, and Clément *et al.* (37) estimated that pSi impregnated with sodium perchlorate reacted at rates exceeding $2,000 \text{ m}\cdot\text{s}^{-1}$ based on the time that the reaction front interrupted a laser reflected from the surface. Subsequent to the work presented in this Thesis, pSi has been investigated using combinations of high speed video analysis and electronic probes to detect passage of the flame front passing along the burning surface. These works have recorded velocities as low as $2\text{-}3 \text{ m}\cdot\text{s}^{-1}$ (76) to over $3000 \text{ m}\cdot\text{s}^{-1}$ (45).

The advantage of the previous photodiode sensitivity work, however, is that it demonstrated the potential for using the bright optical emission of the burning material to measure the sample. Using an array of fibre-optic probes at fixed distances, individually connected to photodiodes, would enable the progression of the reaction front to be measured as a function

of time, a common technique in the field of energetic materials research (25, 89).

Characterising pSi energetic materials in this way will enable different variants to be compared to each other, and to alternative energetic materials, independent of the measurement technique.

It is clear from the above discussion that knowledge of the burning rate of pSi energetic materials is a fundamental gap in the understanding of these systems. Key questions to be addressed in this Chapter are:

- How does sample morphology (i.e. porosity, porous layer thickness) influence the burning rate?
- Do different oxidising agents demonstrate different burning rates?
- Does the oxidising agent penetrate evenly into the porous layer, or is there some bias present creating an uneven distribution within the pores?

3.2 Materials and experimental methods

pSi samples were prepared by the pulsed electrochemical etching method described in Section 2.1, and characterised by the methods described therein. Etching time was controlled from between 5 and 90 minutes of applied current (7.5 and 135 minutes of experimental preparation time at 66% duty cycle), and at HF concentrations of between 10 and 40%.

3.2.1 Sample initiation and burning rate measurement

Loaded samples were initiated using a high voltage electric spark, generated by a Bosch GT40 automotive ignition coil. A remote trigger box was constructed using the aluminium body of the box acting as the ground plane, with a flexible cable connected to an electrode held above the pSi surface. Samples could be initiated either directly on top of the spark box, or in a conductive assembly placed on the box. The energy of the spark was measured to be 100.9 ± 2.4 mJ with a potential of ≈ 10 kV.

When determining the burning rate, samples were retained on a stainless steel block mounted on top of the aluminium trigger box, with the fibre-optic array held close to the surface by a second block bolted to the base plate. This system (Figure 3-1) permitted the top block to be held away from the surface by inserting steel washers as spacers (for unconfined velocity testing) or clamped directly against the surface for confined velocity testing. It must be noted that even in the confined configuration, a microscopic air-gap existed between the surface of the energetic material and the confining stainless steel block as no bonding agent was applied between the two surfaces.

Five fibre optic probes were held along the centre line of the sample at 5 mm gaps, with the first of the probes being 10 mm from the point of initiation. The fibre optic cable was an OMC-US single-core polymer cable (1.0 mm core diameter, 1.0 mm sheath). The end of the fibre optic cable was freshly cleaved using a razor blade between each sample. The probes

were held very close to the pSi surface, but did not actually touch it in order to prevent a measurement artefact due to sample confinement from the actual cable itself.

Each of the fibre optic probes was connected to a HFBR-2521Z fibre optic photodiode receiver. A custom-built circuit interfaced these probes to a Tektronix 2232 digital storage oscilloscope (100 MHz resolution). This circuit provides a -0.5 V step for each probe that activates, permitting the time of activation (i.e. time of arrival of the reaction front) to be measured as a function of distance. The circuit also ensures that if any particular probe fails to activate, then the next probe will activate both voltage steps, ensuring that the time of activation for any particular probe is known due to the measured voltage. The recorded velocity for any individual sample was the average velocity across the longest distance of burning, measured by activation of the earliest and latest fibre optic probes. Measurements were averaged over five individual sample replicates. Timing accuracy of the oscilloscope was verified by technical staff from the Faculty of Science and Engineering workshops.

Qualitative image-based analysis of the reaction front was also performed using a Photron FastCam Ultima-APX high-speed digital video camera. The camera was operated at 12,500 frames per second, and supplemental lighting was provided by high intensity halogen spot-lights. To avoid premature initiation of the sample due to the heat generated by the spot-lights, they were switched on only a few seconds prior to the desired time of initiation of the sample.

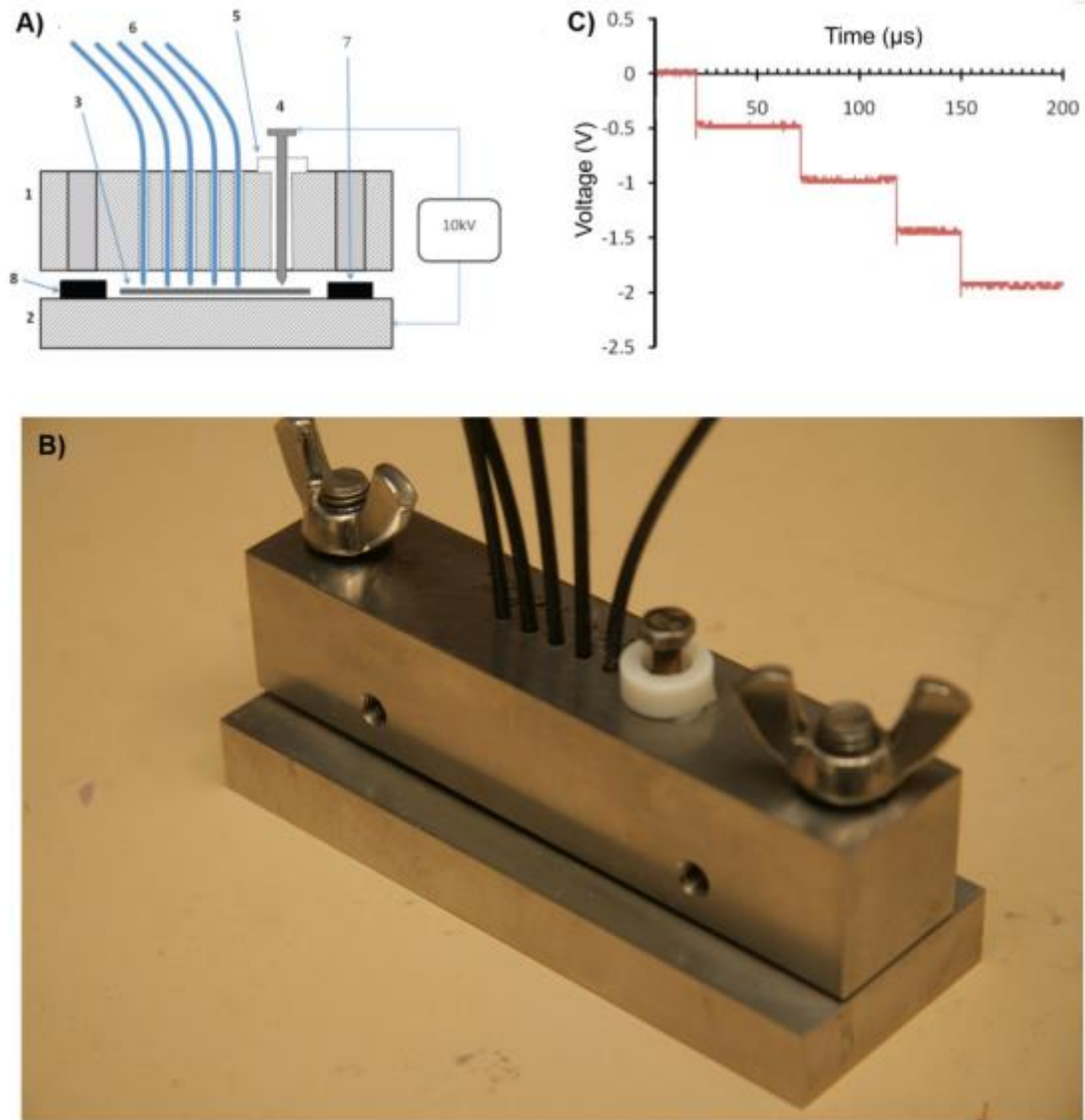


Figure 3-1: A) and B) Fibre-optic array consisting of stainless steel block (1) and base (2), sample (3), adjustable spark electrode (4), Teflon insulator (5) and fibre optic probes (6). The array is clamped together using retaining bolts through the upper block (7) and may be held away from the sample using spacers (8). C) Representative oscilloscope trace from fibre optic array (collected on DSO-2090 USB oscilloscope for presentation, 40 MHz resolution) for pSi etched at 22.5 mA cm^{-2} , 40% HF electrolyte, 180 duty cycles, initiated in confined configuration. The 5th fibre optic probe failed to trigger the voltage drop from -2.0 to -2.5 V – measured velocity is averaged over the preceding four probes.

3.2.2 Oxidising agent distribution

The degree of volumetric loading of the oxidising agent into the pores was determined gravimetrically. The distribution of the oxidising agent deposited into the pores was

investigated by two separate methods. Penetration of the inorganic oxidising agent was investigated using a FEI Inspect F50 SEM coupled with EDAX energy dispersive x-ray analysis (EDX). It was reasonably anticipated that samples of live energetic material would initiate if exposed to the electron beam within the SEM. Therefore, in order to simulate the behaviour of SP being deposited into the pores, calcium chloride (CaCl_2) was chosen as a non-energetic simulant due to its high solubility in methanol (prepared at 246 g.L^{-1}) and the ease with which Ca and Si signals can be resolved by EDX. Samples of pSi were loaded with CaCl_2 , and cross sections were mounted for SEM-EDX analysis.

Similarly, it was reasonably anticipated that the alternative oxidising agent under investigation (PFPE) would also initiate within the SEM. No suitable non-energetic simulant was available having similar properties to the PFPE. Therefore, the distribution of the PFPE was investigated directly using a Horiba Xplora Raman microscope (785 nm illuminating laser, 90 seconds spectra collection time), operated at 1% of maximum laser intensity to reduce the possibility of initiation.

3.3 Results and discussion

3.3.1 Effect of porosity

Porosity is the measure of the volume fraction of voids present in the porous structure. Assuming that the pores can be filled to their maximum capacity with crystallised oxidising agent, the porosity should exert a strong influence on the performance of the energetic material. The bulk performance of energetic materials in general is most efficient at or near to

a balanced stoichiometry (28). By calculation, the ideal porosity to provide for a balanced mixture of SP and pSi on the basis of Reaction 1-1 is 74.4% (84). With all other variables held constant, decreasing the HF concentration of the electrolyte solution will tend to increase the porosity of the pSi.

pSi was prepared at HF concentrations varying between 10 and 40%. Each sample was etched for 180 duty cycles (a total of 30 minutes of applied current) at a current of 85 mA ($22.5 \text{ mA} \cdot \text{cm}^{-2}$) for a total charge of 153 C of applied electrical charge. Samples etched at HF concentrations below 10% were unsuitable for investigation, due to the pSi surface disintegrating within the duration of the etch. Pore size and porosity of the samples was determined using SEM and gravimetry, respectively (see Table 3-1). All samples were loaded with SP as the oxidising agent. In order to investigate the influence of confinement on the reaction velocity, samples were measured both with and without confinement by the stainless steel block of the fibre-optic array. The results of the velocity measurements are also summarised in Table 3-1.

Table 3-1 Reaction velocity (under confined and unconfined conditions) as a function of surface porosity and pore size, etched at varying electrolyte concentrations. Displayed errors are 1 standard deviation (n = 5).

HF concentration (%)	Porosity (%)	Pore size (nm)	Velocity unconfined ($\text{m} \cdot \text{s}^{-1}$)	Velocity confined ($\text{m} \cdot \text{s}^{-1}$)
10	72.2 ± 0.6	6.4 ± 1.7	94 ± 7	209 ± 50
15	69.7 ± 0.6	4.0 ± 1.3	-	334 ± 68
20	64.7 ± 0.5	3.6 ± 1.4	88 ± 11	276 ± 70
25	60.0 ± 0.1	3.6 ± 1.4	-	231 ± 45
30	58.1 ± 2.1	2.9 ± 1.0	70 ± 18	124 ± 7
40	52.3 ± 1.3	2.9 ± 1.4	94 ± 16	103 ± 13

For the unconfined samples, a trend of reaction velocity was not observed, and accordingly no data was collected for 15% and 25% electrolyte solutions. In the confined samples, however, the velocity peaked at over 300 m s^{-1} at a porosity of approximately 70%, but dropped sharply above this point. The low velocities observed at the lowest porosities are not surprising considering that the reacting mixtures are so fuel rich, reducing the overall efficiency of the reaction.

The fact that the velocity peaks at a porosity slightly lower than the predicted ideal indicates that the microstructure influences flame propagation through the material. It could be considered that at low porosity, pores had smaller diameter and were less numerous compared to higher porosity samples, thereby restricting flame propagation through the pore network. If flame progression is aided by progressive disintegration of the pSi matrix at the flame front, the additional rigidity provided by low porosity samples (90) may also contribute to lower burning rates. Considering that the burning rate drops sharply at a porosity of 72%, it may be that the material is so weak that it provides no effective barrier to generation of pressure at the burning front, thereby contributing to a lower local burning rate in accordance with Equation 1-1. These two competing influences appear to reach a balance at the observed peak porosity of 69.7%.

Furthermore, the fact that the burning rates are considerably higher in the confined samples than in the unconfined samples indicates that this reaction is not the simple gasless reaction predicted by Reaction 1.1 but that there is a significant influence from gaseous reaction

products (possibly including the bound hydrogen from the freshly etched surface, or from vapourised NaCl).

It should be noted that while the peak velocity (confined) occurred at a porosity of $\approx 70\%$, samples etched using 15% HF electrolyte beyond 30 minutes of applied current demonstrated a trend of decreasing sample quality. This manifested as pSi surfaces becoming fragile and disintegrating into flakes unsuitable for use. As indicated by the reaction detailed in Figure 1-2, HF is gradually depleted from the electrolyte as pSi grows. Depletion of HF from the electrolyte (and therefore reducing concentration) will drive samples toward higher and higher porosities as etching time increases. While one possible solution for this would be to increase the electrolyte volume to maintain a relatively consistent HF concentration for long duration etches, it was decided to conduct all future studies at a porosity of 65% (using 20% HF electrolyte). This provided the best compromise of near maximum performance and stability of the pSi, within the safety limitations of the available equipment.

3.3.2 Effect of film thickness

Lazaruk *et al.* (23) demonstrated a linear relationship between the thickness of the pSi layer (loaded with potassium nitrate) and the optical intensity of the resulting explosion.

Lazarouk *et al.* (41) suggested that the minimum thickness for a sustainable energetic reaction between pSi and potassium nitrate was $15\mu\text{m}$. However, no data was presented in this or other literature that suggested an upper limit beyond which no velocity advantage is observed. To investigate the effect of pore depth on the burning rate, samples were prepared at a HF

concentration of 20% and a current of 85 mA ($22.5 \text{ mA}\cdot\text{cm}^{-2}$). Samples were etched for varying numbers of cycles to produce applied current times up to 90 minutes, and all samples were loaded with SP to create the energetic material. The burning rates recorded for samples initiated under confined and unconfined conditions are displayed in Table 3-2. Samples that were etched for longer than 180 cycles (30 minutes applied current) were interrupted and the etching solution refreshed to avoid depletion of the HF.

Table 3-2: Reaction velocity (under confined and unconfined conditions) as a function of pore depth for pSi etched at $22.5 \text{ mA}\cdot\text{cm}^{-2}$ in 20% HF electrolyte solutions, loaded with SP. Displayed errors are 1 standard deviation (n = 5).

Cycles	Applied etching time (minutes)	Applied charge (Coulombs)	Pore depth (μm)	Velocity unconfined (m s^{-1})	Velocity confined (m s^{-1})
30	5	25.5	4.2 ± 0.2	1.2 ± 0.3	2.4 ± 0.8
60	10	51.0	8.8 ± 0.1	3.4 ± 1.4	3.8 ± 0.7
90	15	76.5	14.4 ± 0.4	17 ± 8	19 ± 6
180	30	153.0	26.2 ± 0.2	88 ± 11	276 ± 70
270	45	229.5	42.9 ± 0.4	101 ± 17	324 ± 45
360	60	306.0	53.7 ± 0.6	134 ± 42	425 ± 96
540	90	459.0	72.0 ± 0.6	199 ± 53	399 ± 124

It can be seen from Table 3-2 and Figure 3-2 that the burning rate increased significantly at lower pore depths, but the velocity of the burning front remained relatively slow. However, between depths of 14 and 26 μm , the burning rate jumped significantly. Beyond this inflection point large increases in the pSi layer depth were not accompanied by significantly large increases in the burning rate, evident as a plateau in Figure 3-2. It is possible that at this point the structure of the material became self-confining in a way that increased the burning rate significantly.

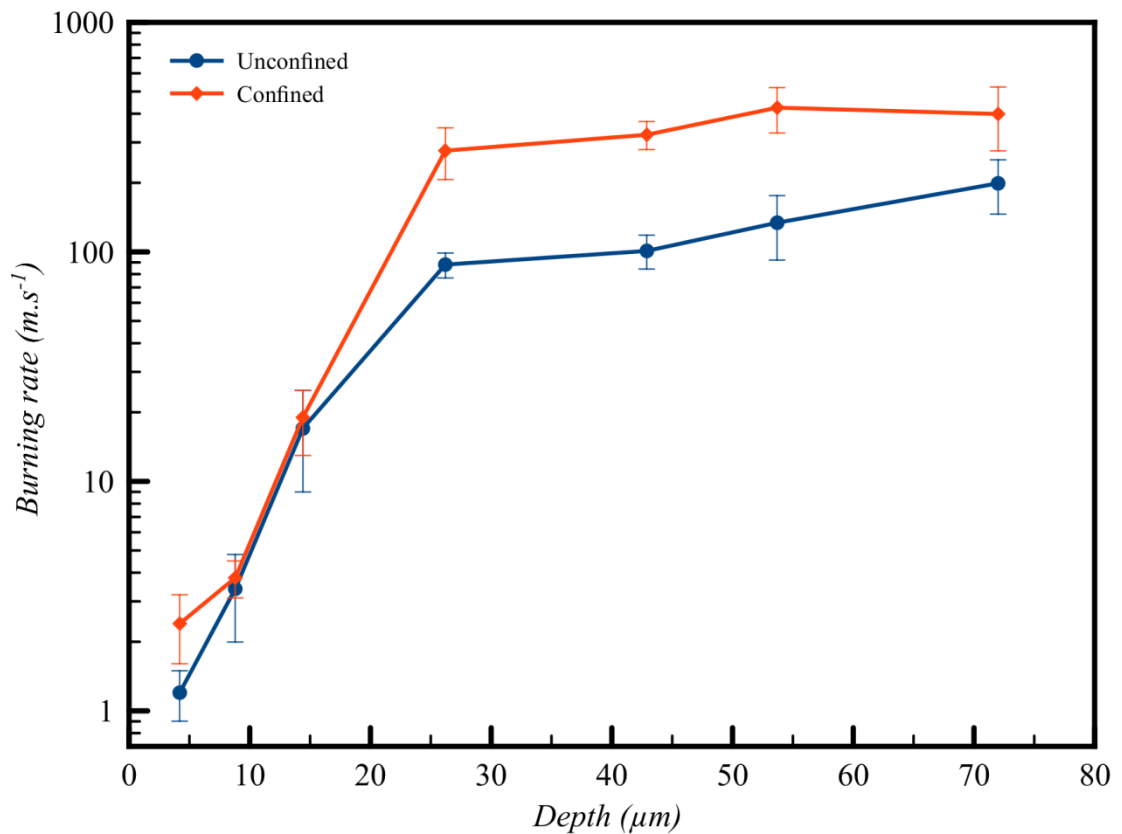


Figure 3-2: Reaction velocity (under confined and unconfined conditions) as a function of pore depth for pSi etched at 22.5 mA.cm^{-2} in 20% HF electrolyte solutions, loaded with SP (n=5).

Our results are somewhat in accordance with the work of Lazaruk *et al.* (23) who observed that the optical intensity of combustion increased linearly with increasing etch depth, however their analysis demonstrated that the intensity would rise continuously without limit instead of the plateau reported here. This is an important observation because it demonstrates that burning rate is independent from optical emission intensity. Again, as expected, the velocity of the confined samples exceeded that of the unconfined samples. The observed plateau suggests that acceleration of hot reaction products (either through the material or along the thin gap between the sample and the confining block) reached some limiting value beyond which it was no longer possible to increase the velocity of the reaction.

All samples previously described consisted of a pSi layer bound to the supporting wafer. It was considered that if the energetic material was not constrained by being bound to the base layer, the velocity of the burning front would increase. A further set of samples were prepared (180 cycles, 22.5 mA cm^{-2} , 20% HF) but were subjected to an electropolishing step at the end of the main etch, undercutting the pores to form free-standing pSi membranes of $\approx 26 \mu\text{m}$ thickness. Three samples prepared in this manner were loaded with SP and initiated in a confined configuration, yielding an average reaction velocity of $383 \pm 11 \text{ m s}^{-1}$. This is a significantly faster reaction velocity when compared to samples prepared under the same etch conditions, but remaining bound to the supporting wafer ($276 \pm 70 \text{ m s}^{-1}$). It is likely that the very thin gap between the base of the pSi membrane and the contact plate acted as a path along which hot reaction products could travel. In combination with a similarly thin gap between the top surface and the top block of the fibre optic array, these two paths combined to increase the surface area available for combustion, thereby accelerating the reaction velocity compared to the bound layer. During this series of experiments, it was observed that a free-standing membrane of pSi loaded with SP was exceedingly sensitive, and several samples were initiated prematurely by very light mechanical pressure during handling (e.g. the pressure of placing the fibre-optic probe against the surface), possibly causing the brittle pSi surface to fracture and commence the burning reaction. Accordingly, no further work was carried out with pSi in this configuration.

3.3.3 Effect of various oxidising agents

SP has dominated research into pSi energetic materials (see Table 1-1). Clément *et al.* (37) trialled a wide variety of different oxidising agents, however reported only the presence or absence of an observed explosion, rather than quantifying their burning rates.

Here, a variety of substances were investigated to understand their potential as oxidising agents suitable for pSi energetic materials systems. With one exception, the primary reason for investigating a substance was its solubility in the carrier solvent, methanol. Solutions were prepared at concentrations approaching the saturation limit for the individual oxidising agent, with an upper limit of approximately 400 g.L^{-1} . These parameters were chosen to provide a balance between the volume of solution to be added to a surface as determined by Equation 2-2, and the need to cover the entire pSi surface with solution (thereby encouraging even distribution across the measurement area). Solution concentrations are listed in Table 3-3.

The exception to the use of methanol as the carrier solvent occurred for perfluoropolyether Fomblin Y HVAC 25/9 (PFPE) oxidising agent. This was prepared as a solution (200 g.L^{-1}) in the fully fluorinated volatile solvent FC-75. Fomblin Y is a high viscosity liquid at room temperature. Impregnation of this material into the pores required the stock solution to be pipetted onto the surface, followed by evaporation under vacuum in a desiccator with subsequent back-filling of the vessel using N_2 – three successive steps were required in order to load the wafer.

Each pSi sample was etched for 90 duty cycles (a total of 15 minutes of applied current), at a current of 170 mA (45 mA cm^{-2} , 153 C), in a 20% HF electrolyte, producing a pSi surface with a porosity of $64.7 \pm 0.5\%$, a depth of $26.2 \pm 0.2 \mu\text{m}$, and pore diameters of $3.6 \pm 1.4 \text{ nm}$.

All substances were initially checked for compatibility with pSi by performing a spot check of a single droplet of the solution onto a freshly etched pSi surface. Two substances ($\text{Cu}(\text{NO}_3)_2$ and KMnO_4) reacted immediately on contact with the surface, causing the pSi to degrade non-explosively within a few minutes possibly due to an adverse electrochemical reaction between the substances present. No other oxidising agents displayed an incompatibility with pSi.

All samples were initiated in both confined and unconfined configurations, initiated with a high voltage electric spark. Burning rates recorded by the fibre optic velocity probes are presented in Table 3-3.

As can be seen from these results, most oxidising agents investigated demonstrated a capability of functioning as a suitable agent in pSi energetic material systems. Most of the chlorate, perchlorate and nitrates investigated displayed low to moderate burning rates when initiated without confinement. SP clearly demonstrated the fastest burning rates under these conditions in either confined or unconfined configurations, recording the maximum burning rate of 276 m.s^{-1} . Both magnesium perchlorate and gadolinium nitrate also demonstrated moderately high burning rates when initiated under confinement.

Table 3-3: Burning rate of pSi loaded with various oxidising agents.

Oxidising agent	Concentration (g.L ⁻¹)	Velocity (m.s ⁻¹) (n=5)	
		Unconfined	Confined
Ba(ClO ₄) ₂	408	2.39 ± 0.42	93.7 ± 24.0
LiClO ₄	199	1.66 ± 0.25	43.0 ± 13.5
Mg(ClO ₄) ₂	300	19.0 ± 11.3	136.8 ± 62.6
Na(ClO ₄) ₂	400	87.5 ± 10.6	276.9 ± 69.9
Sr(ClO ₃) ₂	76	4.27 ± 0.50	38.3 ± 14.9
Al(NO ₃) ₃	318	3.17 ± 0.66	12.5 ± 2.5
Gd(NO ₃) ₃	346	2.84 ± 0.36	133.1 ± 37.5
Ni(NO ₃) ₂	400	0.88 ± 0.31	-
Perfluorononanoic acid	400	0.20 ± 0.05	0.21 ± 0.03
Perfluoropolyether	200	0.24 ± 0.01	0.23 ± 0.01

These velocities are in the same order of magnitude as those reported by Currano and Churaman (53) (600 m.s⁻¹) and Piekel *et al.* (22) (200 – 800 m.s⁻¹) at similar porosities, but far lower than those reported by Becker *et al.* (45) (>3000 m.s⁻¹). The possible causes for these differences are discussed in Section 3.3.4. Similarly, Abraham *et al.* (43) reported unconfined burning rates in the order of 2.9 to 21 m.s⁻¹ for a variety of nitrate salts and sulphur.

Notably, nickel nitrate was incredibly inefficient under these circumstances. While a burning rate of 0.88 m.s⁻¹ was able to be recorded when initiated in an unconfined configuration, this was achieved only after attempting 15 samples. Flame progress was noticed to be quite insipid with many samples self-extinguishing before valid velocity measurements were able to be recorded. No burning rates were able to be successfully recorded in a confined configuration.

Two perfluorinated substances were also investigated as alternatives to the inorganic substances previously described. Both perfluorononanoic acid (PFNA) and perfluoropolyether (PFPE) demonstrated very low burning rates of $\approx 0.2 \text{ m.s}^{-1}$. Confinement appeared to have no significant effect on the burning rate, and both substances displayed very consistent flame speeds. While the burning rates for these oxidising agents are considerable lower than their inorganic counterparts, these materials are interesting due to their consistency. Furthermore, neither PFNA or PFPE are classified as dangerous goods, a fact that may present advantages for handling and preparation.

The velocity of pSi loaded with PFPE is clearly much lower than when loaded with SP. However, it is somewhat higher than the 0.014 m.s^{-1} reported by Mason (91). In that work, only very small samples of pSi loaded with PFPE ($3 \times 5 \text{ mm}^2$) were ignited, and the pSi had a significantly higher porosity (80 to 90%) compared to the 66% porosity of our material. It was demonstrated in Sections 3.3.1 and 3.3.2 that for perchlorate-based systems, the structure of the pSi substrate has a significant influence on the burning rate (22) and there is every expectation that similar influences would be observed for fluorocarbon-loaded pSi.

Mason (91) further observed that the samples loaded with PFPE failed to ignite using a nichrome hot-wire, or from the heat liberated from a nanothermite formulation, but would ignite upon application of a naked flame for 10 to 20 seconds. Here, ignition was not attempted using such heat sources, and it was found that samples ignited promptly with a high voltage electric spark. It is known that one path in the reaction between a fluorocarbon and a metallic fuel commences by rupturing of the perfluoropolymer molecule to liberate a variety

of highly reactive radicals (92, 93), with the molecules pyrolysing at greater than 290 °C (94). So, while PFPE has a high viscosity and low vapour pressure at room temperature, application of a point-heat source may not cause sufficiently fast temperature rise to initiate the reaction if the PFPE is being driven away from the heating point (due to the combined effects of reduced viscosity and increased vapour pressure at elevated temperatures), thereby reducing the oxidising agent concentration in the immediate vicinity of the heat source. However, the prompt ignition of the sample upon application of the high voltage spark suggests that the sample is either being heated very rapidly (faster than the PFPE can diffuse away from the point heat source), or, alternatively that the PFPE molecule is being ionised directly by the spark (93).

3.3.4 High speed video analysis

During these burning rate experiments, large sample-to-sample variance in was observed, in many cases exceeding 25% and in few cases approaching 50% (Table 3-1 and Table 3-2). In order to investigate the source of this variance, the reaction triggered by a spark was recorded with a FastCam high speed video camera. In these experiments, samples were initiated directly on the spark trigger box.

Samples prepared at a HF concentration of 20% and a current of 170 mA ($45 \text{ mA} \cdot \text{cm}^{-2}$) were etched for 90 and 180 duty cycles to produce different pore depths of 24.9 and 49.9 μm , respectively. At this etching current, the pore diameter is $3.5 \pm 1.7 \text{ nm}$, very similar to pores produced at the lower current of $22.5 \text{ mA} \cdot \text{cm}^{-2}$ and the same HF concentration (see Table 3-1).

The first observation from these experiments was that all of the samples initiated under unconfined conditions appeared to deflagrate, and no evidence of detonation was observed. Detonation could be inferred if the flame proceeded at high velocity (i.e. $>1000 \text{ m.s}^{-1}$), or if a pressure wave was generated which destroyed the supporting brittle Si wafer – such features were not observed. In all of these samples, a strong plume of flame was seen to be jetting off from the surface, and samples which were not taped to the spark trigger box were rapidly propelled off from the surface. For samples with porous layers of less than $25 \mu\text{m}$ thickness, the reaction front was observed to expand radially from the point of initiation until it reached the edge of the etched region. At this point, the burning rate at the edge of the etched region increased and accelerated past the reaction front in the centre of the sample, such that the steady state reaction front had the appearance of an inverted-V (Figure 3-3). This behaviour was observed repeatedly across samples of pSi loaded with different oxidising agents.

When thicker samples were used, such as the $\approx 50 \mu\text{m}$ thick sample shown in Figure 3-4b, the reaction front proceeded in an almost straight line across the width of the sample. This indicates that at some thickness between 25 and $50 \mu\text{m}$, the pSi layer becomes self-confining to such an extent that it increases the pressure of the reaction products within the sample, accelerating the reaction velocity along the centre of the sample to match the velocity along the bordered edge.

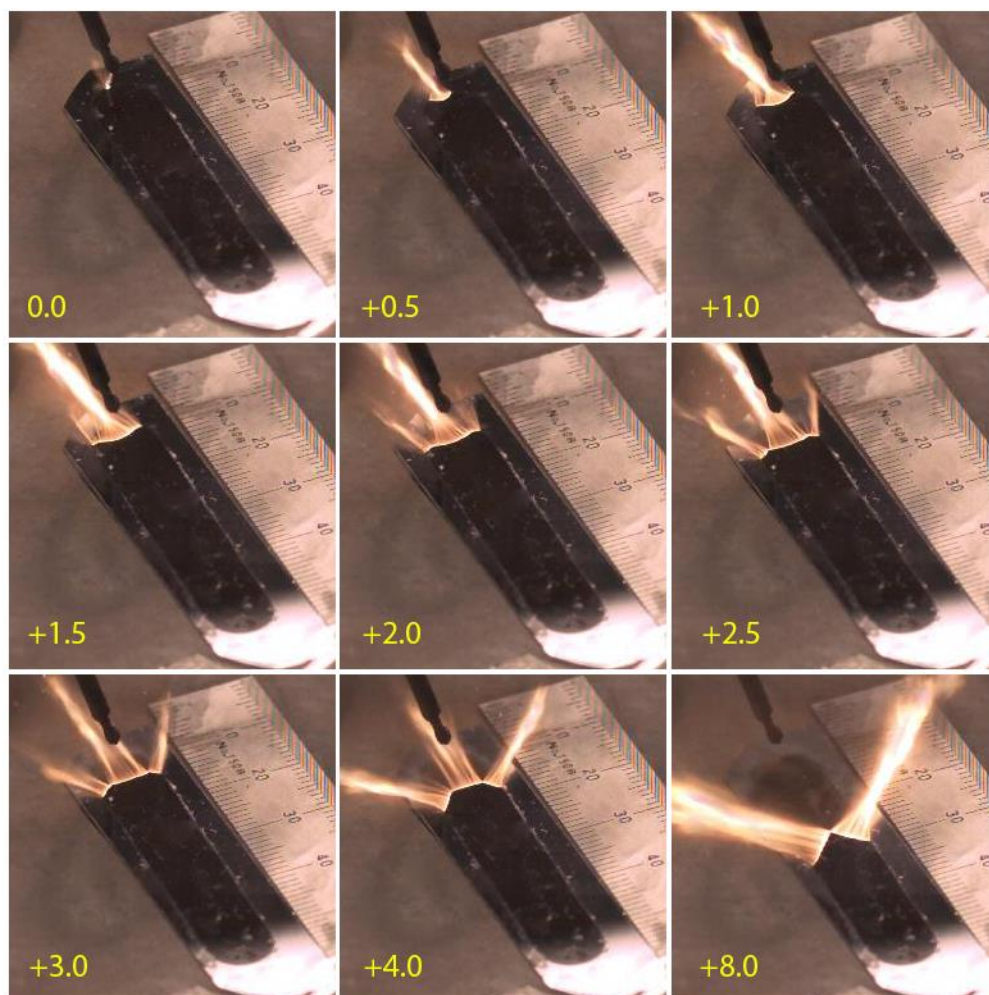


Figure 3-3: Flame development in pSi loaded with $\text{Ba}(\text{ClO}_4)_2$, displaying progression from initial ignition by the spark, radial burning, and development of the inverted-V pattern. Panel increments are in milliseconds, as indicated. Flame speed between images at 4.0 and 8.0 ms is approximately $3.0 \text{ m}\cdot\text{s}^{-1}$.

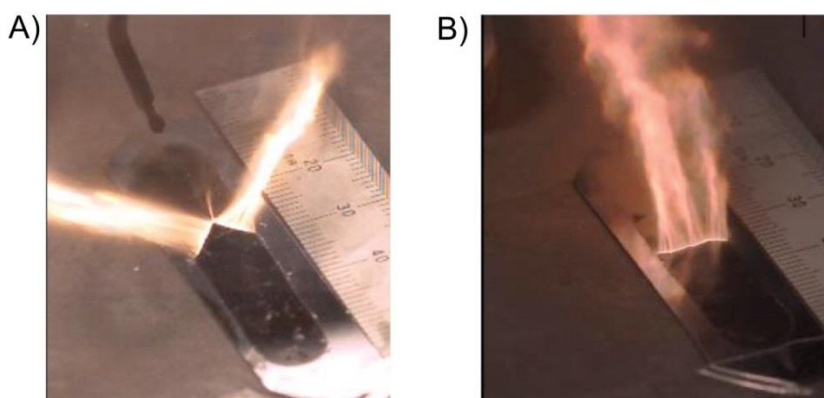


Figure 3-4: A) pSi sample of $24.9 \mu\text{m}$ thickness (etched at $45 \text{ mA}\cdot\text{cm}^{-2}$, 90 duty cycles in 20% HF electrolyte), displaying inverted V steady state reaction front. Flame is proceeding toward the camera from the spark electrode at the top of the sample. B) pSi sample of $49.9 \mu\text{m}$ thickness (etched at $45 \text{ mA}\cdot\text{cm}^{-2}$, 180 duty cycles in 20% HF electrolyte), displaying straight steady state reaction front, advancing toward the camera.

The effect of edge boundary confinement contributing to formation of the inverted-V pattern was evident when a similarly etched sample was split along its long axis. Here, one side of the pSi bordered with un-etched silicon (a confinement in the plane of the pSi layer) but the other side was unconfined. The reaction front had a diagonal appearance (one half of the inverted-V), with the flame along the Si / pSi boundary preceding the flame at the unconfined edge (Figure 3-5).

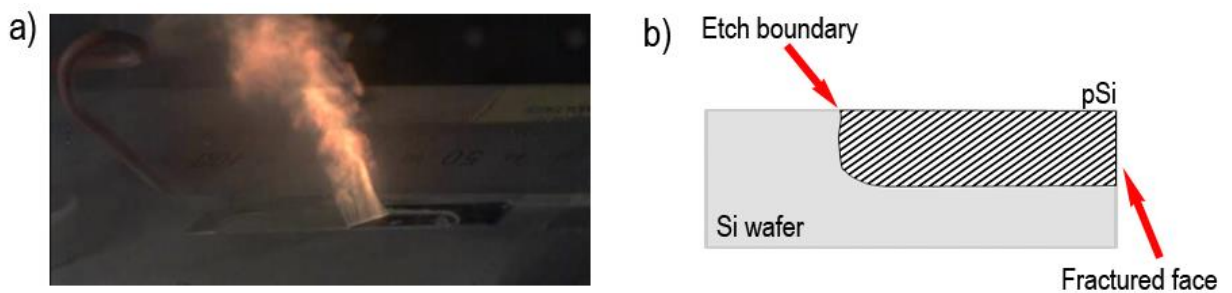


Figure 3-5: a) pSi sample of 24.9 μm thickness (etched at $45 \text{ mA}\cdot\text{cm}^{-2}$, 90 duty cycles in 20% HF electrolyte), loaded with SP, and b) diagram of sample cross section. The sample cracked along the longitudinal axis, leaving a free face of pSi unsupported by the surrounding wafer, and displays only half of the inverted V steady state reaction front.

In many of the samples investigated with the high speed video, there was evidence that the reaction front skipped ahead erratically. The reaction was observed to break through up to 5 mm ahead of the main reaction front. These events manifested as strong jets of flame emanating vertically out of the surface (red marker arrow, Figure 3-6). These spots would then burn radially and coalesce before again forming the steady reaction front observed before their appearance. This skipping was highly erratic and unpredictable. In terms of the fibre optic measurements, this skipping would lead to the apparent average burning rate for any individual sample to be higher than its true steady state value. It is likely that this erratic skipping of the reaction front is a significant contributing factor to the large variance seen in

the quantitative velocity measurements. Similar fast reactive combustion waves have been observed in fissures formed in mechanically and thermally damaged high explosives (25).



Figure 3-6: 49.9 μm thick pSi sample, depicting flame break-through ahead of main reaction front.

The reason for this erratic burning behaviour is unknown. It is possible that, due to the brittle nature of pSi, small plates of the etched layer become detached from the underlying wafer, perhaps due to the combination of microstructural defects in the original pSi surface and the pressure generated within the surface from gaseous reaction products. This would provide for a fissure along which the high pressure flame can jet under before finding another weakness and breaking out to the free surface. The low variance of reaction velocity observed for the 26 μm thick free-standing pSi membrane (2.8%) compared to the attached sample (25.2%) (Section 3.3.2) possibly supports the theory that unpredictable membrane detachment contributes to erratic skipping of the reaction front.

3.3.5 Distribution of oxidising agents within pSi

3.3.5.1 Solid oxidising agents

Preparation of pSi energetic materials involves transport of the oxidising agent into the pores by a low viscosity / high volatility carrier solvent. Capillary forces draw the solution into the pores, whereby the solvent will then evaporate leaving the oxidising agent deposited within the pSi matrix. This issue has been explored only very briefly in pSi energetic material systems. Various carrier solvents (methanol, ethanol, and acetone) were used by Clément *et al.* (37) to transport a wide variety of substances into the pores using successive impregnation / evaporation cycles. However, the actual distribution within the pores was not studied. Piekiet *et al.* (22) used sodium chloride as a simulant in lieu of SP, finding that the material was unevenly distributed toward the base of the pores, but unfortunately did not seek to explain the cause of this distribution.

It has also been previously observed that the loading of SP (as a solution in methanol) into a pSi layer is problematic (61, 76). A common problem is that as the methanol evaporates and the solution becomes saturated, the SP will tend to nucleate on the exterior face of the pSi and then quickly form crystals outside of the pores instead of seeping into the pores as intended, requiring the sample to be washed and re-loaded. Careful evaporation using a stream of nitrogen can assist in preventing this, but even with very careful preparation small crystals may still form on the surface of the wafer, creating uncertainty regarding the exact distribution of the oxidising agent.

To investigate this, a sample of pSi was etched (45 mA/cm², 30 minutes applied current @ 66% duty cycle, 40 μm etch depth) and loaded with 120 μL of CaCl₂ solution (246 g.L⁻¹ in methanol) as a non-energetic material to simulate the behaviour of SP. After evaporation in a stream of nitrogen and conditioning for 20 minutes in a vacuum desiccator, the samples were cleaved and a cross-section mounted for SEM imaging and EDX analysis. The added quantity of CaCl₂ was calculated to be approximately 41% of the maximum loading of the available pore volume – this was deliberately chosen to be a sub-optimal loading level to assist visualisation of the CaCl₂ distribution within the pores. Figure 3-7 displays a cross section of the resulting sample, with EDX spectra collected at defined intervals across the depth of the pSi layer.

The CaCl₂ was found to be distributed toward the base of the pores, visualised as a distinct contrast band starting at a depth of approximately 20 μm. This is supported by the atomic concentrations presented in Figure 3-7 (Panel b) which show that the CaCl₂ increased in concentration through the depth of the sample, reaching a maximum at the base of the pSi layer (41.0 μm). The final sample point (at a depth of 44.6 μm from the surface) is in the unetched wafer (region iii). Small crystals of CaCl₂ were clearly visible across the surface of the cross-section of pSi, while the presence of large crystals of CaCl₂ (indicated by the marker arrow in Panel a) on the exposed face of the cross-section are believed to be caused by migration and evaporation of residual water at the freshly cleaved surface under the high vacuum of the SEM chamber.

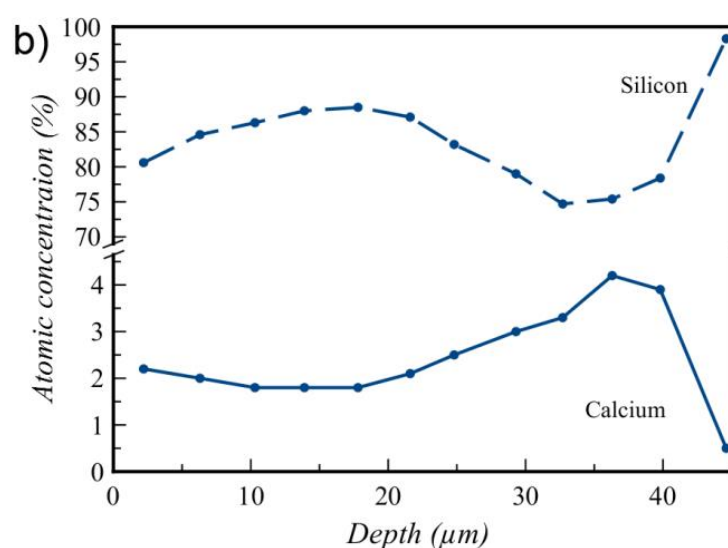
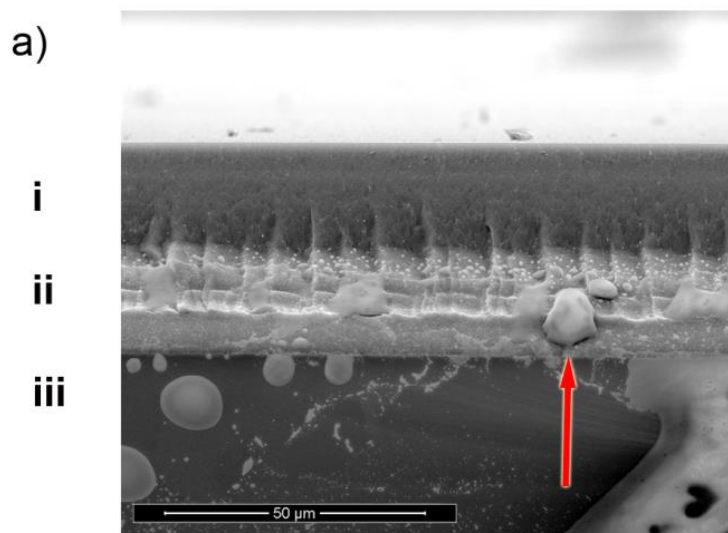


Figure 3-7: a) Cross-section SEM image of pSi (regions i and ii) loaded with CaCl_2 (region ii) supported by the unetched Si wafer (region iii), and b) atomic concentrations of Si and Ca through the depth of the sample into the unetched wafer (the depth reference of $0 \mu\text{m}$ is the top of the pSi layer).

It is clear that, at least for the CaCl_2 simulant, the crystalline material deposited into pSi as a solution in methanol is preferentially loaded towards the base of the pores. One possible explanation for this phenomenon is that contraction of the solvent deeper into the pores, caused by a combination of capillary forces, reducing liquid volume through evaporation, and vapour pressure within the pores above the liquid layer, carries the solution to the base of the

porous layer until it reaches saturation and subsequently precipitates. It is reasonable to infer from this that the SP would behave in a similar manner, and that the biased loading effects would be minimised by loading the pores to their maximum volumetric capacity. These results support very similar observations by Piekiet *et al.* (22).

3.3.5.2 PFPE

Whilst SP is a crystalline solid after the solvent has evaporated, PFPE is a high viscosity liquid polymer at room temperature (viscosity 285 cSt, MW \approx 3800 g/mol, density 1.9 g/cm³). A single loading application of the PFPE solution only partially seeped into the pores, and once the solvent has evaporated an oily film was left on the exterior surface of the pores. Loading was improved by successive loading steps which included evaporating the solvent under vacuum in a desiccator and then returning the desiccator to atmospheric pressure (backfilling the desiccator with N₂) to help drive the PFPE deeper into the pores – it was observed that after three successive load-vacuum-backfill cycles no further loading of the pores was achieved (as determined gravimetrically for each successive cycle).

A sample of pSi was etched (45 mA.cm⁻², 15 minutes applied current @ 66% duty cycle, 12 μ m etch depth) and loaded with PFPE in this manner, and a cross-section of this sample was investigated using Raman microscopy, collecting spectra at 0.5 μ m steps across the layer. Detailed spectra of the sample collected at various depths through the pSi layer are presented in Figure 3-8. By comparison to separate reference samples of pSi and PFPE, a broad spectral band at centred at 625 cm⁻¹ was found to be unique to pSi (due to a combination of various phonon modes in pSi (95)), whilst smaller bands centred at 744 and 810 cm⁻¹ were unique to

the PFPE possibly due to multiple C-O and C-F vibrations (96). The intensity of the pSi and PFPE bands as a function of the depth are presented in Figure 3-9, along with the relative ratio of these two bands. The overall signal intensity of those bands increased towards the top of the porous layer. However, the ratio of the PFPE:pSi bands showed a slight decrease going down into the porous layer. A slight increase at the base of the porous layer (indicated by the rising inflexion of the PFPE:pSi ratio) may be due the marginal signal intensity at those points masking the true relative concentration of the two species, a factor that could be attributed to the low laser intensity used here for safety reasons. Overall this indicates that even though PFPE was being preferentially deposited towards the top of the porous layer, the oxidising agent was still present throughout the pSi. Clearly PFPE is suitable as an oxidising agent, but loading into the surface is limited by the narrow 3.5 nm diameter pores investigated here.

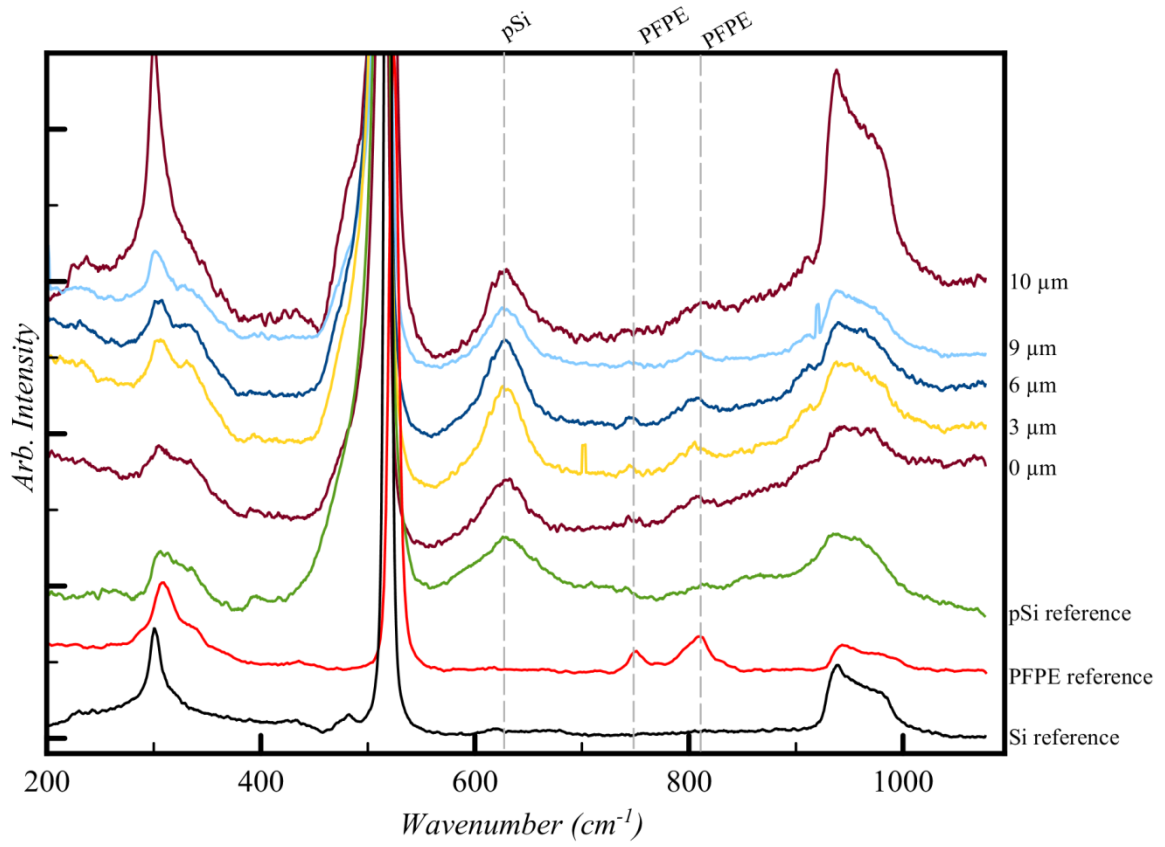


Figure 3-8: Selected Raman spectra across the pSi surface loaded with PFPE including blank pSi and PFPE samples for comparison (the depth reference of 0 μm is the top of the pSi layer). Peaks unique for pSi (625 cm⁻¹), and PFPE (744 and 810 cm⁻¹) are highlighted.

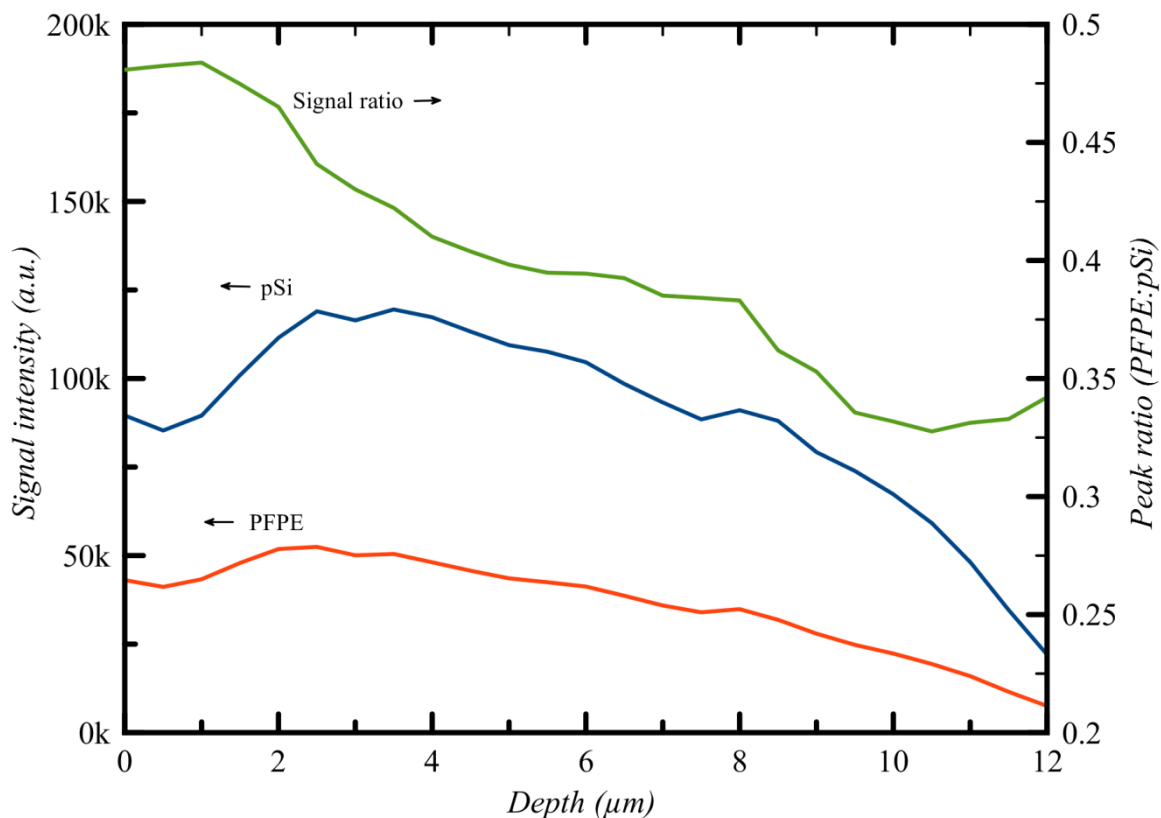


Figure 3-9: Penetration of PFPE into pSi layer. Signal intensity corresponds to the pSi band at $597\text{-}693\text{ cm}^{-1}$ and the PFPE band at $792\text{-}817\text{ cm}^{-1}$ (the depth reference of $0\text{ }\mu\text{m}$ is the top of the pSi layer).

3.4 Conclusions

The principle investigation reported in this Chapter was the determination of the burning rate of pSi under a variety of conditions. Whereas a variety of chlorate, nitrate and perchlorate oxidising agents were investigated, all demonstrating potential for suitable use in this system, sodium perchlorate emerged with the fastest burning rate.

The burning rate was highly dependent on the morphology of the sample – for thin layers the burning rate was strongly dependent on the layer thickness, up to the point where the layer

thickness became self-confining (approximately $25\mu\text{m}$) at which point the confined burning rate plateaued in the order of $200 - 400 \text{ m.s}^{-1}$. This was supported by the use of high speed videography which gave insights to the structure of the burning front – confinement at the edges of the etched area (bound by the supporting Si wafer) accelerated the flame in this region compared to the centre of the sample, giving the burning front a distinct inverted-V pattern. This effect disappeared in thicker samples, supporting the notion that the samples became self-confining at thicknesses greater than $\approx 25 \mu\text{m}$.

There was less dependence of the burning rate on the porosity of the sample. Initiated without confinement, samples of pSi showed marginal differences across a wide range of porosities. However when the effect of sample confinement was added, burning rate peaked at a porosity of approximately 70%.

High speed videography also proved instrumental in discovering the source of erratic burning rate measurements. Unpredictable flame break-outs appearing some distance ahead of the main burning front were visualised. The effect of these break-outs would be to artificially accelerate the burning front, skipping it forward faster than had burning occurred at a steady rate. One possible cause for this skipping was believed to be fissures within the sample, created either due to internal pressure from the burning front, or due to manufacturing defects of the sample itself.

Further investigations revealed that the loading of the sample with oxidising agent was not a simple process, and the assumption that the agent is evenly distributed through the pSi layer is unlikely to be valid. A combination of SEM and EDX investigations indicated that solid inorganic oxidising agents (simulated with CaCl_2) would preferentially deposit at the base of the porous layer. Conversely, high viscosity fluoropolymers investigated using Raman microscopy were found to be preferentially deposited toward the top of the porous layer.

3.5 This Chapter in context with subsequent research

The work presented in this Chapter, specifically Sections 3.3.1, 3.3.2 and 3.3.4, was carried out between 2008 and 2011, and was published in Reference (97). At that time, little research had been published which examined the burning rates of pSi energetic materials, and their relationship to pore structure. Subsequently, several groups have continued investigations into these factors, advancing understanding of pSi energetic materials beyond that presented in this Chapter. Reference (97) has been cited by original research articles (22, 43, 55–59, 61, 62, 71, 72, 98–111) and review articles (84, 112–116).

Whereas the work presented here was limited to determining the influence of porosity and pore depth on the burning rate, Piekielec *et al.* (22) extended this and conducted a further extensive characterisation of the influence porosity, SSA and dopant concentration, finding that peak burning rates ($2000 \text{ m}\cdot\text{s}^{-1}$) occurred at high porosity ($\approx 72\%$) and high SSA ($\approx 900 \text{ m}^2\cdot\text{g}^{-1}$) using moderately doped wafers ($1\text{--}10 \text{ }\Omega\cdot\text{cm}$). This is perhaps the most extensive investigation of the influence that the etching conditions have on the performance of pSi

energetic materials published subsequent to (97). Parimi *et al.* (59) and Yarrington *et al.* (80) separately investigated the influence that substrate doping had on the burning rate, both finding that the dopant type and concentration were significant factors controlling the morphology of the pSi surface, and therefore indirectly influenced the reaction between pSi and the oxidising agent in both perchlorate and fluorocarbon systems.

Here it was observed through high speed videography that flame progression through the pSi was sometimes erratic and would skip ahead leading to artificially high burning rates, and it was proposed that this was due to internal pressurisation of the sample leading to small fissures through which the flame would jet. It was further concluded that the explosive process was a deflagration rather than a detonation. Parimi *et al.* (58) noted a similar effect, and conducted experiments to prevent crack formation during the pSi manufacture process. They reached the similar conclusion that crack formation led to channels through which the flame would progress rapidly. To help confirm this hypothesis, they deliberately introduced channels into the pSi surface and observed acceleration of the flame speed of up to two orders of magnitude. In agreement with the conclusions in (97), Parimi *et al.* (58) concluded that independence of the burning process from external shockwaves above the surface indicated that the process here was a deflagration dominated by conduction and convection heat transfer processes. Conversely, Piekiet *et al.* (62) employed DRIE to form channels within a Si wafer prior to etching to form pSi, noting acceleration of the flame speed of up to $1200 \text{ m}\cdot\text{s}^{-1}$, concluding that the process was driven by an acoustic wave travelling through the medium (described as a pre-detonation) instead of a mere deflagration.

Nevertheless, the concept of controlling the energetic process through organised patterns of etching culminated by Piekiet *et al.* (106) through formation of narrow channels (28 μm wide, 14 μm deep), in a convoluted path concentrated into a small area of only 1 cm^2 (Figure 3-10). Sustained linear burning along this path for a relatively extended period of time may prove beneficial for MEMS applications. Keshavarzi *et al.* (100) took an alternative approach, patterning 3 x 3 mm^2 areas of pSi on a wafer (loaded with SP). They determined that there was a critical distance of 400 μm between these pSi areas, above which the explosion would not transmit from one area to the next, a significant observation which could lead to dense arrays of energetic pSi across a wide area.

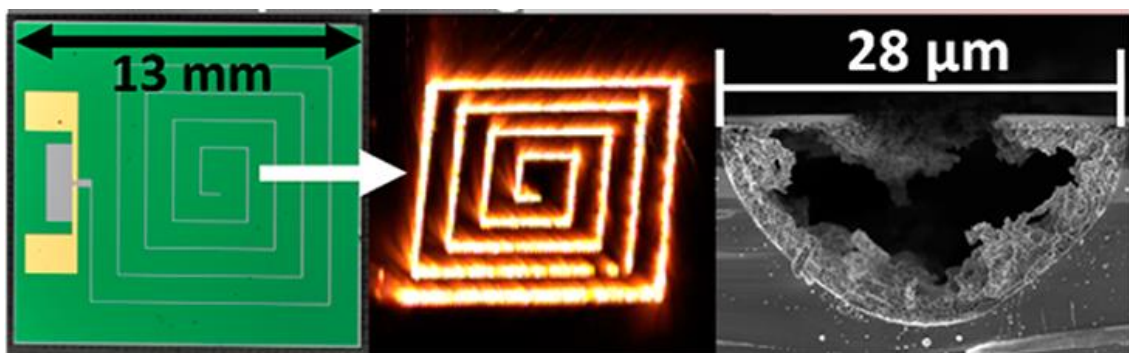


Figure 3-10: Linear burning along convoluted paths of narrow pSi channels loaded with SP (106)

Becker *et al.* (98) conducted experiments and directly observed the production of a fireball and shockwave emanating from an exploding pSi surface loaded with SP. Shockwaves were recorded as travelling at up to 1127 $\text{m}\cdot\text{s}^{-1}$ in air. Such waves may be strong enough to ignite subsequent materials in an explosive train of which pSi forms the first element, again leading toward real-world applications of pSi energetic materials. Furthermore, they observed that the fireball lasted for approximately 3 times longer for samples ignited in air compared to

identical samples ignited in a N₂ atmosphere, which is direct evidence for the afterburning phenomena expected for fuel-rich energetic materials.

While on-wafer applications of pSi energetic materials dominate the work reviewed in this Thesis, several groups have started incorporating the material into more complex mixtures. Parimi *et al.* (104) exploited the high sensitivity of pSi / SP energetic materials to enhance the ignitability of more powerful Al / CuO nanothermites. Thiruvengadathan *et al.* (69) used pSi nano-powders and nano-wires formed by DC arc discharge, mixed with SP, to form an energetic material with electrostatic discharge (ESD) sensitivity compared to various aluminium based nano-thermites. Such applications, while not directly relevant to this Thesis, indicate that pSi energetic materials are increasingly of interest to workers in the field of nano-energetic materials.

Chapter 4 SENSITIVENESS OF POROUS SILICON ENERGETIC MATERIALS

The response of pSi energetic materials to the common stimuli of impact, friction and electrostatic discharge was investigated. The major finding being that the material is as sensitive as comparable primary explosives.

These results were published in:

Plummer, A., Kuznetsov, V., Gascooke, J., Shapter, J., and Voelcker, N.H, 2016, "Sensitiveness of porous silicon based nano-energetic films," *Propellants, Explosives, Pyrotechnics*, 41, pp1029-1035.

4.1 Introduction

The explosive behaviour of pSi films impregnated by an oxidising agent has been recognised and steadily investigated since 1992 (84). The behaviour originates from the very high internal surface area of pSi which permits a very intimate mixture between the oxidising agent and the fuel (silicon), leading to materials that are stable at room temperature and are able to react explosively upon application of an energy stimulus. Indeed, pSi energetic materials prepared in this way are sensitive to a wide variety of stimuli. Methods of initiation that have been reported include heating using for example a hot-plate (64) or hot bridge-wire (53, 71), or by an electrical spark (37). Additionally, laser ignition of pSi energetic materials has been reported using a variety of wavelengths and laser fluences (37, 48, 71, 117).

Throughout the work presented in Chapter 3 it was noted that pSi energetic materials loaded with SP were very sensitive to initiation. Any event which tended to fracture the loaded surface (e.g. dropping a sample onto the bench, scratching a sample, etc.) would cause it to initiate promptly. Extreme care needed to be taken to prevent mishandling and premature initiation. Similar behaviour has also been observed in several reports that pSi energetic materials are highly sensitive to initiation by weak mechanical stimuli such as scratching or mechanical fracture (84). Interestingly, pSi samples loaded with PFPE were noticed to be remarkably insensitive to initiation by mechanical disruption. Whereas all samples (PFPE and SP alike) would initiate promptly using the 100 mJ high voltage spark, PFPE loaded samples did not initiate under the same “mishandling” as SP loaded samples.

Cautionary notes are present in much of the work reported on pSi which recognise the hazards posed by these materials and serve as a reminder to readers to handle the materials carefully. In order to fully realise the potential for these materials to be adopted into widespread use, the sensitiveness to initiation by various stimuli must be quantified. Standard tests are available to measure the sensitiveness to impact, friction and electrostatic discharge (ESD) enabling pSi energetic materials to be compared to more conventional alternatives (25). Mason (91) reported that silicon nanoparticles (<100 nm particle diameter) loaded with sodium perchlorate (SP) would not initiate if struck by a drop-weight (unspecified mass) from a height of 0.38 m but would initiate if the weight was dropped from a height of 2.20 m. Churaman *et al.* (50) found that pSi films loaded with SP would not initiate when subjected to sudden acceleration forces at up to 5131 g. Mason (91) further reported that mixtures of silicon nanoparticles and SP would initiate if subjected to electric sparks having energies of less than 1 mJ. Terry *et al.* (79) reported that similar mixtures of SP and silicon nanoparticles had ESD initiation thresholds of between 16 and 25 mJ. Similarly, Subramanian *et al.* (68) reported that pSi powders would initiate with ESD spark energies of 25 mJ, while Thiruvengadathan *et al.* (69) determined that adding pSi microparticles to an Al / CuO nanothermite reduced ESD sensitiveness to approximately 100 mJ.

Although sensitiveness data is available for particulae or powdered pSi energetic materials, no such measurements exist for on-wafer variants. It is the aim of the work presented in this Chapter to determine the sensitiveness of SP and PFPE loaded pSi energetic materials to impact, friction and ESD.

4.2 Materials and experimental methods

4.2.1 Porous silicon preparation

Porous silicon was prepared using the standard method (Section 2.1) from p-type boron doped wafers, 3 – 6 $\Omega\cdot\text{cm}$ resistivity, <100> orientation, etched in 20% HF / ACN electrolyte, at a current density of 45 $\text{mA}\cdot\text{cm}^{-2}$ for 45 minutes (66% duty cycle – 30 minutes of applied current). Previous work has determined that these etching conditions produce pSi surfaces with pore diameters of 3.6 ± 1.4 nm, 59.9 μm thick, and a porosity of $64.7 \pm 0.5\%$ (97).

For all investigations reported here the pSi layer remains attached to the supporting Si wafer. In this configuration, only the pSi forms the reactive material and the supporting wafer takes no part in the reaction (41).

4.2.2 Loading of oxidant into pSi

As noted earlier, pSi loaded with SP would initiate with light mechanical pressure. Accordingly, samples were cut to the suitable size of the experiment (typically 6 x 6 mm^2) prior to loading with 5 μL of SP solution (400 $\text{g}\cdot\text{L}^{-1}$ in MeOH). It was noted in Section 3.3.5.1 that SP had a tendency to precipitate on the exterior face of the pSi rather than within the pore structure. This same effect was observed when loading pre-cut samples, and required very careful drying with a gentle N_2 stream prior to storage in a desiccator. Nevertheless, minor precipitation on the exterior face was present for all samples, which needed to be gently removed using a soft cotton swab, leading to some uncertainty as to the exact NEQ for each

sample. Under these conditions, a 6 x 6 mm² sized sample loaded with 5 µL of SP solution would have a NEQ of 2.6 mg (by calculation).

pSi loaded with PFPE, however, showed no such initiation sensitivity, and loaded wafers were able to be cut to size after loading with 200 g.L⁻¹ PFPE in FC-75 solvent.

4.2.3 Sensitiveness testing

Samples were initially screened for sensitiveness using simple screening laboratory tests as a means to subjectively assess the potential sensitiveness of the sample. Impact sensitiveness was evaluated by striking a sample with a steel hammer against a stainless steel backing plate, observing any visual or auditory evidence of a reaction, while friction sensitiveness was evaluated by scratching the surface with a stainless steel spatula.

Following the simple indicative tests, quantitative measurements were performed using standard lab-based instrumentation. Impact sensitiveness was measured on a Rotter Impact apparatus (5 kg drop weight) (118) and was conducted by successively lowering the height from which the weight is dropped, until the point at which ignition was not observed (Figure 4-1). Subsequently, the drop height was raised or lowered up to 50 times to determine the threshold impact energy. The minimum height from which the weight could be dropped was 10 cm. Friction sensitiveness was measured on a Julius Peters BAM Friction apparatus (118), increasing or decreasing the applied weight until six successive samples failed to ignite at the selected test level (Figure 4-2). ESD sensitiveness was measured on a custom-built high-

voltage discharge instrument with pre-determined spark energy levels of 0.045, 0.45 and 4.5 J, again seeking the level of energy at which 6 successive samples would fail to ignite. For these three tests, evidence of an ignition at any particular test level was determined either directly (by actually observing an ignition event), or indirectly by observing the state of the material after the test (unreacted pSi has a dark purple / black glassy appearance, whereas reacted material has a dull powdery brown appearance).

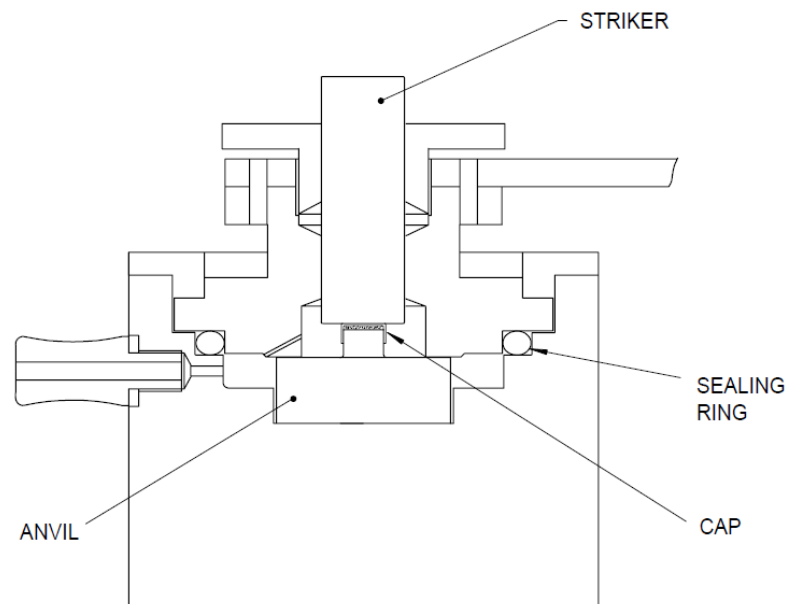


Figure 4-1: Sample confinement in Rotter Impact Test. Samples of pSi energetic material were sandwiched between the hardened steel anvil and the brass cap. The 5 kg drop weight falls under gravity, colliding with the striker and thereby impacting on the sample (118).

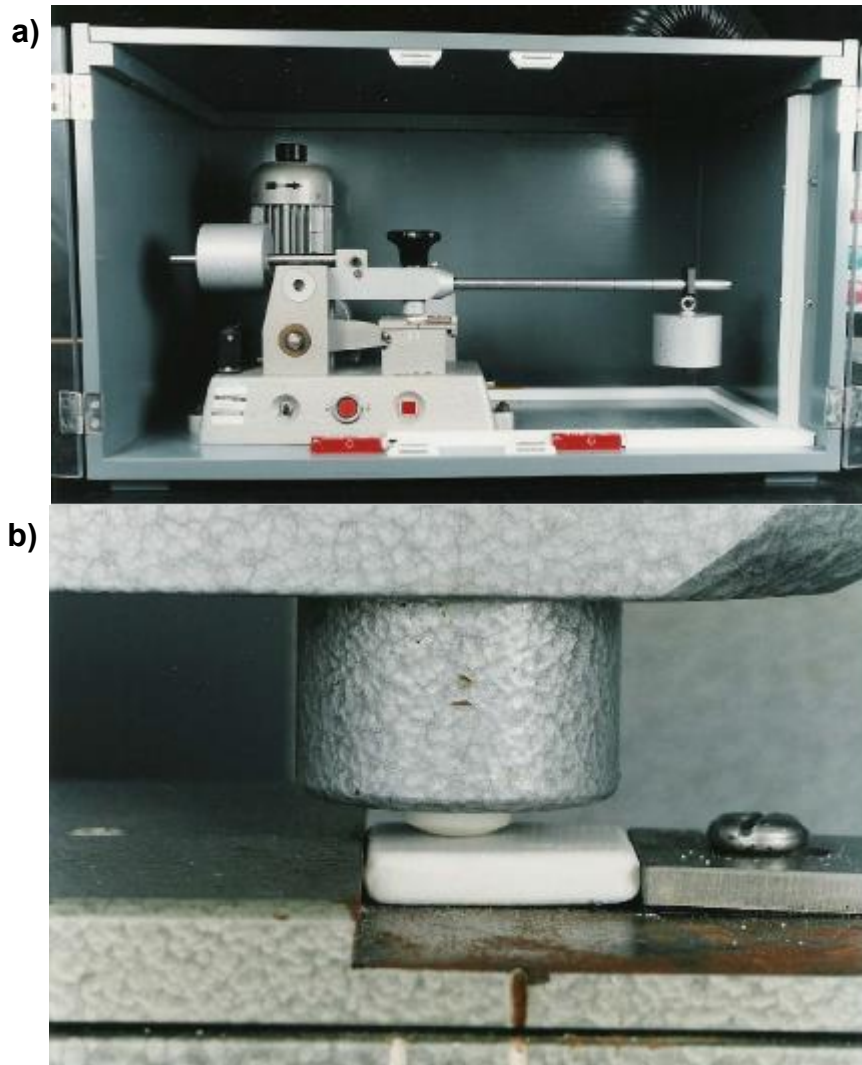


Figure 4-2: a) BAM friction apparatus indicating weight suspended on armature, and b) detail view of interface between ceramic piston and base plate (118).

4.3 Results and discussion

4.3.1 Initial sensitiveness screening

All samples (both SP and PFPE) initiated promptly when subjected to a 100 mJ electric spark during burning rate experiments described in Section 3.2.1.

Samples loaded with SP also initiated promptly when subjected to a very weak strike with a hammer, or if the surface was scratched by a stainless steel spatula, reinforcing the earlier observations that these materials are extremely sensitive. Moreover, any process which exposed a fresh face in the pSi surface (such as snapping a sample in half) would cause initiation in almost every instance if the sample was loaded with SP.

However, samples of pSi which were loaded with PFPE did not initiate when struck with a hand-held hammer, nor if scratched with a spatula. The strength of the hammer strike was sufficient to crush the wafer and cause a slight dent in the stainless steel backing plate, while the amount of force applied with the spatula to assess friction was sufficient to fracture the pSi surface. Fragments of these samples were then subjected to electric spark initiation and verified that the samples remained energetic even after these treatments.

4.3.2 Instrumented sensitiveness testing

A second series of samples were prepared and subjected to the instrumented friction, impact and ESD tests, with the results presented in Table 4-1. In these tests, the sizes of the etched samples were greater than the space available within the respective instruments. As described earlier, etched wafers were fractured into smaller sections ($\approx 6 \times 6 \text{ mm}^2$) prior to being loaded in the normal manner, and only one section of wafer was tested at any one time (i.e. multiple small sections were not combined to re-form the original sample mass). Whilst this is a slight

deviation from the normal form of the material, it was felt that having only a single cut wafer sample would be representative of the behaviour of the material in its un-sectioned form.

Table 4-1: Initiation sensitivities of pSi loaded with SP or PFPE (n = 6).

	pSi / SP	pSi / PFPE	Lead azide	Nitroglycerine
Impact	<4.9 J	<4.9 J	2.5 – 6.5 J ^a	0.2 J ^a
Friction	< 5 N	> 360 N	0.1 – 1.0 N ^a	>353 N ^a
ESD	<0.045 J	>0.045 J, <0.45 J	0.05-0.06 J ^b	

a Ref (28).

b: Ref (119).

pSi loaded with either SP or PFPE was found to be sensitive to initiation by impact at below the limit of detection for the available instrumentation, which precluded calculation of a Figure of Insensitiveness usually expressed for this test. Whilst this is expected for pSi/SP, the result was surprising for pSi/ PFPE when considering that this material was insensitive to a sharp strike from a steel hammer. The instrumented drop-weight test sandwiched the energetic material sample between a steel anvil and a brass cup, as per the standard configuration for this test (Figure 4-1). This effectively created a small pocket of air, which could be compressed upon impact and thereby heated adiabatically (25). The hammer-strike test was not sealed in this manner and air between the sample and the impacting surfaces would escape without being heated. This extra heating of the sample due to adiabatic compression of the trapped air volume during the drop-weight test may explain the difference in the observed results between these two tests. Whereas Mason (91) reported the sensitiveness of pSi / SP nanoparticles to be between 0.38 and 2.20 m drop height, this system is not directly comparable due to the different morphology of the samples described here (on-wafer pSi vs nanoparticles).

The nature of the samples under investigation required a slight deviation from the standard form of the BAM Friction test. Specifically, the energetic material (pSi loaded with oxidising agent) was rubbed between the ceramic pistil of the apparatus and the supporting Si wafer instead of a ceramic base plate as required by the test. When loaded with SP, samples were found to initiate at the lowest limit of detection. The fact that the SP loaded material initiated at the lowest limit of detection gives confidence that the result accurately represents the sensitive nature of this energetic material in spite of the slight deviation from the standard BAM test. However, when loaded with PFPE no sample initiated even at the greatest applied force – at this level (360 N) the supporting Si wafer was pulverised when the energetic material was rubbed between the two ceramic surfaces of the apparatus.

Again as expected, samples of pSi loaded with SP initiated at the lowest limit of detection for ESD sensitiveness. Loaded with PFPE, samples would not initiate at 0.045 J, but initiated reliably at 0.45 J. However, it is also noted that samples of pSi loaded with PFPE would initiate reliably with a spark energy of 0.1 J during the burning rate testing described in Chapter 3. The true threshold level for pSi / PFPE is therefore between 0.045 and 0.1 J spark energy. In spite of the differences in the form of the samples (on-wafer vs particles), these results are broadly in accordance with Subramanian *et al.* (68) and Terry *et al.* (79) for pSi loaded with SP.

The impact, friction and ESD sensitivities of pSi based energetic materials are analogous to other sensitive energetic materials. For example, the behaviour of pSi loaded with SP is very similar to the primary energetic material lead azide for all three modes of initiation investigated here (28). However, pSi loaded with PFPE can exhibit high sensitiveness to impact under certain conditions but displays low sensitiveness to friction, and only moderate ESD sensitiveness. Whilst this might seem incongruous, sensitiveness to one mode of initiation is not a predictor to sensitiveness by another mode – nitroglycerine is an example of an energetic material which displays high impact but low friction sensitiveness (28).

4.4 Conclusions

Porous silicon based energetic materials were studied to determine their sensitiveness to common modes of initiation. When loaded with SP, the energetic material was found to be sensitive to impact, friction and ESD at the lowest limit of detection for the available apparatus. PFPE was found to be slightly less sensitive to ESD than SP, and insensitive to friction. However, it was determined to be very sensitive to impact using the Rotter Impact Apparatus. This was in contrast to the observation that pSi / PFPE energetic material did not initiate when struck sharply with a steel hammer, reinforcing the difficulty of applying standard high-explosive sensitiveness tests to this novel material. Nevertheless, it was concluded from these results that pSi based energetic materials should be regarded as having the sensitiveness of primary explosives, and afforded all appropriate care with which those types of energetic materials are handled. Finally, while pSi loaded with PFPE has a lower burning rate compared to pSi/SP systems, PFPE may be a viable alternative to SP as an oxidising agent for certain applications of pSi energetic material systems. An example of this

could be initiation systems subject to high levels of vibration (and therefore friction within the pore matrix) but which are otherwise protected from impact or ESD.

Chapter 5 LASER SHOCK IGNITION OF POROUS SILICON ENERGETIC MATERIALS

Initiation of pSi loaded with SP was achieved via indirect laser illumination and due to a laser generated elastic wave in an effort to improve the potential versatility of the system. Measurement of the speed and particle velocity of the elastic wave was achieved through use of an interferometric technique (photon Doppler velocimetry).

These results were published in:

Plummer, A., Kuznetsov, V., Gascooke, J., Shapter, J., and Voelcker, N.H, 2014, "Laser shock ignition of porous silicon based nano-energetic films," *Journal of Applied Physics*, 116, p054912.

5.1 Introduction

Other work in this Thesis and elsewhere has demonstrated that pSi will initiate through various mechanical and electrical stimuli. An interesting alternative to these methods is ignition by laser illumination.

Laser ignition of pSi energetic materials has been reported at a variety of wavelengths and laser fluences (37, 48, 71). In each of these instances the laser directly illuminates the pSi surface to cause ignition. This arrangement may cause difficulties for incorporating pSi in assembled devices if the surface needs to be both in contact with a receptor charge yet exposed enough to be able to be illuminated by the laser. The use of shockwaves to cause ignition of these materials has not been well documented, and application of simple laser-generated shockwaves may represent one possible solution to this problem (120, 121). In all instances, it is reported that the initiating stimulus either desorbs the hydrogen from the surface, or fractures the pSi crystals, in such a way that exposes the unreacted Si surface to the oxidising agent (51). Small reactions at the site of initiation liberate sufficient energy to accelerate reaction rates to the desired explosive reaction.

Furthermore, in order to model energetic pSi systems, it is necessary to understand the material properties of the system, including the behaviour of the material when subjected to shock loading (120). Shock compression experiments, which record the speed of the shockwave travelling through the material and the velocity of the material accelerated by the wave (i.e. the particle velocity), are one aspect of the work required to derive the pressure and density of the shockwave through application of the Rankine-Hugoniot equations (120).

Standard shock compression experiments applied to conventional energetic materials, such as the Hopkinson split-bar technique or explosively driven plane-wave generators (121), far exceed the scale of pSi energetic systems, and are therefore unsuitable. Laboratory scale techniques for shock generation are also well known and are applicable to micro-scale experiments (121). A convenient and routine technique is to use moderate to high energy laser pulses to irradiate a surface to generate a short duration plasma – the rise and fall of the pressure associated with this plasma will generate a shockwave emanating from, and driving into, the surface (122, 123). The efficiency with which the wave can be directed into the surface under investigation can be increased by adding a confining layer to trap the plasma between two surfaces, and adding an absorbing layer to convert the laser energy to heat, thereby increasing the plasma pressure (122). The compression wave generated in this manner can be considered to be one dimensional for thin samples which will decay in intensity as it travels through the sample depth (124).

The shockwave generated by any of these techniques will travel through the bulk material, emerging at the opposite surface. Simply measuring the transit time of the wave through the known thickness of the material will determine the wave velocity. However, measurement of the particle velocity is more problematic. Techniques such as spaced electrical contact probes are suited to large shocks emerging from bulk energetic materials (120). By measuring the wave profile through a receptor having well characterised material properties (e.g. PMMA) it is possible to derive the properties of the shock donor (i.e. the material under investigation), but again this is a technique suited to bulk energetic materials (120).

The face of the target opposite to the donor shock is termed the “free surface” when it is unrestrained by another material and the wave can exit to the atmosphere. The velocity of the free surface accelerated by the emerging wave is directly proportional to the particle velocity as follows (29):

$$U_p = \frac{U_{fs}}{2} \quad \text{Equation 5-1}$$

where U_p is the particle velocity and U_{fs} is the free surface velocity (m/s). Optical interferometric techniques (such as the velocity interferometer system for any reflector, VISAR) are suited to measurement of the free surface velocities for both large and small scale shocks (120), and may easily be implemented in a laboratory environment. Similarly, by utilising the shocked or stressed sample as the displacement mirror of a Michelson interferometer, the adhesion of thin aluminium films on silicon or silica substrates impacted by laser-generated compression waves has been characterised (124). Photon Doppler velocimetry (PDV) has emerged as a simple technique for measurement of U_{fs} using relatively inexpensive off-the-shelf fibre optic components (123, 125, 126). By using the optical interference of Doppler-shifted light that is reflected from the moving target surface one can record U_{fs} as a function of time.

In this investigation, the laser shock initiation properties of pSi energetic materials are studied using PDV to determine the nature and strength of the shockwave at the threshold for initiation.

5.2 Materials and experimental methods

5.2.1 Porous silicon preparation

pSi was prepared using the standard method (Section 2.1), etching circular samples (15 mm etched area, 1.76 cm^2) for either 90 or 180 duty cycles (15 or 30 mins of applied current) at a current density of $45 \text{ mA}\cdot\text{cm}^{-2}$ in 20% HF / ACN electrolyte. Previous work (Section 3.3) has determined that these etching conditions produce pSi surfaces with pore diameters of $3.5 \pm 1.7 \text{ nm}$, a porosity of $64.7 \pm 0.5\%$, and thickness of 24.9 and $49.9 \mu\text{m}$, respectively. Energetic pSi was formed when required by loading the etched surface with SP ($400 \text{ g}\cdot\text{L}^{-1}$ in MeOH) adjusting individual sample volumes according to Equation 2-2.

5.2.2 Photon Doppler Velocimeter

The system used during this investigation is depicted in Figure 5-1.

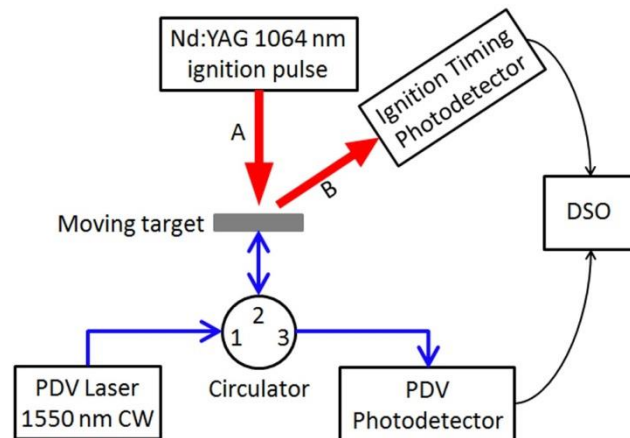


Figure 5-1: Schematic of the home-built PDV system used in this study. The 1550 nm CW laser is aimed at the front surface of the target, via the three port circulator, and is recorded on the digital storage oscilloscope (DSO). The 1064 nm laser pulse (A) is reflected from the rear surface of the target (B) and captured by a second photodetector to function as a timing reference.

Light from a continuous wave laser is fed into Port 1 of a three-port optical circulator, emerges from Port 2, and illuminates the moving target through an optical probe (Figure 5-1). However, a small fraction of this light will reflect back along the fibre from the cleaved end of the probe without interacting with the target (126). The reflected light from the moving target is Doppler-shifted, and interferes with the unshifted light inducing a beat wave. The beat wave propagates back into Port 2, and emerges entirely from Port 3. The variation of the beat wave is registered by a photodetector and is recorded by a digital storage oscilloscope (Figure 5-2).

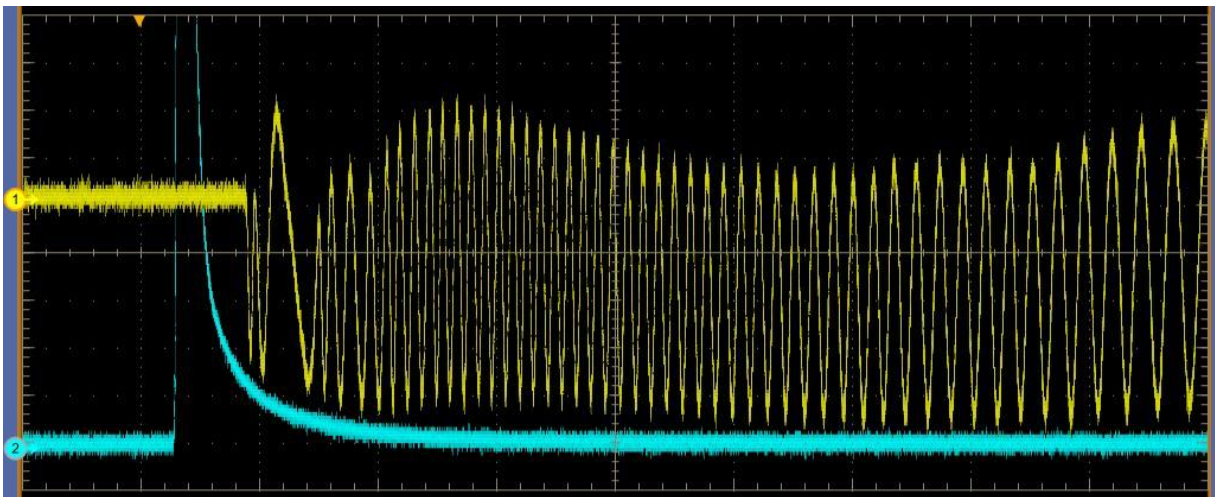


Figure 5-2: Screen shot of DSO output, depicting Channel 1 (PDV photodetector, yellow trace) and Channel 2 (timing photodetector, blue trace). Variation in the beat frequency recorded by the PDV is directly related to the changing velocity of the surface. Time scale is 50 μ s per division.

The frequency of the beat wave is related to the target velocity as follows (126):

$$U_{fs} = \frac{f \lambda}{2} \quad \text{Equation 5-2}$$

where f is the beat frequency and λ is the wavelength of the source laser light. This simple relationship permits calculation of U_{fs} by directly measuring the beat frequency. Processing

the recorded beat frequency signal from the oscilloscope thus permits measurement of U_{fs} as a function of time for the shock event under investigation.

The PDV system utilised an NKT Photonics Koheras Adjustik C15 laser (1550 nm operating at 80 mW). This was fed through an AFW Technologies three-port circulator (model CIR-3-15-C-1-2) via a SMF-28e single mode fibre. The optical probe illuminating the target surface consisted of the stripped and cleaved end of the fibre placed perpendicular to the surface at a distance of approximately 0.5 mm. The light intensity emerging from Port 3 of the circulator was measured using an Electro Optics Technologies ET-3000A-FC photodetector connected to a Tektronix DPO7254C oscilloscope. The recorded waveforms were later processed using a MATLAB short-term Fourier transform routine to yield surface velocity as a function of time.

5.2.3 Laser shock generation

Confined plasmas were generated by clamping Si wafer samples against a glass microscope slide and irradiating the sample with single pulses of 1064 nm laser radiation. Prior to clamping, a layer of black paint (Dulux matt black spray paint) was applied to the surface of the glass facing the wafer and allowed to dry. The glass and the wafer were in immediate contact. The black paint had a measured thickness of $27 \pm 4 \mu\text{m}$ (determined by SEM), and was believed to be slightly porous in nature, as depicted in Figure 5-3. More predictable coatings including sputter coated gold (50 and 100 nm thick) on the glass surface were trialled, however these were found to be too reflective and failed to absorb enough of the incident 1064 nm laser radiation to provide reliable ignition.

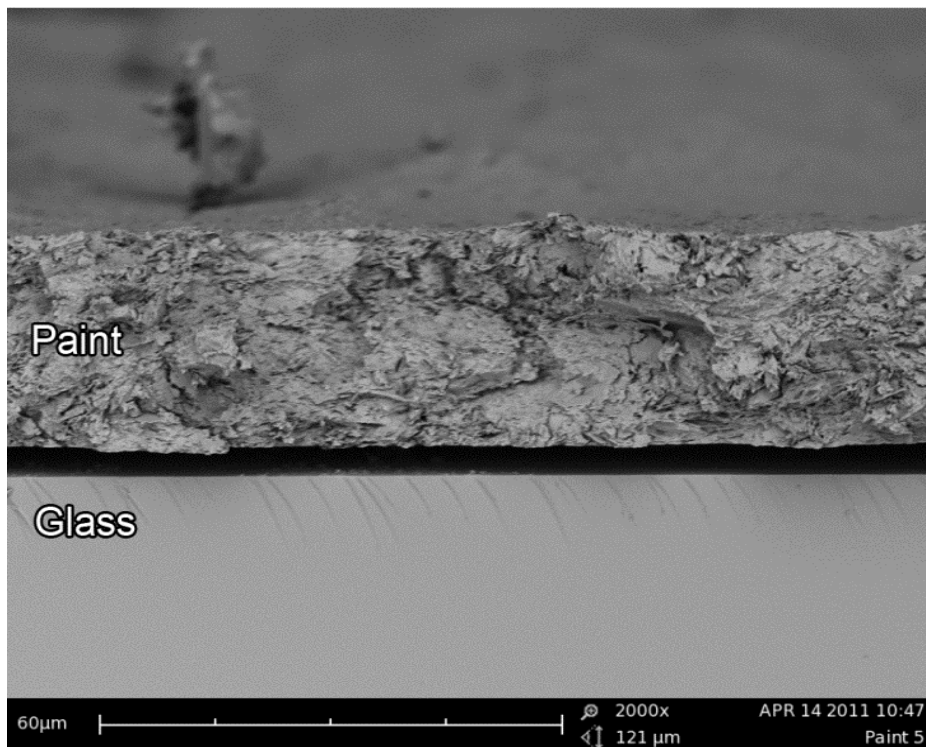


Figure 5-3: SEM image of the absorbing black paint layer on the glass slide used to generate confinement, showing delamination of the paint from the glass during preparation of the cross-sectional samples for imaging.

The glass and wafer were clamped together using an aluminium sample holder having a 12.5 mm diameter circular aperture on both the front and rear faces to permit unimpeded laser irradiation from both sides (Figure 5-4(a)) – the glass and paint layers can also be omitted to permit the 1064 nm laser to interact directly with the backside of the Si wafer (Figure 5-4(b)).

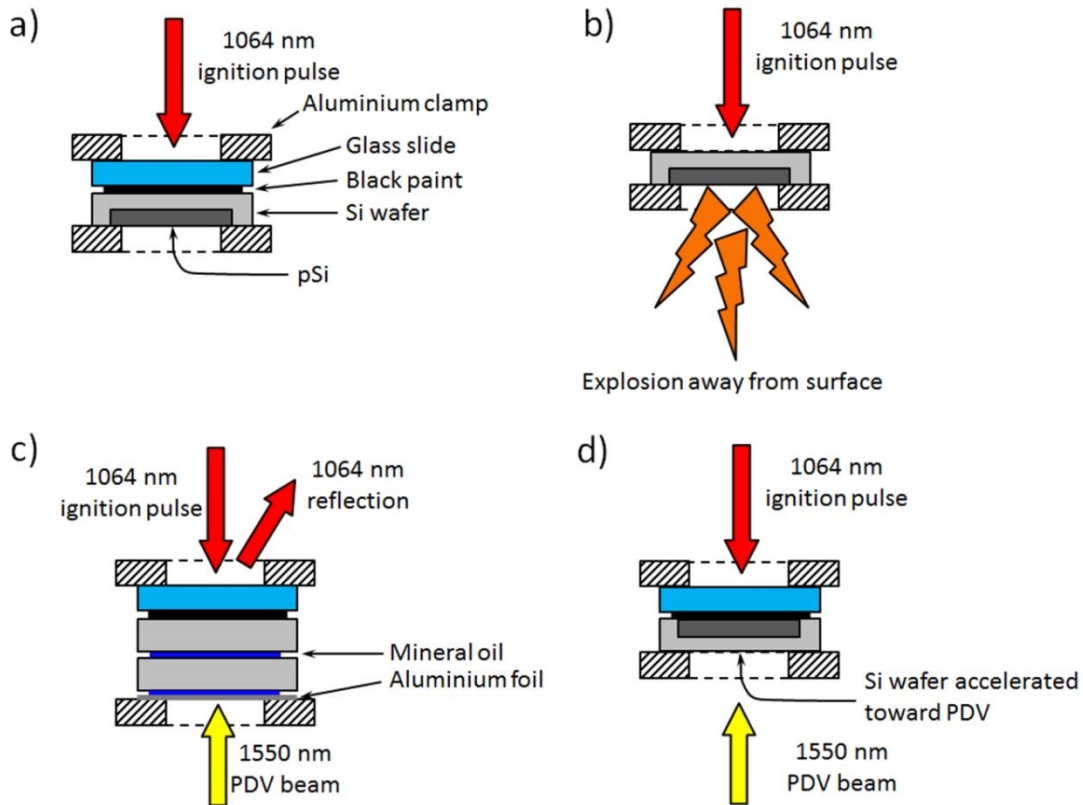


Figure 5-4: a) Sample assembly for laser shock initiation of pSi samples, b) Sample assembly for “laser thermal” ignition, c) Sample assembly for simultaneous recording of wave and particle velocity of unetched Si (two unetched Si wafers are depicted, however, up to three layers could be effectively assembled in this manner), and d) Sample assembly for recording of wafer acceleration due to exploding pSi.

Laser irradiation was performed by a Continuum Surelite III Q-switched Nd:YAG laser (1064 nm, 10 ns single pulse, spot size of approximately 7 mm). The energy of the laser was measured using a Vector H310 power meter with a Scientech AC2501 detector head, and was found to have a pulse-to-pulse error (standard deviation at 95% confidence interval) of between 3.7% (50 mJ pulses) to 2.6% (925 mJ pulses). An Electro-Optics Technology ET2030 photodiode was positioned behind the sample to capture reflected 1064 nm light to provide a timing reference (Figure 5-1 and Figure 5-4(c)), recorded simultaneously with the PDV signal. For clarity, the side of the sample which is illuminated by the 1064 nm laser is

referred to as the backside, while the side which faced the PDV probe is referred to as the frontside (Figure 5-5). Wang *et al.* (124) described a similar experimental arrangement to study aluminium film adhesion on silicon and silica substrates, and conducted an analysis which concluded that the shockwave generated by this method was essentially planar as it travels through the sample, for a distance of 2 to 3 times the radius of the laser spot (i.e. through a sample thickness of 7 to 10 mm for the experiments reported here). Therefore, errors associated with stress dissipation at the edges of the shocked area were minimised by aligning both the 1064 nm incident laser pulse and the 1550 nm PDV probe to the approximate centres of the back- and front-side, respectively.

The source silicon wafers used during this investigation were approximately 388 or 502 μm in thickness. Shock velocity experiments required successively thicker samples to determine velocity parameters, which are not commercially available. Thus, multiple layers of Si were stacked together, up to a maximum of approximately 1200 μm . It was found that a thin layer of light mineral oil was needed between each layer in order to provide effective coupling and transmission of the shockwave (Figure 5-4(c)). The mineral oil (Sigma Aldrich, density 0.82 g.cm^{-3} , viscosity $<30 \text{ cps}$) was added as a single drop between successive layers during stack assembly, and the entire stack clamped between two flat plates for 5 minutes. The average oil layer thickness by this method was determined to be 1.4 μm as inferred from the measured layer and stack thicknesses. Thus, whilst there are differences between the densities of the two materials (Si and oil) which will have some effect on the wave transmission, it was believed that this would be minimal due to the relative thicknesses of the layers.

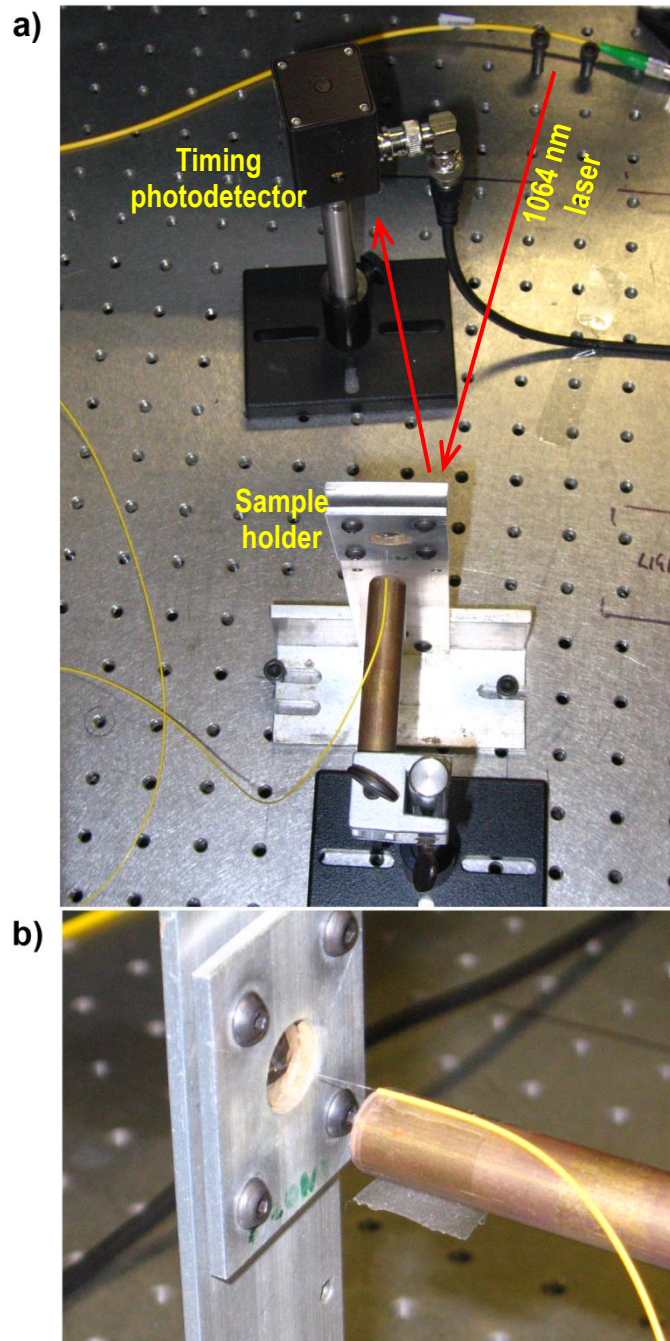


Figure 5-5: PDV system depicting a) location of timing photodetector to rear of sample holder, and b) position of PDV probe (yellow fibre optic cable) near to front side of sample surface through the circular window of the clamping assembly.

The Si wafer surface had a high specular reflectivity. A deviation of few degrees from the normal angle of 1550 nm laser light incidence resulted in the loss of the PDV beat signal. The

use of a thin layer of matte aluminium foil ($12.2 \pm 0.8 \mu\text{m}$ thick) in a configuration similar to that reported by Asay (127) was necessary to provide a diffuse reflective surface in order to obtain a suitable PDV signal. The acoustic impedance of the Si and Al is similar (19.6 and 17.3 MRayls, respectively (35)) and therefore it was anticipated that introduction of the extra layer would not significantly influence the recorded wave or free surface velocities.

Wafer stack thicknesses were measured using a Mitutoyo Digimatic digital micrometer.

5.3 Results and discussion

5.3.1 Laser shock initiation

To firstly determine if pSi loaded with SP could actually be initiated by a laser-generated shockwave, samples of pSi loaded with SP were configured as per Figure 5-4(a), and irradiated by pulses of 1064 nm light from the Nd:YAG laser. Prompt initiation was observed upon application of a single laser pulse indicating that this was a viable technique to initiate pSi energetic materials (Figure 5-6). The intensity of the laser was adjusted to achieve a 50% probability of initiation, the threshold being determined to occur at laser pulse energies of 130 mJ (equivalent to a power density of $3.38 \times 10^4 \text{ kW}\cdot\text{cm}^{-2}$). As it is known that these materials are very sensitive to mechanical stimuli, and also that Si is partially transparent to 1064 nm infrared light (128, 129), it was necessary to determine if the observed initiation was due to a transmitted shockwave or some other effect. Accordingly, mechanical (sample fracturing) or thermal (laser heating) effects needed to be eliminated.

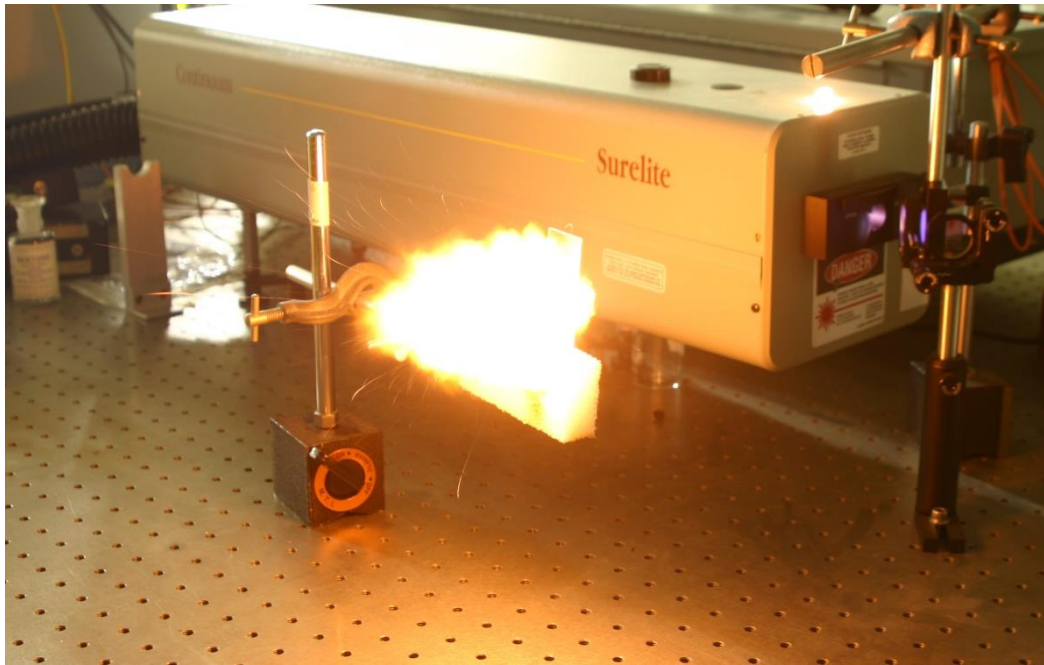


Figure 5-6: pSi loaded with SP ignited using laser-generated shockwave.

In order to isolate the mechanism, samples of pSi loaded with SP were configured as per Figure 5-4(b) - by omitting the confining glass slide and black absorptive layers the 1064 nm ignition pulse can interact directly with the backside of the Si wafer without the generation of a shockwave. It was found that samples would not initiate upon backside illumination at laser pulse energies of 130 mJ, but would initiate if irradiated at energies greater than 650 mJ. Moreover, optical transmission measurements showed that 1.9% of the 1064 nm light was being transmitted through the wafer, suggesting that the small fraction of unabsorbed 1064 nm light impinging on the pSi layer was causing initiation of the sample through heating of the pSi layer (termed “laser thermal” initiation). Accounting for this absorption through the bulk of the Si wafer, this 650 mJ threshold equates to an approximate pulse energy of 12 mJ (equivalent to a power density of $3200 \text{ kW}\cdot\text{cm}^{-2}$) emerging at the frontside and interacting with the pSi to cause initiation. Churaman *et al.* (48) described a threshold of initiation for pSi

loaded with SP of $2.7 \text{ kW}\cdot\text{cm}^{-2}$ (514 nm continuous wave), and Wang *et al.* (71) reported a threshold of $1063 \text{ kW}\cdot\text{cm}^{-2}$ (532 nm, 15 ns single pulse) for pSi loaded with ammonium perchlorate – both reports described direct frontside irradiation. Churaman *et al* (48). found that protecting pSi layers from atmospheric humidity using a thin polymer coating prevented ignition even upon long exposure times to the laser. The threshold reported in this work is considerably higher than these two previous reports, however the partial transparency of Si in the infrared region has been exploited to achieve initiation using indirect backside irradiation. This allows the backside of a Si wafer to function as both a hermetic seal and an optical transmission window for an assembled device incorporating pSi layers as an ignition source.

To eliminate the initiation reaction due to the laser thermal mechanism, samples were prepared with a light-absorbing layer of black paint applied directly to the backside of the silicon substrate, and assembled without providing confinement from a glass microscope slide. In this configuration, initiation of the sample was prevented for laser pulse energies up to 900 mJ (the highest pulse energies used in this study). Although a strong plasma was generated with each laser pulse, ablating the paint away, it was not until 3 or 4 pulses had been applied to individual samples that the sample would initiate. This indicated that the layer of black paint effectively absorbed the 1064 nm laser light until such time as it had been ablated away sufficiently to permit the light to transmit through the sample causing laser-thermal initiation of the pSi layer. In spite of the fact that a shock wave of some strength was generated upon ablation of the paint by the laser (determined observationally through the bright flash and audible “crack” produced upon irradiation), it was not sufficiently strong to cause initiation of the sample.

Finally, to eliminate the possibility that mechanical fracture of the sample at the threshold of initiation (due to the pressure generated by the plasma) was contributing to sample initiation, etched blank samples (i.e. pSi samples but without the SP) in the same configuration as Figure 5-4(a) were irradiated at laser pulse energies of 140 mJ, and cross-sections of the wafer cleaved through the shocked zone were imaged using high resolution SEM. These images are shown in Figure 5-7 and clearly indicate that the porous structure was not destroyed, and that delamination from the supporting Si wafer, spallation at the free surface or any other mechanical failure which might have caused pSi initiation were absent. Furthermore, the shocked samples were visually indistinct from unshocked samples.

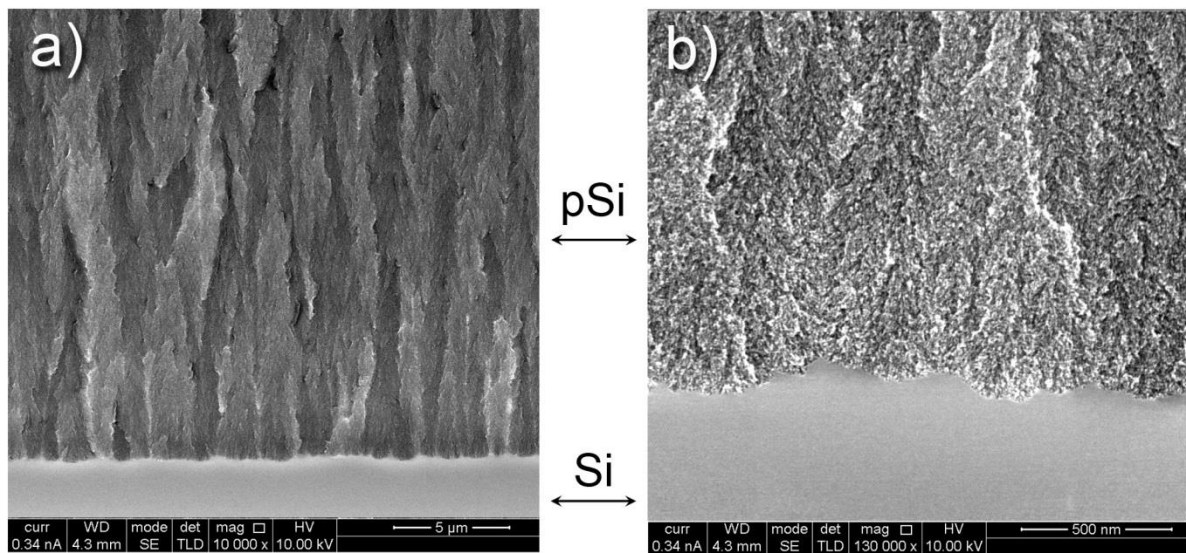


Figure 5-7: Cross-sectional SEM images of pSi layer above supporting substrate after laser-induced shock event ((a) low and b) high resolution). These are indistinguishable from the samples not subjected to laser-induced shock.

So, it was concluded that the development of a shockwave was necessary in order to cause ignition at the threshold of 130 mJ when samples were configured as per Figure 5-4(a).

Mechanical fracturing of the material was eliminated as a possible mechanism at this threshold. A much higher threshold was needed to cause ignition by the laser thermal mechanism (i.e. 650 mJ) - this could occur only in the absence of the confining glass layer, and then only when the 1064 nm laser was unimpeded by the black absorptive paint layer. The exact mechanism of how the shockwave interacts with the pSi to cause initiation has not yet been determined but may include friction between silicon and SP crystals (below the elastic limit of the material) or piezoelectric voltages known to be generated upon stress wave interaction with pSi (129).

5.3.2 Shock wave characterisation.

To determine the intensity and characteristics of the shockwave, the system was configured as per Figure 5-4(b). Unetched Si wafers (or multi-wafer stacks) of between 380 and 1200 μm thickness were shocked with laser pulse energies between 140 and 895 mJ, simultaneously recording both the shock transit time and U_{fs} . The transit time was measured by the difference between the timing photodiode (reflected infrared 1064 nm light) and the onset of the beat frequency. This time difference includes not only the actual transit time of the shock wave, but also all of the system delays including plasma pressure rise time, light transmission through the fibre optic cable etc. The velocity of the wave is the slope of the graph of time of arrival versus wafer thickness, as depicted in Figure 5-8. The wave velocities at 140, 330, 630 and 895 mJ laser pulse energies are 7.0 ± 2.6 , 7.9 ± 2.8 , 8.0 ± 1.7 and $8.5 \pm 3.3 \text{ km.s}^{-1}$, respectively. For comparison, the speed of sound within silicon along the $\langle 100 \rangle$ direction is 8.433 km.s^{-1} (130). As expected, there was an almost linear increase in the time of arrival with increasing Si thickness, and a slight increase in wave velocity with increasing laser pulse

energy. A similar dependency of the wave velocity with laser intensity for laser-shocked aluminium plates, has been reported by Lee *et al.* (131) who observed wave velocities below the speed of sound in the material.

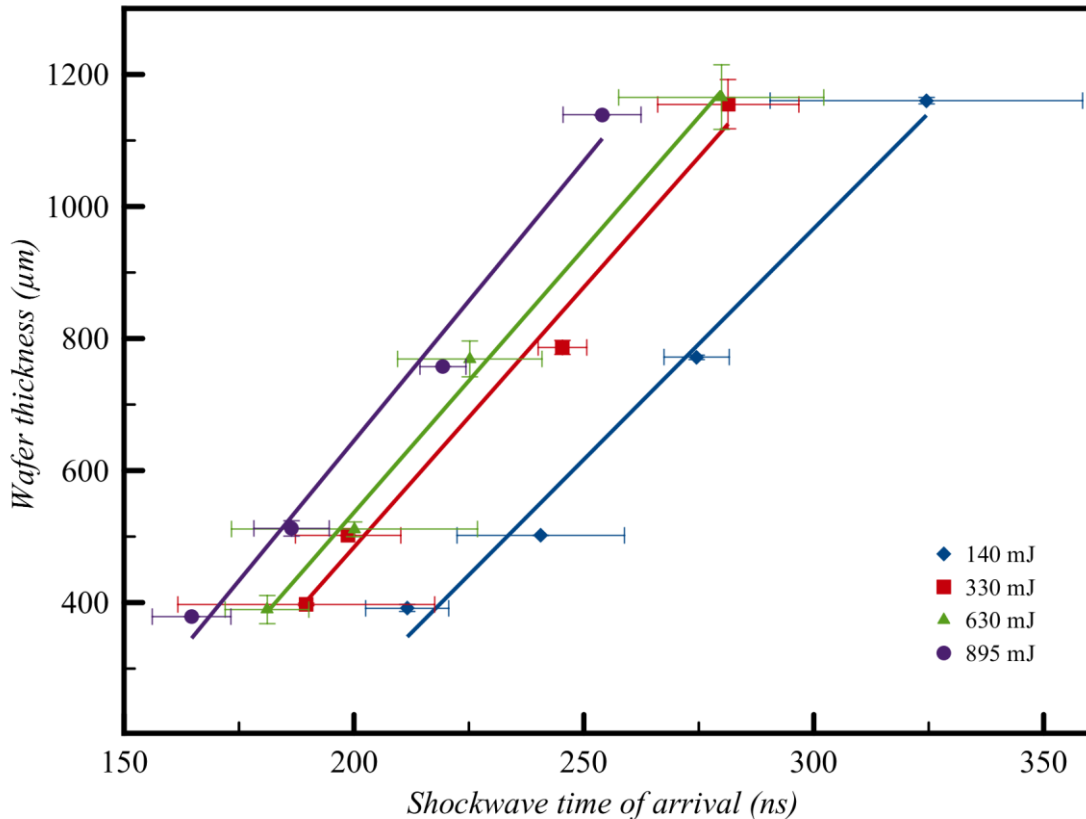


Figure 5-8: Time of arrival of the wave emerging from Si wafers subjected to laser-induced shock wave loading at varying laser pulse energies.

A typical velocity profile of the wave emerging from the surface is presented in Figure 5-9(a). Three distinct phases in the surface velocity profile were observed. The first was a very sudden acceleration of the surface up to a peak velocity, which corresponded to U_{fs} . By restraining the sample in a circular clamp of 12.5 mm, it behaved effectively as a clamped membrane. Upon reaching the maximum deflection permitted by the stiffness of the membrane, movement was halted and the surface decelerated to zero due to pull-back

(phase ii). Small reverberations (seen in many of the samples including those involving only a single Si wafer layer) were seen during phase ii which have not been fully identified, but may possibly be due to oscillation of the membrane or oscillations within the plasma of the absorbing layer. Simultaneously, the entire bulk of the sample is being displaced as a result of the plasma pressure, a process which occurs on a longer time scale and manifests both as flexion of the wafer and subsequent movement of the wafer shards after it fractures. These features (phase iii) are seen as the steady velocity signal between 10 and 25 μs – at this point, the shards of Si struck the PDV probe and terminated the signal.

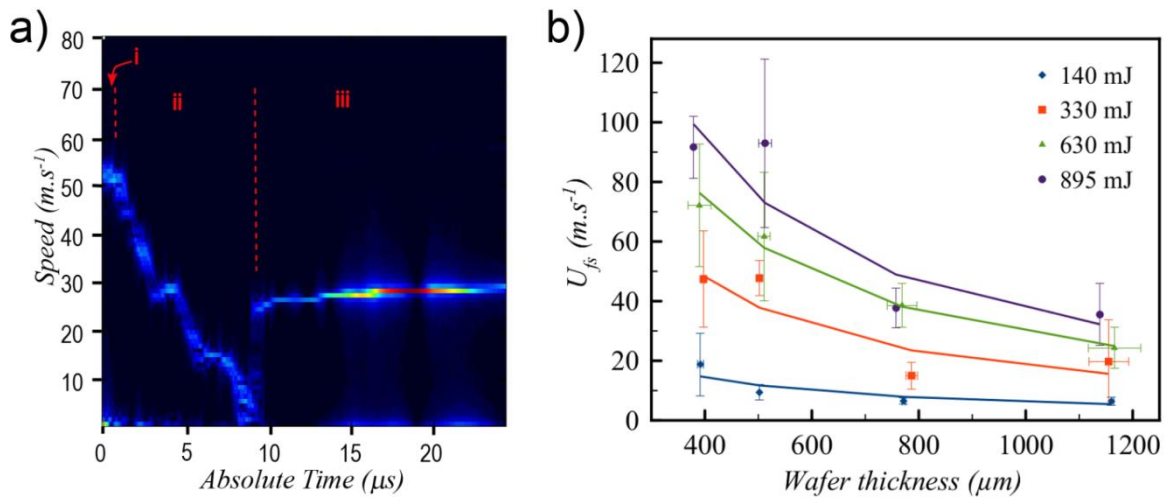


Figure 5-9: A) Free surface velocity profile of a 502 μm thick Si wafer loaded by a shock wave from a 630 mJ laser pulse, depicting the surface acceleration and a peak surface velocity of approximately 52 m.s^{-1} (phase i), surface deceleration due to membrane pull-back (phase ii), and bulk movement of the Si wafer at a velocity of between 25 and 30 m.s^{-1} (phase iii). B) Free surface velocity of Si wafers subjected to laser-induced shock.

The relationship between U_{fs} and wafer thickness at various laser pulse energies is presented in Figure 5-9(b). As expected, U_{fs} was highest for the thinner samples irradiated by the most intense laser pulses, with an exponential like decay as sample thickness increased, suggesting attenuation of the shock wave as it transits through the sample. Again this is consistent with

the observations of Wang *et al.* (124) who also determined that this decay was exponentially related to the thickness of the sample. The rapid deceleration of the wave suggests the shock wave may have transitioned into a stress wave while travelling in the first silicon wafer of the wafer stack (380 μm thick), although more detailed study is required to support this claim.

Fitting of the data presented in Figure 5-8 and Figure 5-9(b) to the linear relationship between wave (U_w) and particle (U_p) velocity (120):

$$U_w = a + bU_p \quad \text{Equation 5-3}$$

where a and b are constants determined from the data, found $a = 6845 \pm 1137$ m/s and $b = 37 \pm 35$. This relationship between U_w and U_p can be used in combination with other Rankine - Hugoniot equations to describe the pressure, density and internal energy of the material associated with the shock. For shockwaves in condensed materials (consisting of both elastic and plastic waves), the constant b is of the same order as the constant a , whereas for purely elastic waves U_w is independent of U_p (29). The low value of b suggests that the observed waves in this system, considering the large observed measurement error, are simple weak elastic waves (i.e. stress waves). Where a material is stressed by a weak elastic wave, the magnitude of the stress (P) is related to the particle velocity, acoustic velocity (C) and Young's modulus ($E = 130$ GPa in the $\langle 1\ 0\ 0 \rangle$ crystal direction) by (29):

$$U_p = \frac{P C}{E} \quad \text{Equation 5-4}$$

For a 380 μm thick silicon wafer irradiated at a laser pulse energy of 140 mJ ($3.6 \text{ mJ}\cdot\text{mm}^{-2}$) an applied compressive stress of 131 MPa was determined – this is comparable to stresses reported by Wang *et al.* (124) who found compressive stress waves of 700 MPa at a laser fluence of $140 \text{ mJ}\cdot\text{mm}^{-2}$ using a similar technique.

Finally, to investigate the effect that exploding pSi has on acceleration of the surface, samples of pSi (380 μm wafer, 68 μm pSi layer) were subjected to shock loading at 140 mJ, recording U_{fs} using the PDV. Here, samples were placed such that the pSi layer directly touched the black absorptive layer and could interact directly with the laser generated shock (Figure 5-4(d)) – this configuration enabled the supporting wafer to function as a mass to be accelerated by the exploding pSi toward the PDV probe. The resulting surface velocity profiles are depicted in Figure 5-10. The unloaded sample (Figure 5-10(a)) clearly displayed a surface velocity peaking at 15 m/s initially, decaying to approximately $5 \text{ m}\cdot\text{s}^{-1}$ by 4 μs – this is very similar to the U_{fs} of unetched Si wafers subjected to the same shock loading ($18.8 \pm 10.5 \text{ m}\cdot\text{s}^{-1}$ – see Figure 5-9(b)).

Introduction of the oxidising agent to create the energetic material resulted in a vastly different profile. Figure 5-10(b) displayed the same initial steady surface velocity of $\approx 5 \text{ m}\cdot\text{s}^{-1}$, but then displayed sudden and almost linear acceleration after 5 μs to a final recorded velocity of $80 \text{ m}\cdot\text{s}^{-1}$ at 22 μs , when the probe is destroyed and the recorded signal terminated. This was equal to an acceleration of $4.4 \times 10^6 \text{ m}\cdot\text{s}^{-2}$. Considering the unit mass of the sample per unit area, this acceleration indicates that an accelerating pressure of 3.9 MPa is developed due to ignition of the energetic material. It must be noted that only preliminary measurements were

conducted in this configuration. However, the recordable differences between the loaded and unloaded pSi samples open the possibility that these techniques may be used to develop the Gurney constants for this material in the future (132).

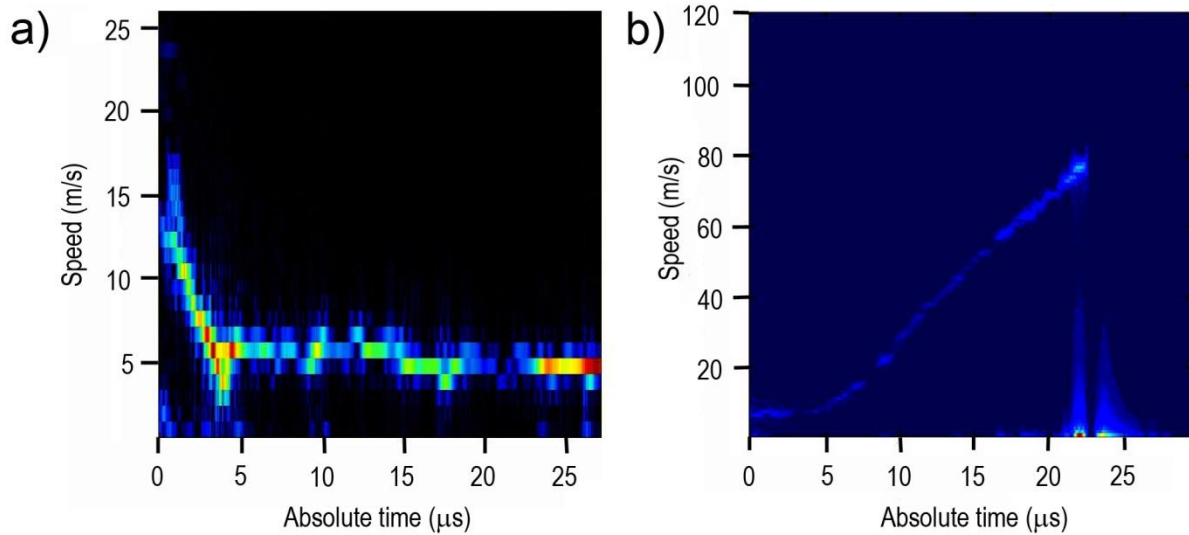


Figure 5-10: U_{fs} profiles of a) unloaded sample (375 μm thick Si wafer with 68 μm thick pSi layer) and b) sample loaded with SP upon irradiation with a 140 mJ laser pulse. The initial peak U_{fs} of the loaded sample is obscured by the resolution of the Matlab signal processing parameters to increase the velocity range to >100 m/s.

It was noted throughout the PDV experiments that the results were sometimes quite erratic with large errors observed in both the U_{fs} and shock time-of-arrival. It was found that the system is very sensitive to even very small deviations in experimental set-up. The PDV probe must be placed at as close as possible to 90° to the surface under investigation, and at a close distance from that surface (≈ 0.5 mm) – even minor deviations had a tendency to reduce the PDV signal to zero. At laser pulse energies greater than 140 mJ, the wafers had a tendency to fracture chaotically, resulting in shards of wafer of inconsistent size within the measurement zone – it is possible that these shards also contributed to the sample measurement error.

5.4 Conclusions

Initiation of pSi films by direct laser irradiation, mechanical impact, electrical sparks and sample heating have been well documented elsewhere. Here, two new methods of initiation of pSi are reported – transmitted laser heating and transmitted laser generated stress waves.

Firstly, it was found that a pSi film loaded with SP is able to be initiated by a weak stress wave propagating through a silicon wafer at a pressure of approximately 131 MPa. This was produced by a laser generated stress wave created at the backside of the wafer, travelling through the bulk silicon material and interacting with the pSi film on the other side of the wafer. The stress wave was weak and elastic rather than a shock wave, with wave velocities somewhat lower than the speed of sound through silicon. Initiation mechanisms due to thermal heating and sample fracturing were eliminated. PDV was shown to be an effective and simple method for recording the motion of the surface where alternative techniques such as VISAR are unavailable.

During this investigation, it was also found that by exploiting the transparent nature of Si in the infrared region, 1064 nm light can be shone through the backside of the supporting Si substrate to heat the pSi energetic material on the front side. The moderately high laser intensities required for this method (a single 10 ns pulse at 650 mJ) reduces the risk of initiation from stray or accidental sources of infrared light.

Conceivably, the fact that pSi energetic samples were able to be initiated using an infrared laser not physically coupled to the sample, either by direct laser transmission or by the generated stress wave, may lead to real-world applications. Physically isolating the initiation and energetic systems provides a degree of safety by reducing the risk of initiation. Furthermore, this also leads to the possibility that devices which incorporate pSi as the primary energetic material may be hermetically sealed from the environment. This would prevent degradation of the material upon oxidation in air and accelerated in moist environments, a problem often encountered with this material.

Chapter 6 THERMAL ANALYSIS OF POROUS SILICON ENERGETIC MATERIALS

To further understanding of why pSi energetic materials are so sensitive to initiation, calorimetric and spectroscopic (FTIR) methods of analysis were employed to study the earliest phases of the reaction. 2D FTIR spectra recorded as a function of temperature and correlated to DSC exotherms, allowed chemical changes within the material to be discovered.

These results have been published in:

Plummer, A., Kuznetsov, V., Gascooke, J., Shapter, J., and Voelcker, N.H, 2017, "Combined thermal and FTIR analysis of porous silicon based nano-energetic films," *RSC Advances*, 7, pp7338-7345.

6.1 Introduction

Chapter 4 of this Thesis reported that pSi energetic materials are very sensitive to initiation, having a sensitiveness consistent with primary explosives, yet displaying a deflagrating explosive behaviour. However, the extreme sensitiveness of pSi to initiation is limiting, preventing real world applications for which the safety of the material is a significant concern. Knowledge of the reaction mechanism between pSi and an oxidising agent is an important factor to help understand the excessive sensitivity, and may assist in the selection of oxidising agent or material treatment regimes in order for these materials to be translated into real-world applications.

Simple bomb calorimetry can determine the total energy released during reaction of a material (25). However, the reaction of an energetic material involves sometimes complex decomposition stages and formation of intermediate species. Investigation of these processes by controlled thermal analysis methods can yield important information, including reaction endo- and exotherms, or intermediate transition or decomposition temperatures all of which gives an insight to the mechanism of the reaction (133).

Investigating the reaction between the pSi surface with liquid oxygen, Kovalev *et al.* (39) first proposed that hydride termination of the freshly etched pSi surface was an essential passivating barrier to prevent spontaneous oxidation. Rupturing the Si-H surface bonds or sub-surface Si-Si bonds by various means created free radicals susceptible to reaction with oxygen. The exothermic reaction between a single Si atom and oxygen molecule releases

sufficient energy to disrupt neighbouring bonds. A single point of initiation can then rapidly cascade up to an explosive reaction.

Churaman *et al.* (51) investigated the mechanism of the reaction between a pSi film (approx. 4 nm pore diameter, 40 μm layer thickness) and SP. Using differential scanning calorimetry (DSC) dehydration endotherms of the monohydrated SP within the pSi pores were observed at approximately 51 $^{\circ}\text{C}$ and 149 $^{\circ}\text{C}$, a phase transition of the SP at 307 $^{\circ}\text{C}$, and finally an explosive reaction at 320 $^{\circ}\text{C}$. No significant exotherms were observed below the temperature of explosion. They concluded that the mixture commenced reaction initially by formation of reactive ions through dissociation of the SP or H_2O during these dehydration steps, which are then free to react with the pSi surface. Again it was observed that the presence of the hydride termination on the pSi surface was essential to promote a strong explosive reaction.

Becker *et al.*(46) investigated the influence of atmospheric conditions on the reactivity of pSi films impregnated with SP. Using bomb calorimetry, freshly etched pSi prepared by galvanic corrosion (up to 150 μm thick layers, 62 to 69% porosity, pore sizes 2.7 to 3.1 nm) loaded with SP yielded gross reaction enthalpies of 9.9 $\text{kJ}\cdot\text{g}^{-1}$ of pSi in a N_2 atmosphere and 27.3 $\text{kJ}\cdot\text{g}^{-1}$ in O_2 . They further observed that oxygen back bonding beneath the hydride-terminated pSi surface resulted in a weak exotherm at about 250 $^{\circ}\text{C}$. This was confirmed by FTIR spectroscopy of samples both prior and subsequent to ignition. In the absence of the hydride termination, no energetic reaction was observed. Hence, the presence of the hydride termination on the pSi surface was essential to enabling the material to react explosively according to the authors. They further concluded that the substantial difference in the total

energy of the reaction recorded between N₂ and O₂ atmospheres was due to the mixture being substantially fuel rich (a limitation imposed by the available pore volume within the pSi layer), thereby allowing remaining Si to react with the oxygen after the main reaction with the SP.

Parimi *et al.*(59) studied the reactivity of various pSi EM's using DSC and TGA, investigating the influence of doping type and doping concentration of the original Si wafer. Wafer dopant concentration and type influenced the reactivity of the material, not directly by contributing to the reaction between the pSi and the oxidising agent, but indirectly by impacting on the morphology and specific surface area of the pSi generated by means of anodisation. Studying the propagation of the flame through pSi EMs of different morphology(57), the authors observed that the peak temperature of the first and strongest exotherm (which was attributed to the solid phase reaction between pSi and SP) shifted to lower temperatures as the specific surface area of the pSi increased, from approximately 400 °C at a surface area of 284 m².g⁻¹ to approx. 280 °C at a surface area of 730 m².g⁻¹. A calculation of the activation energies for these two materials gave values of 124.5 kJ.mol⁻¹ for the low surface area pSi and 72.1 kJ.mol⁻¹ for the high surface area pSi. From those calculations and others, it was determined that the propagation of the flame through pSi was due to a combination of both conductive and convective burning, not simply a conductive mechanism as observed in other solid-phase energetic materials.

Infrared spectroscopy is a versatile technique often applied to pSi research due to the wealth of information available about the chemical structure of this high surface area material.

Oxidation of a pSi surface heated continuously in an O₂ atmosphere was observed by Mawhinney *et al.*(134) with the results showing that the reaction proceeded initially by insertion of oxygen into the Si-Si bonds behind the Si-H surface species when the temperature exceeded 300 °C. As the oxidation proceeded, the hydride species were gradually replaced by hydroxyl groups and eventually, the surface was completely oxidised. Likewise, Salonen *et al.*(86) used FTIR in combination with DSC, showing a strong exothermic reaction of pSi heated in air commencing at about 200 °C, peaking at approximately 300 °C and attributed this to back bond oxidation of the pSi surface. Furthermore, a broad exothermic tail observed in the DSC rising from about 400 °C and terminating at approx. 650 °C was attributed to the formation of surface hydroxyl groups. However, in their study Salonen *et al.* (86) cooled the samples after heating, prior to FTIR analysis.

Both DSC and FTIR studies independently yield valuable information about the structure of pSi and the possible reaction pathways. Significantly, Mawhinney *et al.* (134) recognised the need to continuously record spectra during the heating process to minimise kinetic effects caused by cooling of a heated sample prior to measurement. Such problems would be exacerbated for the fast reacting pSi EM's studied here. It is therefore the aim of this work to combine these two techniques to obtain valuable real-time spectroscopic information regarding the reaction of pSi, and to correlate that to observed reactions in the thermal analysis.

6.2 Materials and methods

6.2.1 Porous silicon preparation

pSi was prepared using the standard method (Section 2.1), etching samples (15 mm etched area, 1.76 cm²) for 180 duty cycles (30 mins of applied current) at a current density of 45 mA.cm⁻² in 20% HF / ACN electrolyte. Previous work (Section 3.3) has determined that these etching conditions produce pSi surfaces with pore diameters of 3.5 ± 1.7 nm, a porosity of 64.7 ± 0.5%, and thickness of 49.9 μm. These wafers were cut into suitably sized smaller samples (approximately 4 x 4 mm² for DSC experiments and approximately 4 x 8 mm² for FTIR experiments) prior to loading with the oxidising agent.

Energetic pSi was created by loading with either SP (400 g.L⁻¹ in MeOH) or PFPE (200 g.L⁻¹ in FC-75), adding 5 μL of solution to the surface evaporating the solvent to deposit the oxidising agent into the pores as normal. Again, precipitation of the SP on the exterior face of the sample was problematic, requiring surface precipitates to be removed with a soft cotton swab prior to analysis.

The NEQ for each sample was determined gravimetrically. Samples were weighed prior and subsequent to loading with the oxidising agent, and the unreactive supporting wafer was weighed subsequent to analysis once the pSi layer had been stripped away using dilute aqueous potassium hydroxide. Samples for analysis typically had a NEQ in the range of 1 to 3 mg.

6.2.2 Thermal analysis

DSC experiments were conducted on a TA Instruments 8020 DSC at a heating rate of $20\text{ }^{\circ}\text{C min}^{-1}$, in open aluminium pans with a chamber purge gas of either dry air (BOC Instrument grade compressed air, $<25\text{ ppm H}_2\text{O}$ (135)) or N_2 at a rate of 50 mL min^{-1} , between ambient and $600\text{ }^{\circ}\text{C}$.

Thermogravimetric analysis (TGA) which would have simultaneously recorded mass changes in the system under analysis was unfortunately unsuitable for use here. This is due to the ceramic sample pans used with the available equipment which would have posed an unacceptable safety risk through friction initiation of pSi loaded with SP.

6.2.3 Spectroscopic analysis

FTIR experiments were conducted separately to the DSC, conducted on samples prepared and loaded under the same conditions, and under the same heating and atmospheric regime. The instrument used was a Nicolet Nexus 870 FTIR using a liquid N_2 cooled MCT detector and 16 scans per measurement point. Samples were heated by conduction on a Linkam FTIR600 hot stage accessory (Figure 6-1), heated at rate of $20\text{ }^{\circ}\text{C min}^{-1}$, with transmission spectra collected between 30 and $510\text{ }^{\circ}\text{C}$ at intervals of approximately $20\text{ }^{\circ}\text{C}$. This was also run with controlled atmospheres of either N_2 or dried air (supplied through a Parker Bailish purge gas generator), and used zinc selenide IR transparent windows. Spectra were all recorded in transmission mode at pre-determined temperatures as the sample was being continuously

heated. The temperature of the sample increased by approximately 2 °C during the time taken to actually record the spectra. Whilst it is recognised that this temperature change introduced a small uncertainty, it was felt that this was an acceptably necessary experimental compromise.

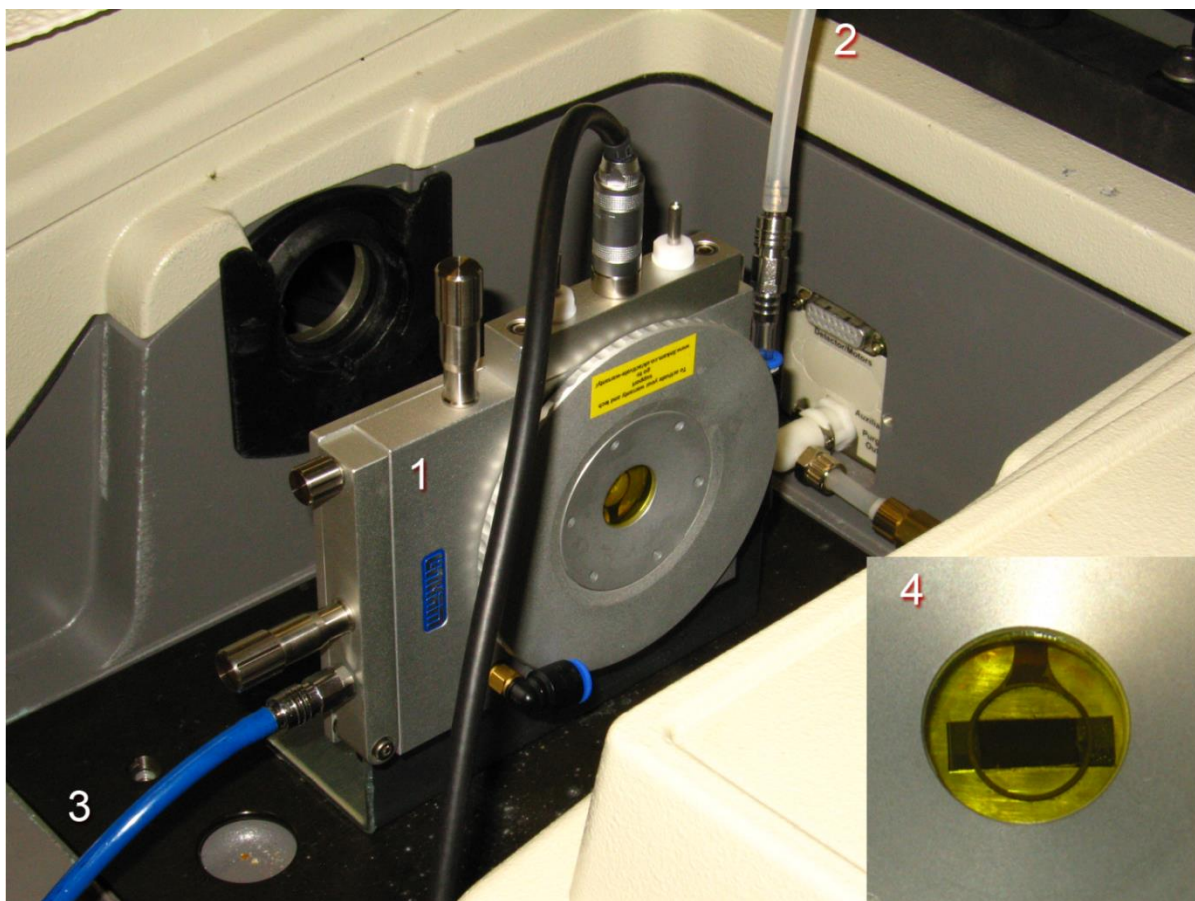


Figure 6-1: Linkam FTIR600 hot stage accessory (1) installed within the FTIR instrument, also depicting the purge gas inlet (2) and outlet (3), with a sample of pSi clamped against the heating element (4, inset).

Table 6-1 lists the characteristic spectral peaks for various species involved in this investigation.

Table 6-1: Characteristic frequencies of relevant transitions of species encountered during this study.

Wavenumber (cm ⁻¹)	Transition	Ref.
616, 621, 643	ClO ₄ ⁻ vibration	(136)
615, 622, 666	Si-H _x deformation, overlapped with Si crystal modes	(134)
671, 730, 776	C-C / C-O / C-F / C-F ₂ / C-F ₃ stretch	(96)
840	Si-N asymmetric stretch (>800 °C)	(137)
841, 877	O-SiH _x (unknown mode)	(134)
906	ClO ₄ ⁻ vibration	(136)
915	Si-H ₂ scissoring	(134)
940	Si-F stretch	(138)
950-1250 (broad)	Amorphous Si-O ₂ absorbance	(134)
980	Overlapping C-C / C-F ₂ / C-F ₃ stretch	(96)
1011, 1127, 1192	ClO ₄ ⁻ vibration	(136)
1015, 1121	Si-O-Si vibration	(134)
1029, 1190, 1826	Si-F ₄ (unknown mode)	(139)
1108	Si-O-Si crystal stretch	(134)
1110	ClO ₄ ⁻ vibration	(136)
1131 – 1345	Multiple overlapping C-C / CF ₂ / CF ₃ stretch	(96)
1157	C-F ₃ (unknown mode)	(139)
1200	C-F stretch	(140)
1283, 1539, 2186, 2561	C-F ₄ (unknown mode)	(139)
1300 - 1150	C-O-C; C-F stretch	(140)
1372	Overlapping C-C / CF ₂ / CF ₃ stretch	(96)
1929	COF ₂ (unknown mode)	(139)
2090, 2115, 2141	Si-H _x stretch	(134)
2214, 2273	OSi-H _x stretch	(134)
3736	SiO-H stretch	(134)
3745	SiO-H stretch	(134)
3750 - 4250	H-F stretch	(139)

It is known that the IR transmission of crystalline Si decreases with increasing temperature due to increases in lattice vibrations within the crystal structure (128). Accordingly, background spectra of an unetched Si wafer were collected at the same temperature intervals as the sample temperatures (within ≈ 2 °C) – Figure 6-2 displays a selection of elevated temperature background spectra indicating the decrease in transmission across the entire

spectral range under investigation. All raw data from individual experimental samples were then recalculated to yield a sample spectrum corrected for the decreased Si wafer transmission at the corresponding temperature.

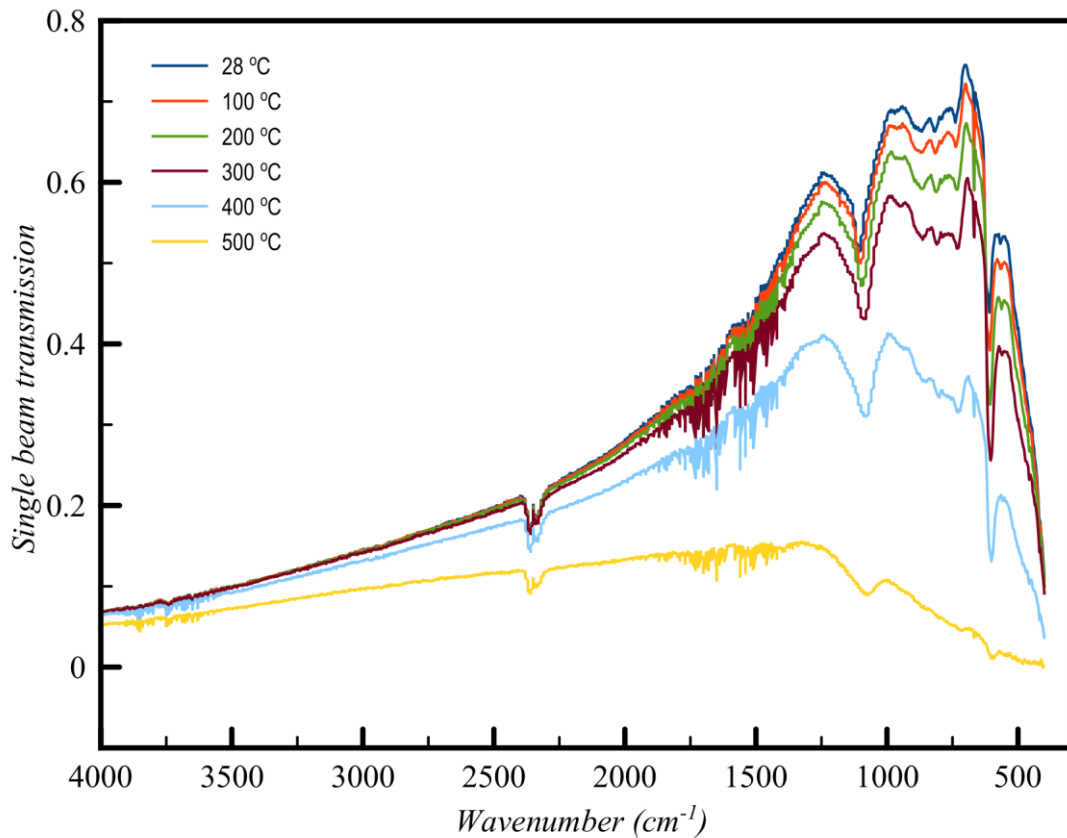


Figure 6-2: Background single beam transmission spectra for unetched Si wafers at elevated temperatures.

6.3 Results and discussion

DSC scans obtained for the various samples used in this study are shown in Figure 6-3. Each scan has been offset to allow comparison between the different samples. For the same samples, 2D images showing FTIR spectra as a function of temperature are compiled in Figure 6-4. Figure 6-5 depicts FTIR spectra (extracted from data forming Figure 6-4)

recorded at 150 °C to allow comparison of each of the material combinations and to highlight the relevant peaks. Each of the eight sample conditions are compared in further detail and presented in Appendix B.

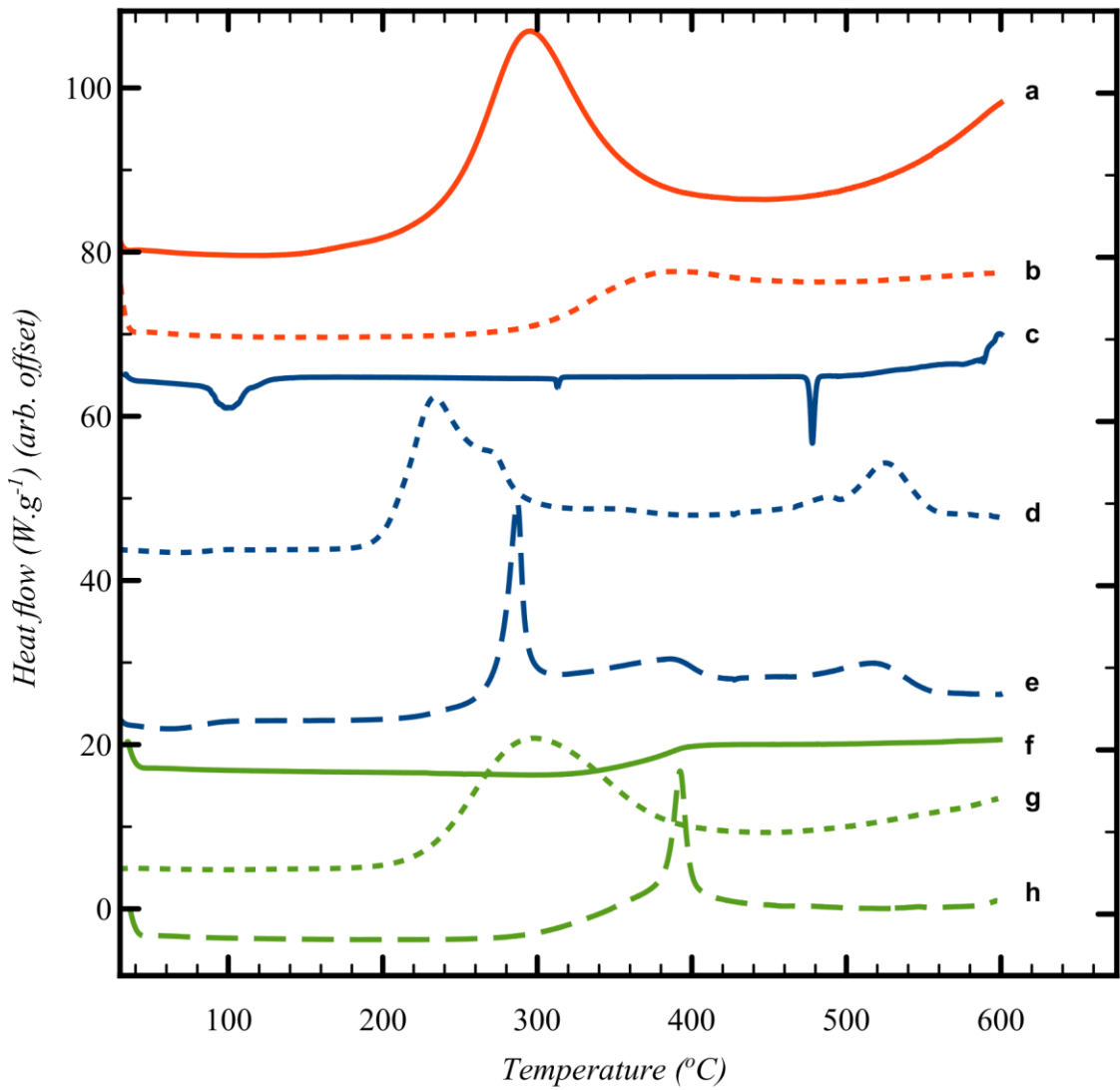


Figure 6-3: DSC scans of a) blank pSi in air, b) blank pSi in N₂, c) blank SP in air, d) pSi / SP EM in air, e) pSi / SP EM in N₂, f) blank PFPE in air, g) pSi / PFPE EM in air, and h) pSi / PFPE in N₂.

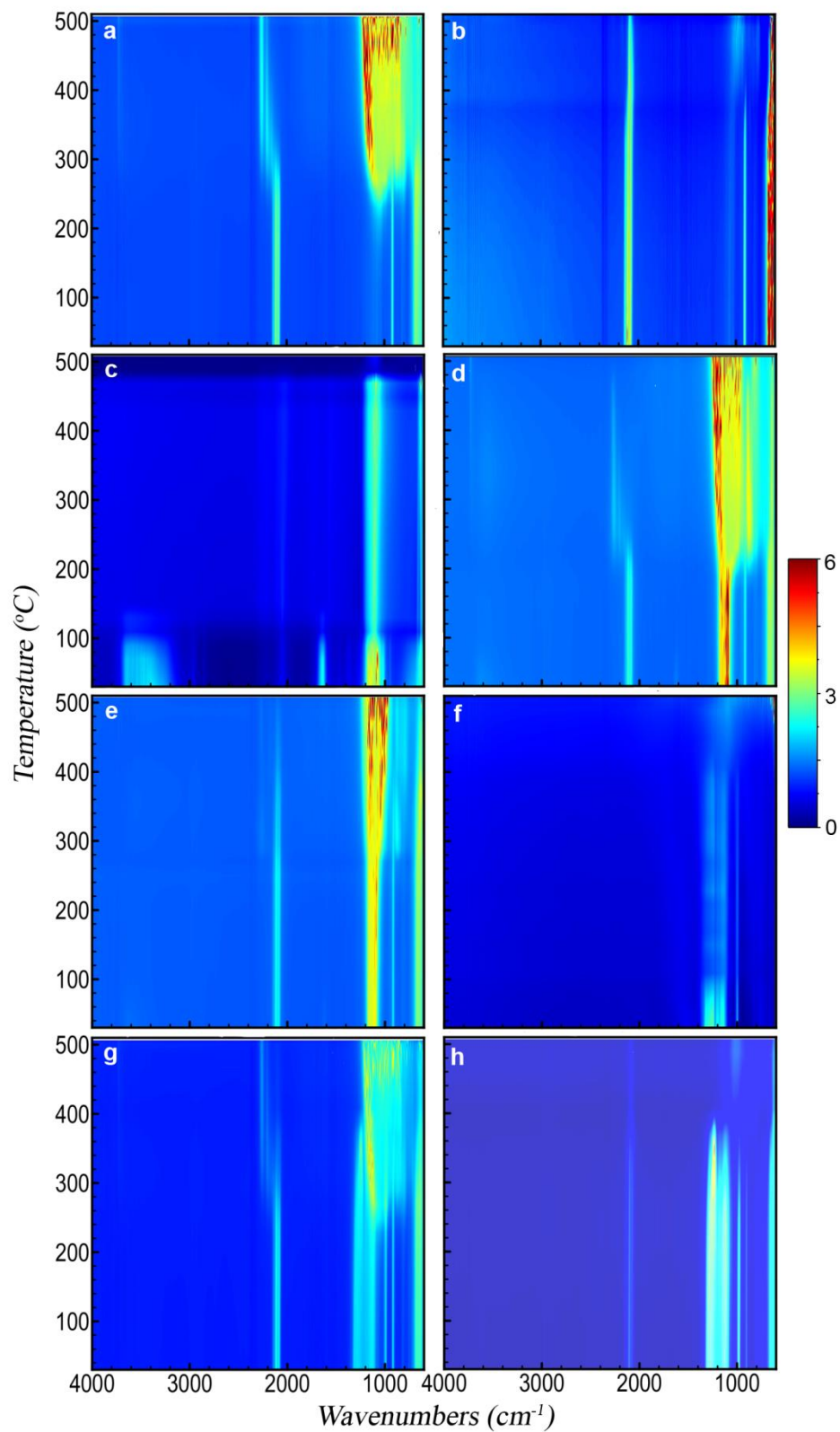


Figure 6-4: 2D FTIR spectra as a function of temperature of a) blank pSi in air, b) blank pSi in N₂, c) blank SP in air, d) pSi / SP EM in air, e) pSi / SP EM in N₂, f) blank PFPE in air, g) pSi / PFPE EM in air, and h) pSi / PFPE in N₂.

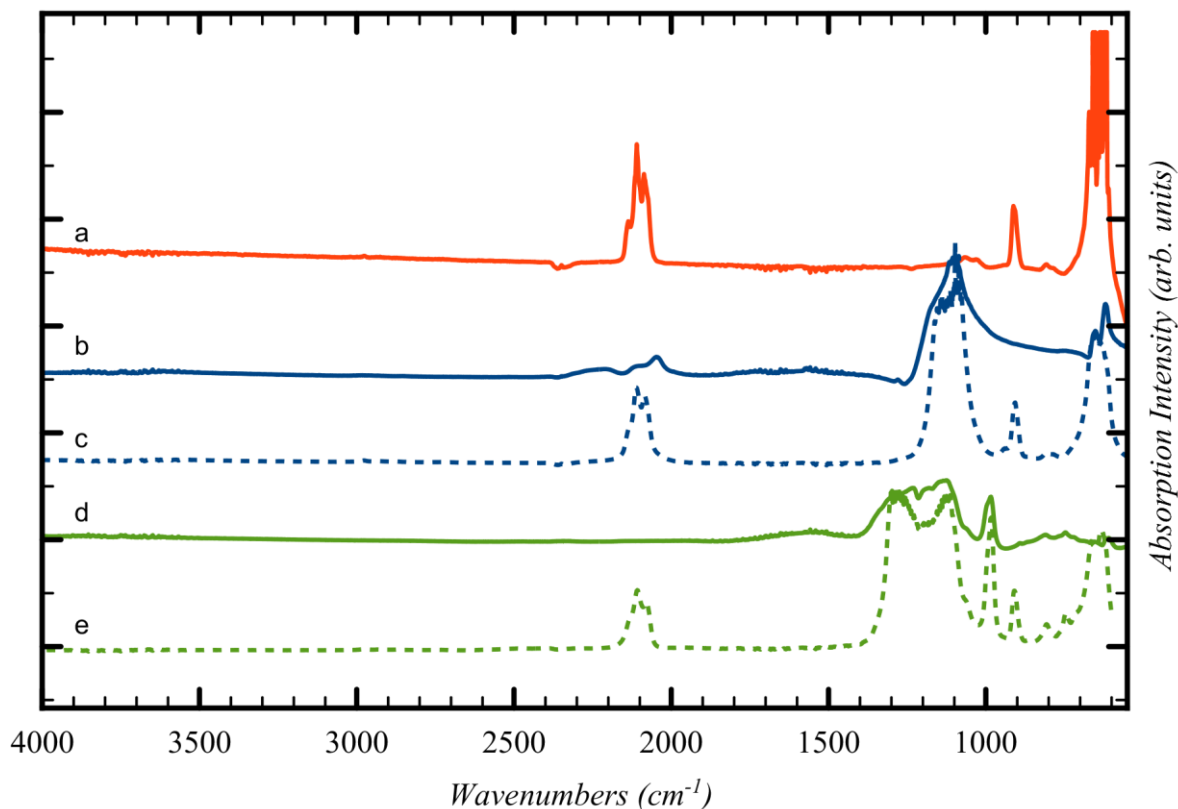


Figure 6-5: FTIR spectra of a) blank pSi, b) blank SP, c) pSi / SP EM, d) blank PFPE, and e) pSi / PFPE EM, collected at 150 °C for samples heated in a N₂ atmosphere. The triplet of peaks at $\approx 2109\text{ cm}^{-1}$ (Si-H_x vibration) and a single peak at $\approx 910\text{ cm}^{-1}$ (Si-H₂ scissoring) are specific for the pSi surface and clearly distinguished from a strong absorption band between ≈ 1000 and 1200 cm^{-1} (associated to multiple perchlorate vibration modes) and a sharp absorption peak at $\approx 980\text{ cm}^{-1}$ attributed to overlapping PFPE CF₂ / CF₃ vibrations.

6.3.1 Thermal behaviour of blank pSi

Unloaded pSi displayed significant evidence of oxidation when heated in air (Figures Figure 6-3a and Figure 6-4a). By means of DSC, we observed an onset temperature of the exothermic oxidation reaction at approximately 200 °C peaking at 292 °C. Comparing this to the FTIR spectral data, the main transition between a fresh and oxidised surface was initially visible at between 230 and 250 °C and appeared substantially complete by approximately 350 °C. This is most clearly indicated by the decrease in intensity of the surface hydride triplet peaks (centred at 2109 cm^{-1}) with an associated increase in the back-bonded oxygen (OSi-H_x)

represented by the peaks at $\approx 2254 \text{ cm}^{-1}$, and is supported by a very strong absorbing band between $\approx 800 - 1200 \text{ cm}^{-1}$ (amorphous Si-O₂ absorbance) and a weak peak at 3730 cm^{-1} (SiO-H stretch). These observations agree reasonably well with those of Salonen *et al.*(86).

However, for pSi heated in N₂ (Figure 6-3b and Figure 6-4b), the DSC showed a weak exothermic peak with an onset from approximately 270 °C and peaking at approximately 380 °C. FTIR spectra displayed the typical triplet of peaks at 2109 cm^{-1} associated with multiple Si-H_x stretching reducing gradually to a single peak centred at 2082 cm^{-1} between 350 – 400 °C. The onset temperature of this transition observed on the FTIR spectra ($\approx 350 \text{ °C}$) was higher than observed on the DSC ($\approx 270 \text{ °C}$), however the FTIR resolution may prevent subtle changes from being observed at lower temperatures. Subsequent to publication of these results (141), Sinha *et al.* (108) confirmed this observation by using TGA coupled with mass spectrometry to directly observe H₂ evolution from a pSi surface commencing at 280 °C.

Similarly, the peak at 910 cm^{-1} (Si-H₂ scissoring) decreased over the temperature range tested, disappearing completely by $\approx 400 \text{ °C}$. It seems that pSi heated in N₂ simply desorbs the surface hydrogen slowly commencing at $\approx 270 \text{ °C}$. By the end of the experimental run at 503 °C the hydride peaks still had not completely disappeared, and the absence of gaseous oxygen prevents further oxidation of the surface. A very weak peak at 850 cm^{-1} appears at 389 °C and increases intensity with temperatures up to 468 °C. This peak may be attributed to incorporation of nitride species on the Si surface based on the study by Scardera *et al.* (137). However, their study was conducted on samples of thin silicon nitride films at deposited at

400 °C and annealed to over 800 °C, and revealed multiple fine peaks centred around 840 cm⁻¹ that were assigned to modes of Si-N_x asymmetric stretching depending on the annealing temperature. Thus, we tentatively assign our observed peak at 850 cm⁻¹ to surface nitride species.

6.3.2 Decomposition and reaction of pSi / SP energetic materials

The FTIR spectra for SP as a function of temperature in air (Figure 6-4c) showed initial strong absorption bands between 1050 – 1200, 1600 – 1700 and 3100 – 3700 cm⁻¹ which disappeared at temperatures between 110 and 130 °C. A first moderate endothermic peak was seen in the DSC scans (Figure 6-3c) at approximately 100 °C. This peak was attributed to dehydration of the NaClO₄·H₂O, and the FTIR spectra appeared to reflect this change. Peaks at 619 and 1108 cm⁻¹ associated with various vibrations of the perchlorate ion were persistently observed. A weak peak at 2046 cm⁻¹ was stable across the temperature range is also associated with SP. In the DSC scan, a second weak endothermic peak at 313 °C was attributed to a phase change of the SP – this was not observed in the FTIR spectra. Sample melting occurred at 477 °C according to the DSC and FTIR. The combined thermal and spectroscopic data presented here agree well with previous work (*136, 142*), even though both studies used the two analytical techniques in isolation.

When SP was incorporated into the pSi layer to create an EM, significant changes in the FTIR spectra were observed compared to blank pSi and pure SP (Figure 6-4a and c). Initially, the strong absorption band centred at 1108 cm⁻¹ due to SP was clearly distinguishable from

relevant pSi peaks at 910 cm^{-1} and the triplet band at $\approx 2109\text{ cm}^{-1}$ for samples heated in either air or N_2 atmosphere (Figure 6-4d and e, and Figure 6-5c).

For pSi/ SP heated in air (Figure 6-3d and Figure 6-4d), the FTIR spectra displayed a clear transition commencing at approximately $200\text{ }^\circ\text{C}$ – this correlates with the onset temperature recorded in the DSC ($203\text{ }^\circ\text{C}$). This change was rapid and complete by approximately $250\text{ }^\circ\text{C}$ (with DSC recording a maximum at $233\text{ }^\circ\text{C}$). These changes are associated with strong oxidation of the pSi surface as evident from the disappearance of the Si-H_x triplet band and associated appearance of the OSi-H_x back bonding (approximately at 2254 cm^{-1}). The broad absorption band between $\approx 800\text{ -}1200\text{ cm}^{-1}$ was also attributed to Si-O_x vibrations. Changes in the perchlorate absorption peaks at $\approx 1100\text{ cm}^{-1}$ were masked at temperatures above $200\text{ }^\circ\text{C}$ due to broad Si-O_x absorption ($800\text{ -}1200\text{ cm}^{-1}$). These changes occurred at a temperature far lower than the melting point of SP ($477\text{ }^\circ\text{C}$) and its associated thermal decomposition. As suggested by Churaman *et al.*(51), this may include release of volatile O and OH radical species from decomposition of the perchlorate which may then interact with either of the two solid phase materials present, leading to a sustained reaction.

In a N_2 atmosphere (Figure 6-3e and Figure 6-4e), energetic pSi / SP displayed a similar sudden change in the FTIR spectra with an onset of approximately $270\text{ }^\circ\text{C}$, $70\text{ }^\circ\text{C}$ higher than in the presence of air. This correlated with an exothermic reaction observed by means of DSC commencing at around $270\text{ }^\circ\text{C}$ with a sharp peak at $300\text{ }^\circ\text{C}$. DSC and FTIR results for blank pSi in N_2 (Figure 6-3b and Figure 6-4b) indicate that the surface hydride desorption commences at approximately $270\text{ }^\circ\text{C}$, and this desorption appears to be an important first step

leading to commencement of the energetic reaction, in the absence of oxygen. Becker *et al.* (46) reached the same conclusion. Again, these reactions occur at a temperature lower than the melting point or decomposition point of the SP.

An additional observation recorded on the DSC scans of EM's run in air (Figure 6-3d and Figure 6-4d) is a shoulder in the main exothermic peak at 272 °C, a feature not observed in the samples in N₂ (Figure 6-3e and Figure 6-4e). This shoulder may be further evidence of afterburning reactions of unreacted pSi with the atmospheric O₂ within the DSC, similar to the high speed video observations reported by Becker *et al.* (98). Afterburning reactions are common in fuel-rich samples which is a possibility with the smaller samples prepared in this study. As noted in the experimental section, loading of small samples of pSi was difficult due to precipitation of the SP on the exterior face of the wafer, leading to variability of the quantity and distribution of the SP within the pSi pores. Additionally, the porosity of the pSi in this investigation (65%) was slightly lower than the calculated ideal porosity required to achieve a stoichiometrically balanced mixture (70-72%)(84), indicating that the system investigated here was fuel rich, thereby facilitating afterburning reactions.

6.3.3 Decomposition and reaction of pSi / PFPE energetic materials

Pure PFPE heated in air (Figure 6-3f and Figure 6-4f) displayed a strong and consistent peak at about 985 cm⁻¹, attributed to C-F bond stretching vibrations (96). Strong broad absorption bands centred at ≈1200 cm⁻¹, and a weak band centred at ≈ 744 cm⁻¹ correspond to multiple C-C / C-O / C-F vibrations (96). These bands persisted until approximately 400 °C when they

disappeared and were replaced by a weaker broad absorption centred at 1050 cm^{-1} . DSC scans of PFPE indicate a very weak change in the baseline commencing at $\approx 320\text{ }^{\circ}\text{C}$ and complete by $400\text{ }^{\circ}\text{C}$. In the DSC, it was noted that the aluminium pan was heavily tarnished after the acquisition of the scans of the PFPE samples were analysed (pans for other samples were not affected in this way), indicating that the sample was pyrolysing at these temperatures, releasing various reactive / oxidative species (instead of simply boiling away) as seen in other fully fluorinated polymers (93).

The FTIR scans of pSi / PFPE EM heated in air (Figure 6-3g and Figure 6-4g) were almost indistinguishable from the appearance of blank pSi in air except for the presence of the PFPE peak at 985 cm^{-1} and the band at 1200 cm^{-1} . Oxidation of the pSi surface due to the oxygen in the air was evident at the same transition temperature of approximately $250\text{ }^{\circ}\text{C}$ but appeared less intense compared to the spectra of blank pSi heated in air. In accordance with this observation, the DSC results of pSi / PFPE in air showed the same exothermic process as blank pSi in air but with a broader transition. No clear exotherms were observed to indicate an energetic reaction. One possible explanation for this is that the presence of the PFPE within the pores limits the rate of diffusion of oxygen into the surface such that the pSi reacts slowly with O_2 prior to pyrolysis of the PFPE.

In contrast, pSi / PFPE EM in N_2 displayed a different profile (Figure 6-3h and Figure 6-4h). The typical pSi peaks ($910, 2213\text{ cm}^{-1}$) and PFPE peaks and bands ($985\text{ \& } 1200\text{ cm}^{-1}$) were present and persisted until above $350\text{ }^{\circ}\text{C}$. The strong exothermic transition observed in the DSC occurring at $397\text{ }^{\circ}\text{C}$ correlated with the loss of most of the PFPE peaks in the FTIR

spectra from 390 °C onwards and also strongly attenuated pSi hydride peaks centred at 910 and 2213 cm^{-1} . Simultaneously, a peak at 1029 cm^{-1} (very weak prior to the transition) increased, potentially indicating production of SiF_4 . Some remnants of the pSi surface were seen in the FTIR spectra above this temperature and may be due to the presence of unreacted pSi left after all of the PFPE has been consumed. The peak at 1029 cm^{-1} was the only indication of a reaction product (SiF_4). Alternative species (such as HF at 3750-4250 cm^{-1}) were not observed.

When the pSi / PFPE results are compared to the pSi / SP heated in N_2 it is apparent that the energetic reaction occurred at a far higher temperature (≈ 400 °C for PFPE compared to 300 °C for SP). For pSi / SP, it was concluded that desorption of the surface hydride from the pSi was the initial step in the energetic reaction. For pSi / PFPE, it appears that the reaction did not occur even above the temperature required to commence hydride desorption, but was delayed until pyrolysis of the PFPE occurred at about 400 °C. Release of oxidising species from the PFPE during pyrolysis appears to be necessary to induce the energetic reaction. This mechanism is very similar to the reaction of other perfluorocarbon-based energetic materials (93).

6.4 Conclusions

Energetic materials based on pSi have the potential to be deployed in advanced integrated initiation systems and micro-electromechanical actuator systems (84), yet real world applications are currently limited due to the extreme sensitivity of the material and

uncertainty over the manner in which they react. Knowledge of the reaction mechanism may pave the way towards materials with fit-for-purpose sensitivity and performance. In an effort to further investigate the mechanism of reaction between pSi and two selected oxidising agents, thermal and spectroscopic methods were combined for the first time to yield more comprehensive information than use of either technique in isolation.

It was observed that breaking of the Si-Si back bonds behind the hydride surface upon reaction with atmospheric oxygen was sufficient to permit the SP to attack the surface and commence the energetic reaction. However, in the absence of oxygen, desorption of the hydride species from the pSi surface was a necessary step to initiate reaction of the pSi with SP. Turning attention to pSi loaded with PFPE, the pSi surface was oxidised in an air atmosphere before having the opportunity to react with PFPE. Yet in a N₂ atmosphere, the reaction between pSi and PFPE was delayed until the onset of pyrolysis of the PFPE. Heating a sample slowly under these controlled conditions is a departure from the normal mode of the explosive reaction of these materials, but the information gained in this way provides important insights into the earliest stages of the reaction.

Whereas the work presented in this Chapter (published in (141)) examined only the earliest stages of the reaction, Sinha *et al.* (108) later confirmed these results through a combination of DSC, 1D FTIR and TGA/MS. However, they extended their studies to examine accelerated ageing of pSi loaded with SP, finding that by heating samples at elevated temperatures between 185 and 300 °C, and recording the time at which samples lost the ability to react

energetically, pSi / SP energetic materials had a predicted mean lifetime to failure of 100 years if stored at 25 °C.

Chapter 7 CONCLUSIONS

The behaviour of porous silicon energetic materials was investigated to gain an understanding of their fundamental behaviour, properties, limits and potential. pSi, fabricated by electrochemical etching of mildly doped p-type Si wafers were found to form highly branched pore structures with voids in the range of 3 – 5 nm. Loading of the surface with a variety of oxidising agents was achieved by making use of high volatility, low viscosity, carrier solvents. The small pore size coupled with moderately high porosity caused a very intimate mixture of the oxidising agent and the pSi fuel. Minor stimuli were sufficient to initiate the reaction which, while initially small, would cascade up to rapid explosive burning (deflagration).

Control over the burning rate could be most easily achieved through selection of etching parameters to influence the morphology of the surface. Weak deflagrations were achieved at layer thicknesses as low as $\approx 4 \mu\text{m}$, accelerating rapidly to strong deflagrations approaching 200 m.s^{-1} at layer thicknesses of $50 \mu\text{m}$ or more. Confining the sample during ignition consistently doubled the burning rate, achieving top speeds of $\approx 500 \text{ m.s}^{-1}$. The nature of the burning was quite erratic, with internal pressure within the sample believed to cause fissures through which the flame would accelerate suddenly and unpredictably. However, throughout this work there was no evidence that the material was undergoing a detonation, in spite of the strength of the deflagration observed.

SP was characterised as being the strongest oxidising agent investigated, although various nitrate and perchlorate salts were found to be suitable. Interestingly, perfluorocarbons (specifically PFPE) were affirmed as being suitable oxidants in this system, displaying

markedly different behaviours which may prove useful if the material is to find real-world applications.

pSi based on SP is exceedingly sensitive, initiating with the slightest disruption of the hydride terminated surface, requiring it to be handled with the care often reserved for primary explosives. Introduction of PFPE reduced the sensitiveness somewhat, eliminating a propensity for ignition by friction, but unfortunately maintaining a high sensitiveness to ignition by confined impact.

Correlated DSC and 2D FTIR confirmed prevailing theories that the hydride terminated pSi surface afforded protection to the surface, preventing reaction with the SP. Disruption of the surface by thermally induced bond rupturing (either due to atmospheric oxidation of the surface, or loss of the protective hydride layer) was the causal factor inducing the energetic reaction. However, the inherent stability of the PFPE tended to prevent the energetic reaction even when reactive pSi bonds became available, and was delayed until pyrolysis of the fluoropolymer at temperatures approaching 400 °C. These two different reaction initiation paths tend to explain the differing sensitiveness of these two pSi variants.

The extreme sensitiveness of the material was reinforced when it was determined that weak elastic waves caused by a laser generated shockwave were sufficient to initiate pSi / SP mixtures. However, one of the most intriguing outcomes from this work was the discovery that the transparency of Si in the infrared region could be exploited and the material can be

initiated by shining the laser through the back of the otherwise opaque substrate, leading to potential safety advantages through electrical isolation of the material from the initiation source.

7.1 Future directions and opportunities

Whereas much has been discovered about the behaviour of pSi energetic materials throughout this project and through work by others in this field, there are still significant problems which will hamper widespread introduction of the material in commercial applications. The extreme sensitiveness of the material to initiation, coupled with the inherent brittleness of Si, means that devices which incorporate pSi energetic materials would likely be unsuitable for deployment due to the risk of initiation through mishandling. Whereas SP has dominated the research, an optimum balance between explosive performance and acceptable sensitiveness may be revealed through a wider survey of alternative oxidising agents, potentially identifying candidates that could actually be suitable for real-world applications.

The long term stability of pSi energetic materials remains doubtful. pSi / SP mixtures are highly hygroscopic and will readily degrade in the presence of moisture, requiring fabricated devices of otherwise increased complexity in order to protect the energetic material. Recently Sinha *et al.* (108) examined the accelerated ageing of pSi / SP systems – while this was under highly idealised conditions, it did demonstrate that the system could potentially remain stable over a long period of time. This is the first and only published work of any stability tests for pSi based energetic materials. Extending this to other oxidising agents may identify

substances which demonstrate the required long term stability, yet do not suffer from the problems associated with hygroscopic SP. A more stable mixture that can be fabricated into devices without complex protective barriers, even at the expense of reduced burning rates, may be more viable than the more energetic pSi / SP system.

Interestingly, with the exception of the investigated fluoropolymers, there are no reports in the literature of non-traditional oxidising agents having been applied to these systems. Two major possibilities for future research exist here. Firstly, energetic materials which are themselves oxidising or have a very high oxygen content, such as ammonium dinitramide (ADN, Figure 7-1a) (143) or CL-20 (2,4,6,8,10,12-Hexanitro-2,4,6,8,10,12-hexaazaisowurtzitane, Figure 7-1b) (143, 144), could be used as alternatives in these systems. Both of these are relatively stable substances, yet upon decomposition both release NO_2 oxidising species (133) able to react with the pSi. Both of these substances would also produce a high proportion of gaseous reaction products (e.g. N_2 , H_2O , CO_2 etc.), thereby improving the capability of the system to perform useful work compared to the substantially solid reaction products of the pSi / SP system (i.e. NaCl and SiO_2).

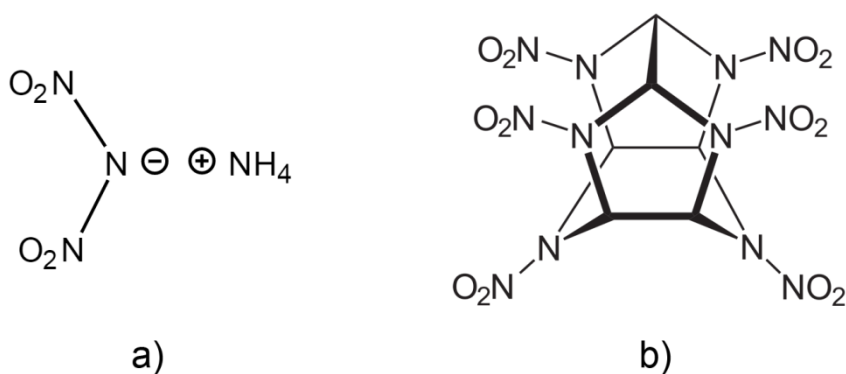


Figure 7-1: Structures of a) ammonium dinitramide and b) CL-20 energetic materials

The second possibility is the direct formation of a polymeric oxidising agent within the pore structure of pSi itself. PFPE was shown to be an effective alternative to SP as an oxidising agent, but the high viscosity liquid was difficult to infiltrate throughout the pore structure of even a thin layer of pSi. However, if the pore structure was completely filled with a low viscosity monomer for a fluoropolymer, with the polymerisation reaction carried out inside the pores, this would potentially alleviate the uneven distribution experienced by PFPE. Furthermore, if the conditions were chosen correctly to form a solid or elastomeric polymer within the pSi matrix, the material properties of the polymer may serve as structural reinforcement, enhancing the overall strength of the mixture. Such a solid composite pSi / fluoropolymer may be more resilient to mechanical damage, with the toughness of the polymer counteracting the brittleness of the pSi thereby improving the sensitiveness to impact compared to pSi / liquid PFPE.

The need to understand and predict the behaviour of these mixtures may be able to be answered through numerical modelling of these systems. As was noted by Parimi *et al.* (60), and supported by this Thesis, progress of the flame front through the pSi layer occurs predominately through conductive and convective heat transfer processes, however filling the narrow pores investigated here and elsewhere with oxidizing agent will tend to restrict flame permeation through the pSi layer. The combined efforts of du Plessis (15) (modelling of the pSi structure and relationship to SSA), Sinha *et al.* (108) (determination of pSi / SP reaction kinetics), Becker *et al.* (98) (measurement of reaction products of pSi / SP at various mole ratios) and the large body of work documenting the burning rate of pSi energetic materials

forms the basis for the necessary data to be used for numerical modelling of the behaviour of pSi energetic material systems. Such modelling would be expected to provide insights into the role of flame permeation through the pore network, the influence of the melting point and thermal conductivity for different oxidising agents, and potential for work output, all in a manner which could help to optimise the system.

BIBLIOGRAPHY

1. Cullis, A. G., Canham, L. T., and Calcott, P. D. J. (1997) The structural and luminescence properties of porous silicon, *Journal of Applied Physics* 82, pp909–965.
2. McCord, P., Yau, S. L., and Bard, A. J. (1992) Chemiluminescence of anodized and etched silicon: Evidence for a luminescent siloxene-like layer on porous silicon, *Science* 267, pp68–69.
3. Foll, H., Christopherson, M., Cartensen, J., and Hasse, G. (2002) Formation and application of porous silicon, *Materials Science and Engineering R* 39, pp93–141.
4. Allongue, P. (1997) Porous silicon formation mechanisms, in *Properties of Porous Silicon* (Canham, L. T., Ed.), Institution of Electrical Engineers, London pp3–11.
5. Baranov, I. L., Tabulina, L. V., and Stanovaya, L. S. (2003) Specific features of porous silicon synthesis in aqueous-alcoholic etching solutions, *Russian Journal of Applied Chemistry* 76, pp932–935.
6. Chazalviel, J. N., and Ozanam, F. (2005) Ordered Porous Nanostructures and Applications (Wehrspohn, R. B., Ed.), pp15–35, Springer, New York.
7. Coffey, J. L. (1997) Porous silicon formation by stain etching, in *Properties of Porous Silicon* (Canham, L. T., Ed.), Institution of Electrical Engineers, pp23–29.
8. Goryachev, D. N., Belyakov, L. V., and Sreseli, O. M. (2000) On the mechanism of porous silicon formation, *Semiconductors* 34, pp1090–1093.
9. Grossman, A., and Ortega, C. (1997) Chemical composition of ‘fresh’ porous silicon, in *Properties of Porous Silicon* (Canham, L. T., Ed.), Institution of Electrical Engineers, pp144–153.
10. Halimaoui, A. (1997) Porous silicon formation by anodisation, in *Properties of Porous Silicon* (Canham, L. T., Ed.), Institution of Electrical Engineers, pp12–22.
11. Kang, C. G., Kang, M. S., Yang, J. H., Jin, J. H., Hong, S. I., and Min, N. K. (2003) Comparison of nano-porous silicon prepared by photoelectrochemical etching in HF-ethanol and HF-acetonitrile solutions, *Journal of the Korean Physical Society* 42, ppS693–S697.
12. Lee, Y., Lee, J., Suhl, Y., and Lim, S. (2008) Effect of wafer resistivity and HF concentration on the formation of vertically aligned porous silicon, *Journal of Industrial and Engineering Chemistry* 14, pp105–109.
13. Martin, P., Fernandez, J. F., and Sanchez, C. (2004) Hydrogen surface coverage of as-prepared nanocrystalline porous silicon, *Materials Science and Engineering B* 108, pp166–170.

14. Morita, M., Ohmi, T., Hasegawa, E., Kawakami, M., and Ohwada, M. (1990) Growth of a native oxide on a silicon surface, *Journal of Applied Physics* 68, pp1272–1281.
15. Plessis, M. du. (2007) Relationship between specific surface area and pore dimension of high porosity nanoporous silicon - model and experiment, *Physica Status Solidi A* 204, pp2319–2328.
16. Ronkel, F., and Schultze, J. W. (2000) Electrochemical aspects of porous silicon formation, *Journal of Porous Materials* 7, pp11–16.
17. Guendouz, M., Joubert, P., and Sarret, M. (2000) Effect of crystallographic directions on porous silicon formation on patterned substrates, *Materials Science and Engineering: B*, Elsevier 69, pp43–47.
18. Parkhutik, V. (1999) Porous silicon - mechanisms of growth and applications, *Solid State Electronics* 43, pp1121–1141.
19. Plessis, M. du, and Conradie, C. (2005) Nano-explosions in porous silicon. In *Microelectronics, MEMS, and Nanotechnology*, 60370X–60370X, International Society for Optics and Photonics.
20. Canham, L. T. (1997) Pore type, shape size, volume and surface area in porous silicon, in *Properties of Porous Silicon* (Canham, L. T., Ed.), 83–88, Institution of Electrical Engineers.
21. Bailey, A., and Murray, S. G. (1989) *Explosives, Propellants and Pyrotechnics*, p122, Maxwell Pergamon Publishing, London.
22. Piekielek, N. W., Morris, C. J., Churaman, W. A., Cunningham, M. E., Lunking, D. M., and Currano, L. J. (2015) Combustion and Material Characterization of Highly Tunable On-Chip Energetic Porous Silicon, *Propellants, Explosives, Pyrotechnics*, Wiley Online Library 40, pp16–26.
23. Lazaruk, S., Dolbik, A., Labunov, V., and Borisenko, V. (2007) Combustion and explosion of nanostructured silicon in microsystem devices, *Semiconductors*, Springer 41, pp1113–1116.
24. Koch, E.-C., and Clément, D. (2007) Special materials in pyrotechnics: VI. Silicon—an old fuel with new perspectives, *Propellants, Explosives, Pyrotechnics*, Wiley Online Library 32, pp205–212.
25. Suceca, M. (1995) *Test methods for Explosives*, pp1-10 and 91-165, Springer-Verlag, New York.
26. Lee, P. R. (2003) Explosives development and fundamentals of explosives technology, in *Explosive effects and applications* (Zukas, J. A., and Walters, W., Eds.), pp23–46, Springer.

27. Margolis, S. B. (1997) A deflagration analysis of porous energetic materials with two phase flow and multiphase sequential reaction mechanism, *Journal of Engineering Mathematics* 31, pp173–203.
28. Meyer, R., Kohler, J., and Homburg, A. (2002) Explosives 5th ed., p75, Wiley-VCH, Weinheim.
29. Zel'dovich, Y. B., and Raizer, Y. P. (2002) *Physics of Shock Waves and High Temperature Hydrodynamic Phenomena* (Hayes, W. D., and Probstein, R. F., Eds.), pp685-746, Dover Publications, New York.
30. Grigor'ev, V., Luk'yanchikov, L., Pruel, E., and Vasil'ev, A. (2001) Initiation of a porous explosive by overdriven gas detonation products, *Combustion, Explosion, and Shock Waves*, 37, pp572–579.
31. Hamate, Y., and Horie, Y. (2006) Ignition and detonation of solid explosives: a micromechanical burn model, *Shock Waves*, 16, pp125–147.
32. Lee, P. R. (2003) Theories and techniques of initiation, in *Explosive effects and applications* (Zukas, J., and Walters, W., Eds.), pp173-220, Springer.
33. Oxley, J. (2003) Explosive effects and applications, *Explosive effects and applications* (Zukas, J. A., and Walters, W., Eds.), pp137–172, Springer.
34. Pantoya, M. L., and Granier, J. J. (2005) Combustion behaviour of highly energetic thermites: nano versus micron composites, *Propellants, Explosives, Pyrotechnics* 30, pp53–62.
35. Lide, D. R. (1990) Handbook of Chemistry and Physics 71st ed., CRC Press, Boston.
36. Lu, J. P., Dorsett, H. E., Franson, M. D., and Cliff, M. D. (2003) Near-field performance evaluations of Alex effect in metallised explosives, DSTO-TR-1542, Defence Science and Technology Organisation, Edingburgh.
37. Clement, D., Diener, J., Gross, E., Künzner, N., Timoshenko, V. Y., and Kovalev, D. (2005) Highly explosive nanosilicon-based composite materials, *physica status solidi (a)*, 202, pp1357–1364.
38. Loni, A., Canham, L., Defforge, T., and Gautier, G. (2015) Supercritically-Dried Porous Silicon Powders with Surface Areas Exceeding 1000 m²/g, *ECS Journal of Solid State Science and Technology*, 4, ppP289–P292.
39. Kovalev, D., Timoshenko, V. Y., Künzner, N., Gross, E., and Koch, F. (2001) Strong explosive interaction of hydrogenated porous silicon with oxygen at cryogenic temperatures, *Physical Review Letters*, 87, p068301.
40. Mikulec, F. V., Kirtland, J. D., and Sailor, M. J. (2002) Explosive nanocrystalline porous silicon and its use in atomic emission spectroscopy, *Advanced Materials*, Wiley Online Library 14, pp38–41.

41. Lazarouk, S., Dolbik, A., Jaguiro, P., Labunov, V., and Borisenko, V. (2005) Fast exothermic processes in porous silicon, *Semiconductors*, Springer 39, pp881–883.
42. Dawson, R. (2007) Development and Characterization of Explosive Porous Silicon, Thesis, Flinders University of South Australia.
43. Abraham, A., Piekiet, N. W., Morris, C. J., and Dreizin, E. L. (2016) Combustion of Energetic Porous Silicon Composites Containing Different Oxidizers, *Propellants, Explosives, Pyrotechnics*, 41, pp179-181.
44. Becker, C., Currano, L., and Churaman, W. (2009) *Characterization and Improvements to Porous Silicon Processing for Nanoenergetics*, ART-TR-4717, Army Research Laboratory.
45. Becker, C. R., Apperson, S., Morris, C. J., Gangopadhyay, S., Currano, L. J., Churaman, W. A., and Stoldt, C. R. (2010) Galvanic porous silicon composites for high-velocity nanoenergetics, *Nano letters*, ACS Publications 11, pp803–807.
46. Becker, C. R., Currano, L. J., Churaman, W. A., and Stoldt, C. R. (2010) Thermal analysis of the exothermic reaction between galvanic porous silicon and sodium perchlorate, *ACS applied materials & interfaces*, ACS Publications 2, pp2998–3003.
47. Bezuidenhout, H. C., and Mukhopadhyay, S. (2013) High temperature reaction behaviour of nanoporous silicon based explosive formulations, *International Journal of Basic and Applied Sciences*, Science Publishing Corporation 2, pp381-386.
48. Churaman, W. A., Becker, C. R., Metcalfe, G. D., Hanrahan, B. M., Currano, L. J., and Stoldt, C. R. (2010) Optical initiation of nanoporous energetic silicon for safing and arming technologies, in *Proc. Of SPIE 7795, Optical technologies for arming, safing, fuzing and firing IV*, pp779506–779506, International Society for Optics and Photonics.
49. Churaman, W., Currano, L., and Becker, C. (2010) Initiation and reaction tuning of nanoporous energetic silicon, *Journal of Physics and Chemistry of Solids*, 71, pp69–74.
50. Churaman, W., Currano, L., Dubey, M., and Becker, C. (2008) *Fabrication and Characterization of Nanoporous Energetic Silicon*, Army Research Laboratory.
51. Churaman, W., Currano, L., Singh, A. K., Rai, U. S., Dubey, M., Amirtharaj, P., and Ray, P. C. (2008) Understanding the energetic behaviours of nano-energetic porous silicon, *Chemical Physics Letters* 464, pp198–201.
52. Currano, L., Churaman, W., and Becker, C. (2009) Nanoporous silicon as a bulk energetic material. In *Solid-State Sensors, Actuators and Microsystems Conference, Transducers Denver Colorado 2009*, pp2172–2175, IEEE.
53. Currano, L. J., and Churaman, W. A. (2009) Energetic nanoporous silicon devices, *Journal of Microelectromechanical Systems*, 18, pp799–807, IEEE.

54. Morris, C. J., Laflin, K. E., Churaman, W. A., Becker, C. R., Currano, L. J., and Gracias, D. H. (2012) Initiation of nanoporous energetic silicon by optically-triggered, residual stress powered microactuators, in *IEEE 25th International Conference on Micro Electro Mechanical Systems (MEMS), 2012*, pp1245–1248, IEEE.
55. Nguyen, V. C., Pita, K., Kam, C. H., Dolbik, A., Lazarouk, S., and Labunov, V. (2015) Giant and tunable mechanical impulse of energetic nanocrystalline porous silicon, *Journal of Propulsion and Power* 31, pp694–698.
56. Ohkura, Y., Weisse, J. M., Cai, L., and Zheng, X. (2013) Flash ignition of freestanding porous silicon films: effects of film thickness and porosity, *Nano letters*, ACS Publications 13, pp5528–5533.
57. Parimi, V. S., Lozda, A. B., Tadigadapa, S. A., and Yetter, R. A. (2014) Reactive wave propagation in energetic porous silicon composites, *Combustion and Flame* 161, pp2991–2999.
58. Parimi, V. S., Tadigadapa, S. A., and Yetter, R. A. (2015) Reactive wave propagation mechanisms in energetic porous silicon composites, *Combustion Science and Technology*, Taylor & Francis 187, pp249–268.
59. Parimi, V. S., Tadigadapa, S. A., and Yetter, R. A. (2014) Effect of substrate doping on microstructure and reactivity of porous silicon, *Chemical Physics Letters*, 609, pp129–133.
60. Parimi, V. S., Tadigadapa, S. A., and Yetter, R. A. (2012) Control of nanoenergetics through organized microstructures, *Journal of Micromechanics and Microengineering*, 22, p055011.
61. Piekiet, N. W., Churaman, W. A., Morris, C. J., and Currano, L. J. (2013) Combustion and material characterization of porous silicon nanoenergetics, in *IEEE 26th International Conference on Micro Electro Mechanical Systems (MEMS) 2013*, pp449–452, IEEE.
62. Piekiet, N. W., Morris, C. J., Currano, L. J., Lunking, D. M., Isaacson, B., and Churaman, W. A. (2014) Enhancement of on-chip combustion via nanoporous silicon microchannels, *Combustion and Flame*, Elsevier 161, pp1417–1424.
63. Plessis, M. du. (2009) Investigating nanoporous silicon explosive devices, *physica status solidi (c)*, Wiley Online Library 6, pp1763–1768.
64. Plessis, M. du. (2008) Nanoporous silicon explosive devices, *Materials Science and Engineering: B*, Elsevier 147, pp226–229.
65. Plessis, M. du. (2007) Properties of porous silicon nano-explosive devices, *Sensors and Actuators A: Physical*, Elsevier 135, pp666–674.
66. Son, S. F., and Mason, B. A. (2010) An Overview of Nanoscale Silicon Reactive Composites Applied to Microenergetics, in *48th AIAA Aerospace Sciences Meeting*,

including the New Horizons Forum and Aerospace Exposition, January 2010, Orlando Florida.

67. Son, S. F., Yetter, R. A., and Mukasyan, A. S. (2013) *Silicon-Based Nanoscale Composite Energetic Materials*, DTRA-TR-13-1, Defence Threat Reduction Agency.
68. Subramanian, S., Tiegs, T., Limaye, S., Kapoor, D., and Redner, P. (2008) *Nanoporous silicon based energetic materials*, DTIC Document.
69. Thiruvengadathan, R., Belarde, G. M., Bezmelnitsyn, A., Shub, M., Balas-Hummers, W., Gangopadhyay, K., and Gangopadhyay, S. (2012) Combustion Characteristics of Silicon-Based Nanoenergetic Formulations with Reduced Electrostatic Discharge Sensitivity, *Propellants, Explosives, Pyrotechnics*, Wiley Online Library 37, pp359–372.
70. Wang, S., Shen, R., Yang, C., Ye, Y., Hu, Y., and Li, C. (2013) Fabrication, characterization, and application in nanoenergetic materials of uncracked nano porous silicon thick films, *Applied Surface Science*, 265, pp4–9.
71. Wang, S., Shen, R., Ye, Y., and Hu, Y. (2012) An investigation into the fabrication and combustion performance of porous silicon nanoenergetic array chips, *Nanotechnology*, 23, pp435701-1 to 7.
72. Wang, S., Shen, R., Ye, Y., Hu, Y., Wu, L., and Yang, C. (2013) Investigation on combustion of porous silicon nanoenergetic chips ignited by single pulse laser, in *2nd International Symposium on Laser Interaction with Matter (LIMIS 2012)*, pp 87960C–87960C, International Society for Optics and Photonics.
73. Yarrington, C. D., Lothamer, B., Son, S. F., and Foley, T. J. (2009) Combustion Properties of Silicon/Teflon/Viton and Aluminum/Teflon/Viton Composites, in *47th AIAA Aerospace Sciences Meeting Including The New Horizons Forum and Aerospace Exposition, Orlando, FL, USA*.
74. Koch, E.-C. (2002) Metal-fluorocarbon-pyrolants: III. Development and application of Magnesium/Teflon/Viton (MTV), *Propellants Explosives Pyrotechnics* 27, pp262–266.
75. Rider, K. B., Little, B. K., Emery, S. B., and Lindsay, C. M. (2013) Thermal analysis of magnesium/perfluoropolyether pyrolants, *Propellants, Explosives, Pyrotechnics*, 38, pp433–440.
76. Mason, B. A., Son, S. F., Cho, K. Y., Yetter, R. A., and Asay, B. W. (2009) Combustion performance of porous silicon-based energetic composites, *45th AIAA/ASME/SAE/ASEE Joint Propulsion Conference & Exhibition. New York: AIAA* pp1–7.
77. Fastcam SA5 (2016) <http://photron.com/high-speed/cameras/fastcam-sa5/> Photron USA, accessed 01/09/2016.

78. Nguyen, V. C., Pita, K., Kam, C., Dolbik, A., Lazarouk, S., and Labunov, V. (2015) Giant and tunable mechanical impulse of energetic nanocrystalline porous silicon, *Journal of Propulsion and Power*, 31, pp694–698.
79. Terry, B. C., Lin, Y.-C., Manukyan, K. V., Mukasyan, A. S., Son, S. F., and Groven, L. J. (2014) The effect of silicon powder characteristics on the combustion of silicon/Teflon/Viton nanoenergetics, *Propellants, Explosives, Pyrotechnics*, 39, pp337–347.
80. Yarrington, C. D., Groven, L. J., Reeves, R. V., and Son, S. F. (2013) The effect of doping on the combustion and reaction kinetics of silicon reactives, *Combustion and Flame*, 160, pp1835–1841.
81. Bouchaour, M., Ould-Abbas, A., Diaf, N., and Sari, N. C. (2004) Effect of drying on porous silicon, *Journal of thermal analysis and calorimetry*, 76, pp677–684.
82. Kissinger, H. E. (1957) Reaction kinetics in differential thermal analysis, *Analytical chemistry*, 29, pp1702–1706.
83. White, A. (2002) *A review in some current research in micro-electromechanical systems (MEMS) with defence applications*, DSTO-GD-0316, Defence Science and Technology Organisation, Edinburgh.
84. Plessis, M. du. (2014) A Decade of Porous Silicon as Nano-Explosive Material, *Propellants, Explosives, Pyrotechnics*, 39, pp348–364.
85. Sailor, M., Mikulec, F., and Kirtland, J. (2004) *Porous silicon-based explosive*, US Patent Application US2004/0244889.
86. Salonen, J., Lehto, V.-P., and Laine, E. (1997) Thermal oxidation of free-standing porous silicon films, *Applied physics letters*, 70, pp637–639.
87. Roudit, N. (2006) JMicroVision: Image analysis toolbox for measuring and quantifying components of high-definition images, www.jmicrovision.com accessed 01/03/2017.
88. Escorcía, J., and Agarwal, V. (2007) Effect of duty cycle and frequency on the morphology of porous silicon formed by alternating square pulse anodic etching, *physica status solidi (c)*, 4, pp2039–2043.
89. Piercey, D. G., and Klapoetke, T. M. (2010) Nanoscale aluminum-metal oxide (thermite) reactions for application in energetic materials, *Central European Journal of Energetic Materials* 7, pp115–129.
90. Morales-Masis, M., Segura, L., and Ramírez-Porras, A. (2007) Correlation between Vickers microhardness, porous layer thickness and porosity in p-type nanostructured silicon, *Applied surface science*, 253, pp7188–7191.
91. Mason, B. A. (2010) *The combustion performance of nanosilicon based energetic materials*, Thesis, Purdue University.

92. Christo, F. C. (1999) *Thermochemistry and kinetics models for magnesium/Teflon/Viton pyrotechnic compositions*, DSTO-TR-0938, Defence Science and Technology Organisation, Edinburgh.
93. Koch, E.-C. (2012) *Metal-Fluorocarbon Based Energetic Materials*, Wiley-VCH, Weinheim, pp68-118.
94. *Fomblin PFPE Lubes for Vacuum Applications*, (2015), Solvay Specialty Polymers, http://www.solvay.com/en/binaries/Fomblin-PFPE-Lubes-for-Vacuum-Applications_EN-229544.pdf, accessed 09/10/2015.
95. Zhang, S.-L., Wang, X., Li, J., Diao, P., Cai, S., and others. (1994) Raman spectra in a broad frequency region of p- type porous silicon, *Journal of applied physics*, 76, pp3016–3019.
96. Pacansky, J., Miller, M., Hatton, W., Liu, B., and Scheiner, A. (1991) Study of the structure of perfluoro ethers: structural models for poly (perfluoroformaldehyde), poly (perfluoroethylene oxide) and poly (perfluoropropylene oxide), *Journal of the American Chemical Society*, 113, pp329–343.
97. Plummer, A., Kuznetsov, V., Joyner, T., Shapter, J., and Voelcker, N. H. (2011) The burning rate of energetic films of nanostructured porous silicon, *small*, 7, pp3392–3398.
98. Becker, C. R., Gillen, G. J., Staymates, M. E., and Stoldt, C. R. (2015) Nanoporous Silicon Combustion: Observation of Shock Wave and Flame Synthesis of Nanoparticle Silica, *ACS applied materials & interfaces*, 7, pp25539–25545.
99. Jian, G., Feng, J., Jacob, R. J., Egan, G. C., and Zachariah, M. R. (2013) Super-reactive Nanoenergetic Gas Generators Based on Periodate Salts, *Angewandte Chemie International Edition*, 52, pp9743–9746.
100. Keshavarzi, S., Kronast, W., Lima, F., and Mescheder, U. (2017) Controlled energy release based on explosive porous silicon, in *IEEE 30th International Conference on Micro Electro Mechanical Systems (MEMS), 2017*, pp712–715, IEEE.
101. Little, B. K., Emery, S. B., and Lindsay, C. M. (2015) Physiochemical characterization of iodine (V) oxide Part II: Morphology and crystal structure of particulate films, *Crystals*, 5, pp534–550.
102. Ohkura, Y. (2013) *Synthesis and Optical Ignition of Aluminum and Silicon-based Energetic Materials*, Thesis, Stanford University.
103. Parimi, V. S. (2015) *Characterization Of Porous Silicon For Micropyrotechnic Applications*, Thesis, Pennsylvania State University.
104. Parimi, V. S., Huang, S., and Zheng, X. (2017) Enhancing ignition and combustion of micron-sized aluminum by adding porous silicon, *Proceedings of the Combustion Institute*, 36, pp2317–2324.

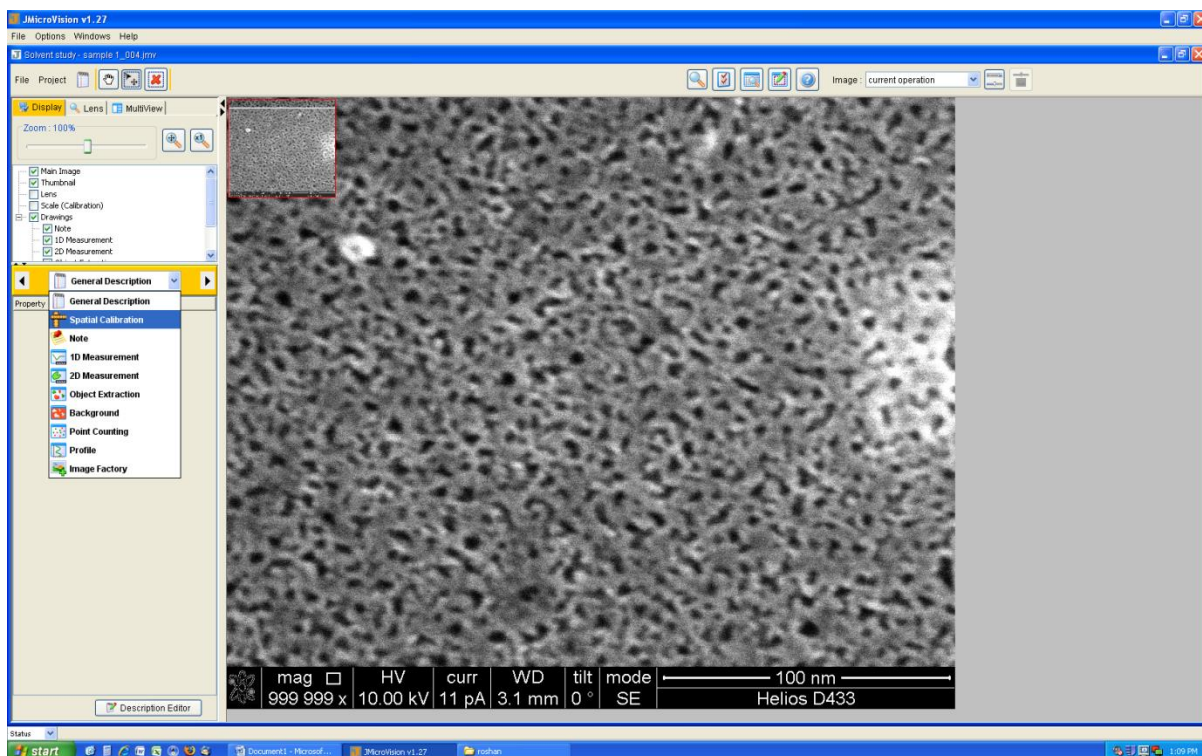
105. Piekiele, N., Churaman, W., Morris, C., and Lunking, D. (2014) Characterization of Patterened Galvanic Porous Silicon for On-Chip Combustion, in *52nd Aerospace Sciences Meeting*, p0817.
106. Piekiele, N. W., and Morris, C. J. (2015) Small-scale, self-propagating combustion realized with on-chip porous silicon, *ACS applied materials & interfaces*, 7, pp9889–9897.
107. Piekiele, N. W., Morris, C. J., Churaman, W. A., and Lunking, D. M. (2015) Exploring the Length Scale Limits of Porous Silicon Combustion, in *MRS Proceedings*, p1758, Cambridge Univ Press.
108. Sinha, S., Piekiele, N. W., Smith, G. L., and Morris, C. J. (2017) Investigating aging effects for porous silicon energetic materials, *Combustion and Flame* 181, pp164–171.
109. Zhao, G., and Lu, M. (2013) Crystal structures, infrared spectra, thermal stabilities and burning properties of RDX derivatives: A computational study, *Computational and Theoretical Chemistry*, 1018, pp13–18.
110. Zheng, X. (2013) *Characterization of Ignition and Combustion Properties of Nanowire-based Energetics*, DTIC Document W911NF-10-1-0106.
111. Zhou, X., Xu, D., Yang, G., Zhang, Q., Shen, J., Lu, J., and Zhang, K. (2014) Highly exothermic and superhydrophobic Mg/fluorocarbon core/shell nanoenergetic arrays, *ACS applied materials & interfaces*, 6, pp10497–10505.
112. Canham, L. (2014) Porous Silicon Membranes, in *Handbook of Porous Silicon* (Canham, L. Ed.), pp163–170, Springer.
113. Canham, L. (2014) Tunable Properties Of Porous Silicon, in *Handbook of Porous Silicon* (Canham, L. Ed.), pp201–206, Springer.
114. Plessis, M. du. (2016) Porous silicon-based explosive devices, in *Porous Silicon: from formation to application* (Korotcenkov, G., Ed.), pp387–401, CRC Press.
115. Plessis, M. du. (2014) Energetics with Porous Silicon, in *Handbook of Porous Silicon* (Canham, L. Ed.), pp975–983, Springer.
116. Zhou, X., Torabi, M., Lu, J., Shen, R., and Zhang, K. (2014) Nanostructured energetic composites: synthesis, ignition/combustion modeling, and applications, *ACS applied materials & interfaces*, 6, pp3058–3074.
117. Plummer, A., Kuznetsov, V., Gascooke, J., Shapter, J., and Voelcker, N. (2014) Laser shock ignition of porous silicon based nano-energetic films, *Journal of Applied Physics*, 116, pp054912-1 to 8.
118. *Energetic Materials Testing and Assessment Policy Committee Manual of Tests - Volume 1* (2007), Defence Ordnance Safety Group, Ministry of Defence, London.

119. Talawar, M., Agrawal, A., Anniyappan, M., Wani, D., Bansode, M., and Gore, G. (2006) Primary explosives: Electrostatic discharge initiation, additive effect and its relation to thermal and explosive characteristics, *Journal of hazardous materials*, 137, pp1074–1078.
120. Davis, W. C. (2003) Shock Waves; Rarefaction Waves; Equations of State, in Explosive Effects and Applications (Zukas, J. A., and Walters, W. P., Eds.), pp47–113, Springer, New York.
121. Field, J., Walley, S., Proud, W., Goldrein, H., and Siviour, C. (2004) Review of experimental techniques for high rate deformation and shock studies, *International Journal of Impact Engineering*, 30, pp725–775.
122. Hong, X., Wang, S., Gou, D., Wu, H., Wang, J., Dai, Y., Xia, X., and Xie, Y. (1998) Confining medium and absorptive overlay: their effects on a laser-induced shockwave, *Optics in Lasers and Engineering* 29, pp447–455.
123. Song, H., Wu, X., Huang, C., Wei, Y., and Wang, X. (2012) Measurement of fast-changing low velocities by photonic Doppler velocimetry, *Review of Scientific Instruments*, 83, p073301.
124. Wang, J., Weaver, R. L., and Sottos, N. R. (2002) A parametric study of laser induced thin film spallation, *Experimental Mechanics*, 42, pp74–83.
125. Brown, K. E., Shaw, W. L., Zheng, X., and Dlott, D. D. (2012) Simplified laser-driven flyer plates for shock compression science, *Review of Scientific Instruments* 83, pp103901–1 to 13.
126. Kuznetsov, V. A., and Bennetts, S. P. (2013) *Development of Photon Doppler Velocimeter for Explosives Research*, DSTO-TR-2792, Defence Science and Technology Organisation, Edinburgh.
127. Asay, J. (1978) Thick-plate technique for measuring ejecta from shocked surfaces, *Journal of Applied Physics*, 49, pp6173–6175.
128. Boyd, I., Binnie, T., Wilson, J., and Colles, M. (1984) Absorption of infrared radiation in silicon, *Journal of Applied Physics*, 55, pp3061–3063.
129. Mendelejev, V. Y., Skovorodko, S., Lubnin, E., and Prosvirikov, V. (2008) Optical constants of silicon in near infrared region, *Applied Physics Letters* 93, pp131916-1 to 3.
130. Vinikman-Pinhasi, S., and Ribak, E. N. (2006) Piezoelectric and piezooptic effects in porous silicon, *Applied physics letters*, 88, pp111905-1 to 2.
131. Lee, K., Lim, C., and Kwon, S. (2006) Propagation of a laser-generated shock wave in a metal confined in water, *Journal of the Korean Physical Society*, 49, pp387–392.

132. Kennedy, J. E. (2003) The Gurney Model of Explosive Output for Driving Metal, in *Explosive Effects and Applications* (Zukas, J. A., and Walters, W. P., Eds.), pp221–257, Springer, New York.
133. Kubota, N. (2007) Propellants and Explosives: Thermochemical Aspects of Combustion 2nd ed., pp75-126, Wiley-VCH, Weinheim.
134. Mawhinney, D. B., Glass, J. A., and Yates, J. T. (1997) FTIR study of the oxidation of porous silicon, *The Journal of Physical Chemistry B*, 101, pp1202–1206.
135. Air - compressed gasses data sheet (2015), BOC Australia, www.boc.com.au/shop/en/au-boc-industrial-store/air--instrument-grade--compressed, accessed 06/04/2016.
136. Ritzhaupt, G., and Devlin, J. P. (1975) Infrared spectra of matrix isolated alkali metal perchlorate ion pairs, *The Journal of Chemical Physics*, 62, pp1982–1986.
137. Scardera, G., Puzzer, T., Conibeer, G., and Green, M. A. (2008) Fourier transform infrared spectroscopy of annealed silicon-rich silicon nitride thin films, *Journal of Applied Physics* 104, pp104310-1 to 7.
138. Kim, Y.-H., Hwang, M. S., Kim, H. J., Kim, J. Y., and Lee, Y. (2001) Infrared spectroscopy study of low-dielectric-constant fluorine-incorporated and carbon-incorporated silicon oxide films, *Journal of Applied Physics*, 90, pp3367–3370.
139. Guber, A., and Köhler, U. (1995) FTIR spectroscopy for the analysis of selected exhaust gas flows in silicon technology, *Journal of molecular structure*, 348, pp209–212.
140. Hoshino, M., Kimachi, Y., and Terada, A. (1996) Thermogravimetric behavior of perfluoropolyether, *Journal of applied polymer science*, 62, pp207–215.
141. Plummer, A., Kuznetsov, V. A., Gascooke, J. R., Shapter, J., and Voelcker, N. H. (2017) Combined thermal and FTIR analysis of porous silicon based nano-energetic films, *RSC Adv.*, 7, pp7338–7345.
142. Devlin, D. J., and Herley, P. J. (1987) Thermal decomposition and dehydration of sodium perchlorate monohydrate, *Reactivity of solids*, 3, pp75–84.
143. Venkatachalam, S., Santhosh, G., and Ninan Ninan, K. (2004) An overview on the synthetic routes and properties of ammonium dinitramide (ADN) and other dinitramide salts, *Propellants, Explosives, Pyrotechnics*, 29, pp178–187.
144. Agrawal, J. P., and Hodgson, R. D. (2007) *Organic Chemistry of Explosives*, 273–275, John Wiley and Sons, Chichester, West Sussex.

Appendix A. CALCULATION OF PORE SIZE DISTRIBUTION FROM SEM IMAGES

Pore size distributions for pSi are determined from planar SEM images using JMicroVision image analysis software. Spatial calibration of the SEM image is determined from the scale bar embedded into the image. The software can then automatically determine the edge of individual pores on the basis of pixel contrast thresholds set by the user.



Pores in electrochemically etched pSi exist with a range of different sizes and shapes. In order to obtain a representative pore diameter suitable for comparison, the software will infer that the measured perimeter for each individual pore is the circumference of an assumed circular pore, thereby enabling the calculation of the equivalent circular diameter (ECD) of that pore. Applying this analysis over the whole image generates an ECD population of 600 – 700 individual pores per image. The extracted data set was then processed using Microsoft Excel to obtain both the mean and standard deviation of the pore sizes, and a histogram of the pore size distribution at 1 nm resolution.

Appendix B. DETAILED CORRELATION BETWEEN DSC AND 2D FTIR DATA

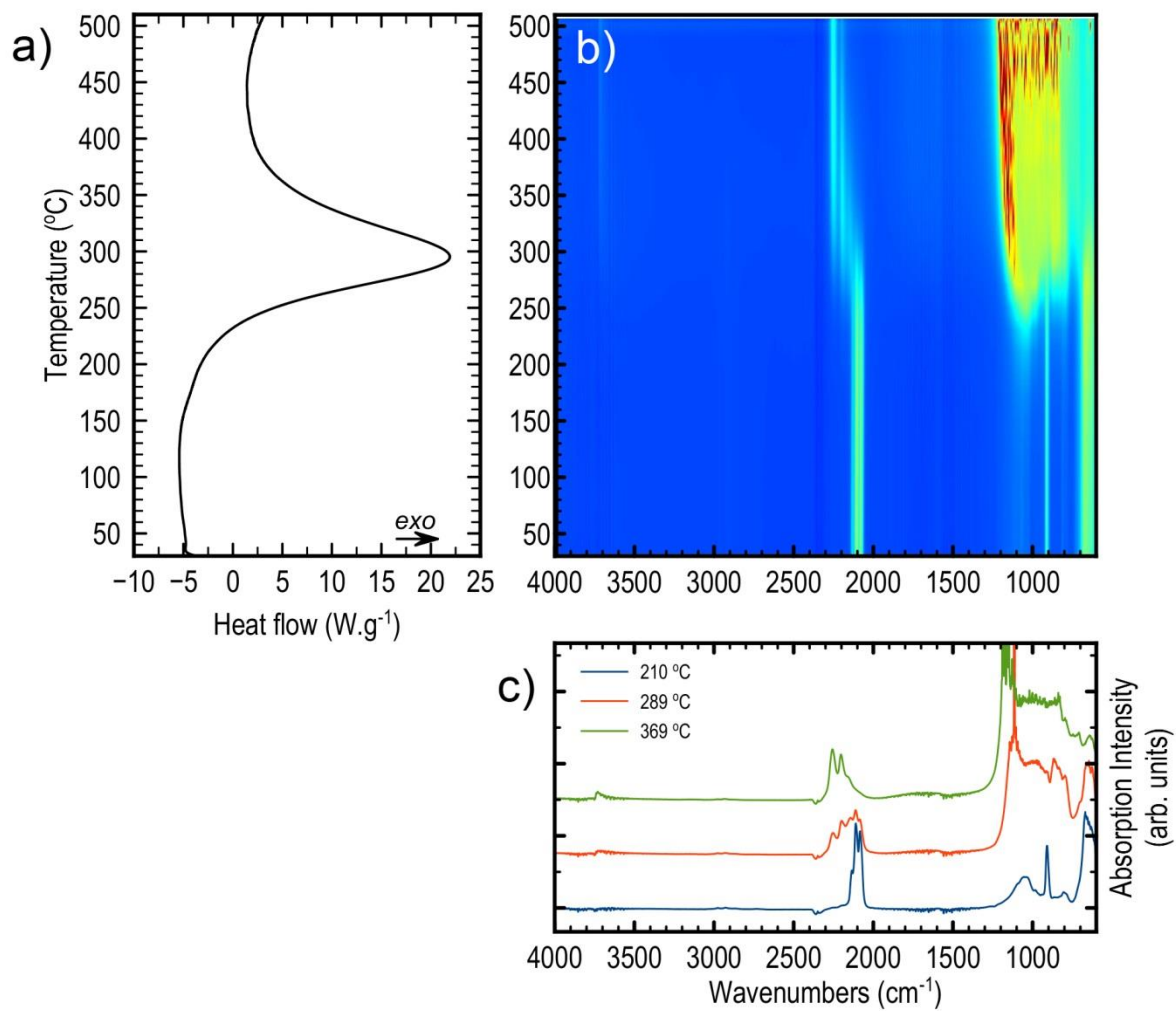


Figure B-1: Correlated 1D and 2D FTIR and DSC thermographs - blank pSi in air.

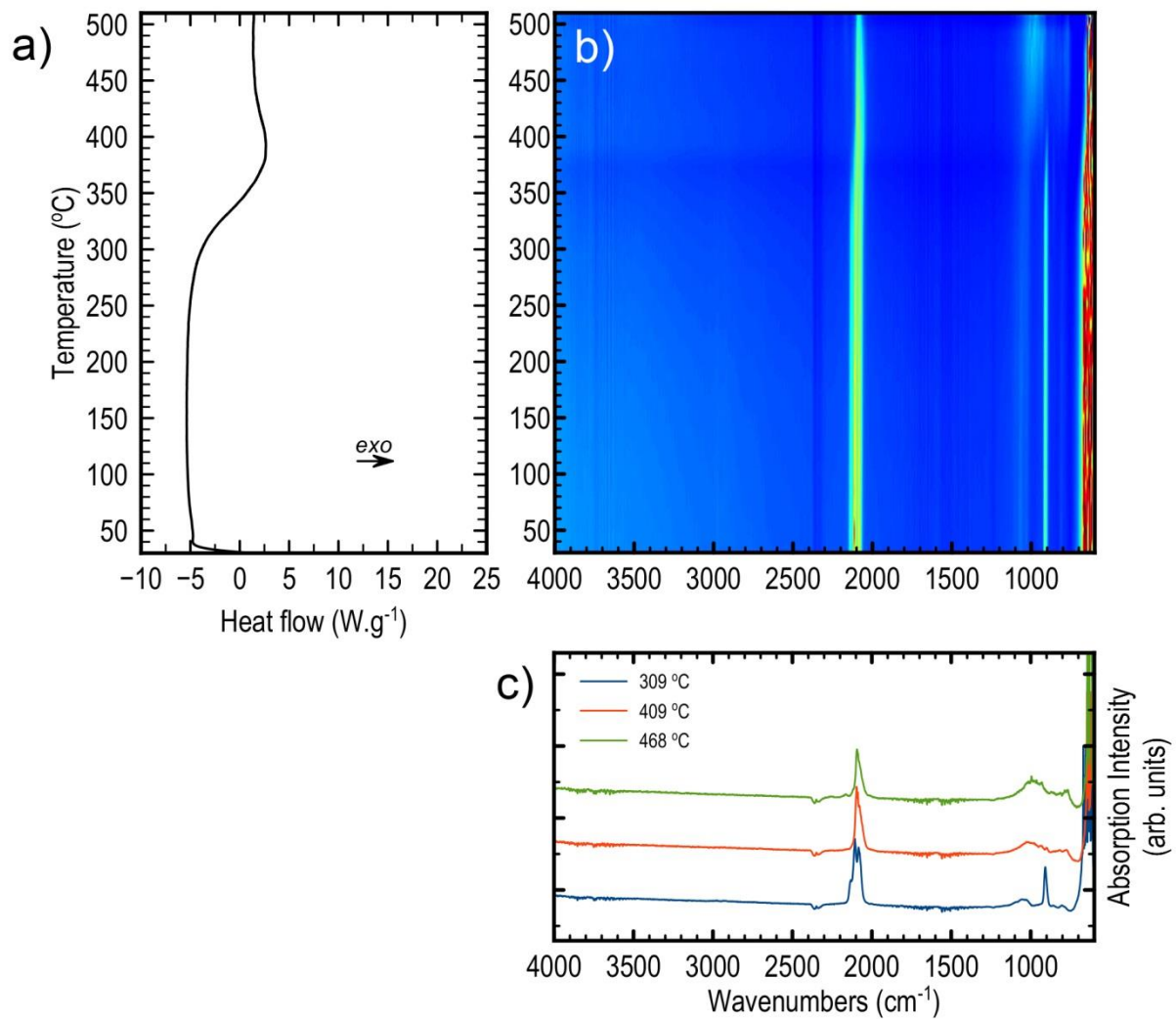


Figure B-2: Correlated 1D and 2D FTIR and DSC thermographs - Blank pSi in N₂.

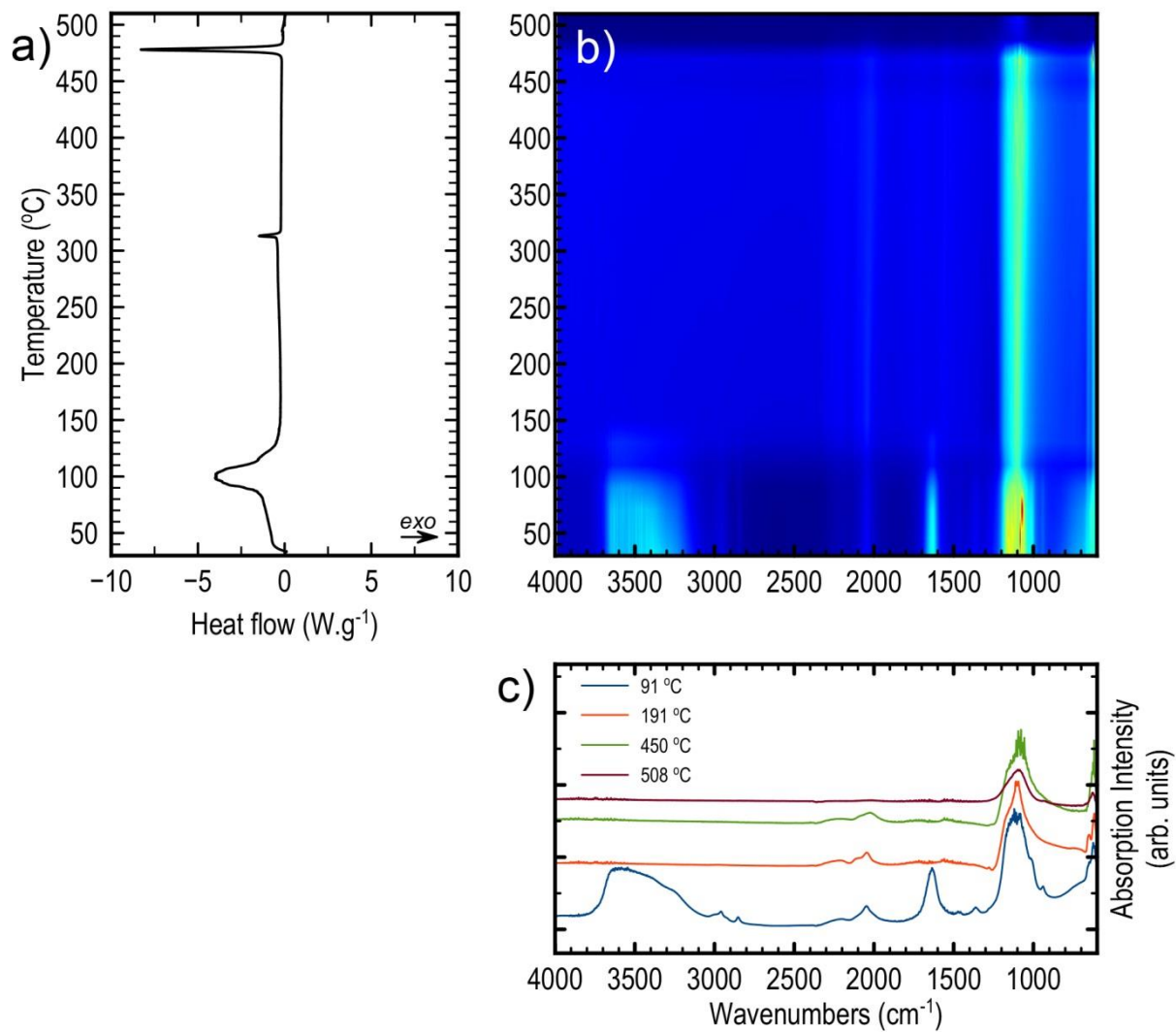


Figure B-3: Correlated 1D and 2D FTIR and DSC thermographs - blank SP in N₂.

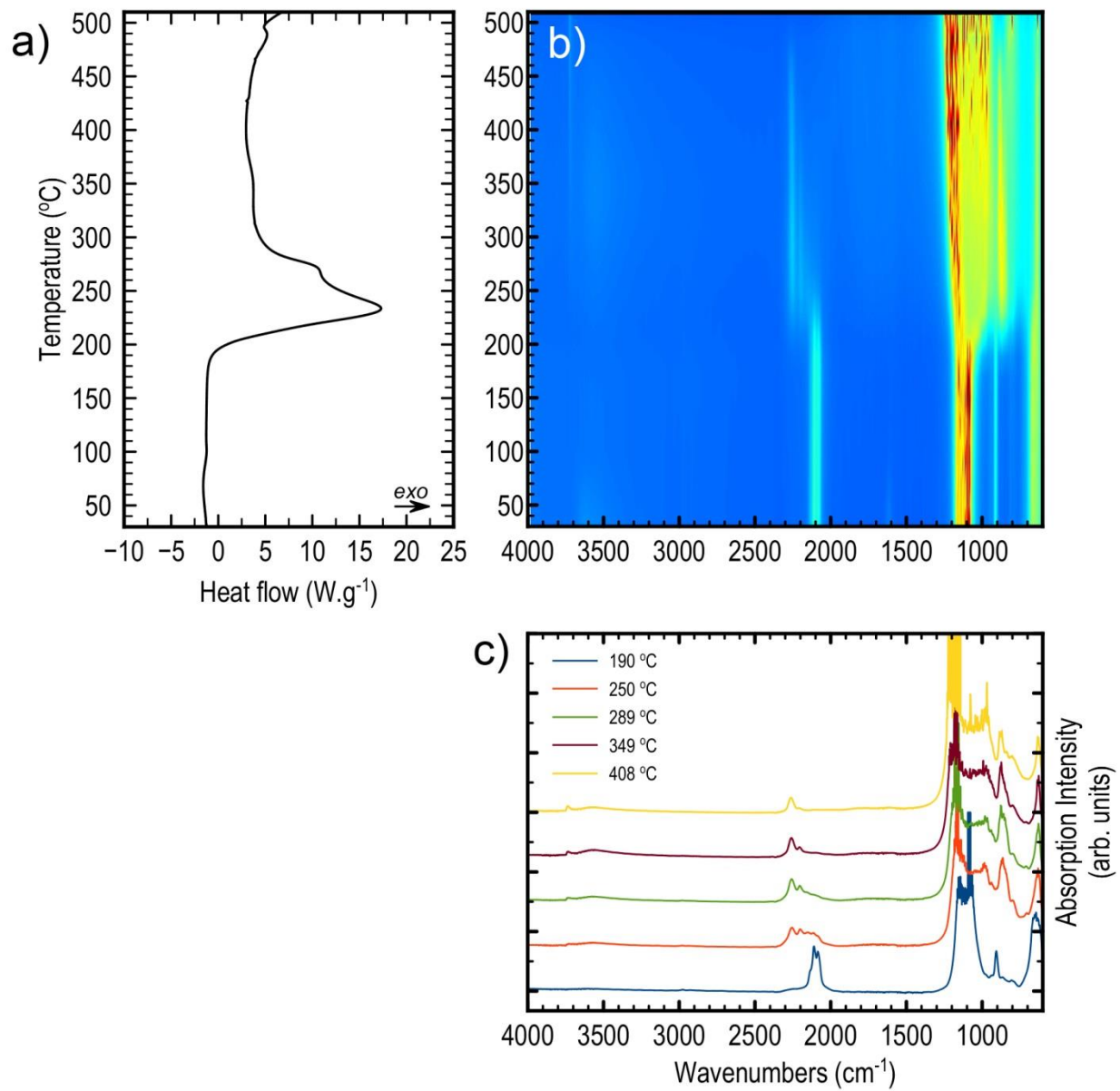


Figure B-4: Correlated 1D and 2D FTIR and DSC thermographs - pSi / SP energetic material in air.

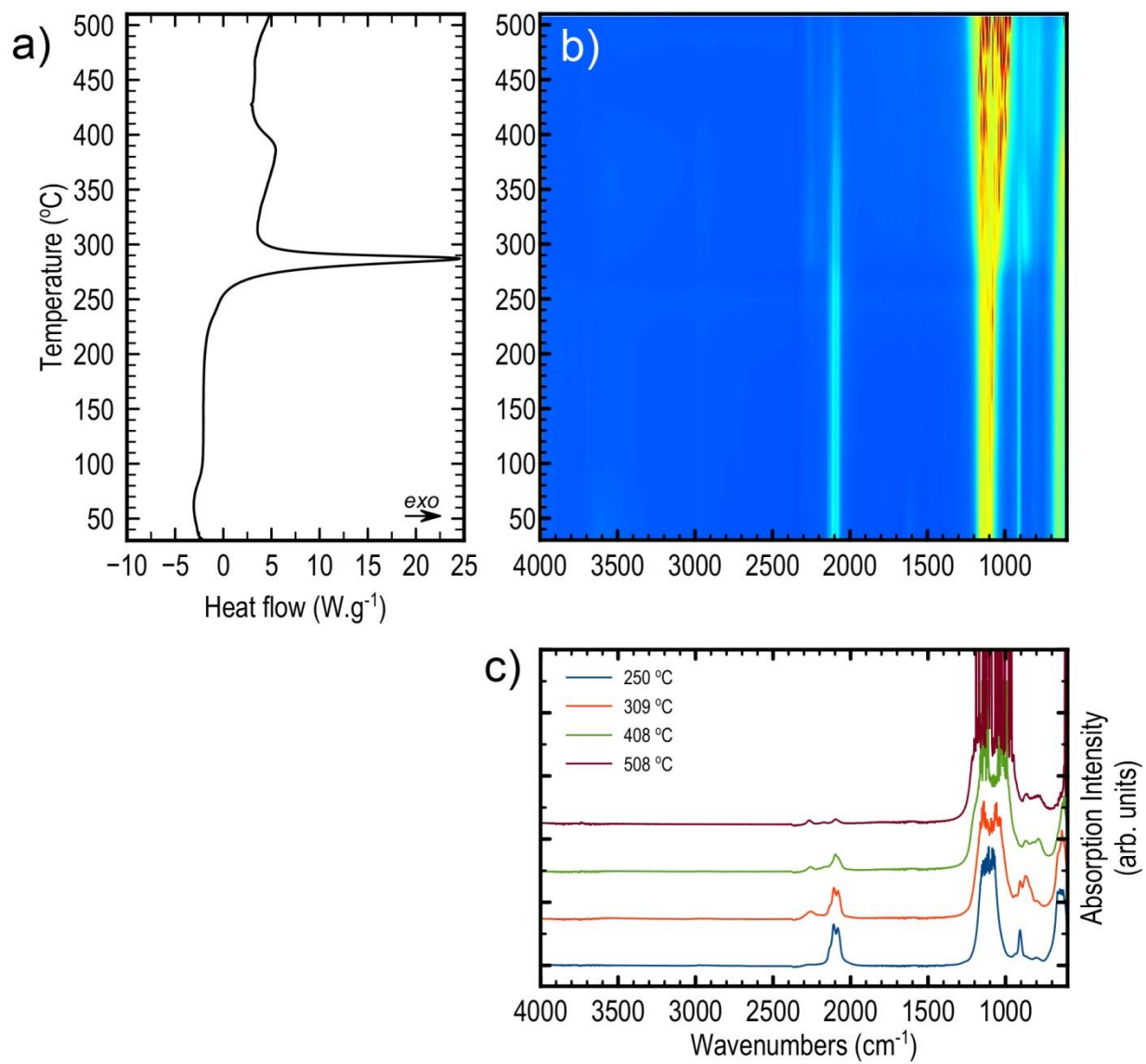


Figure B-5: Correlated 1D and 2D FTIR and DSC thermographs - pSi / SP energetic material in N_2 .

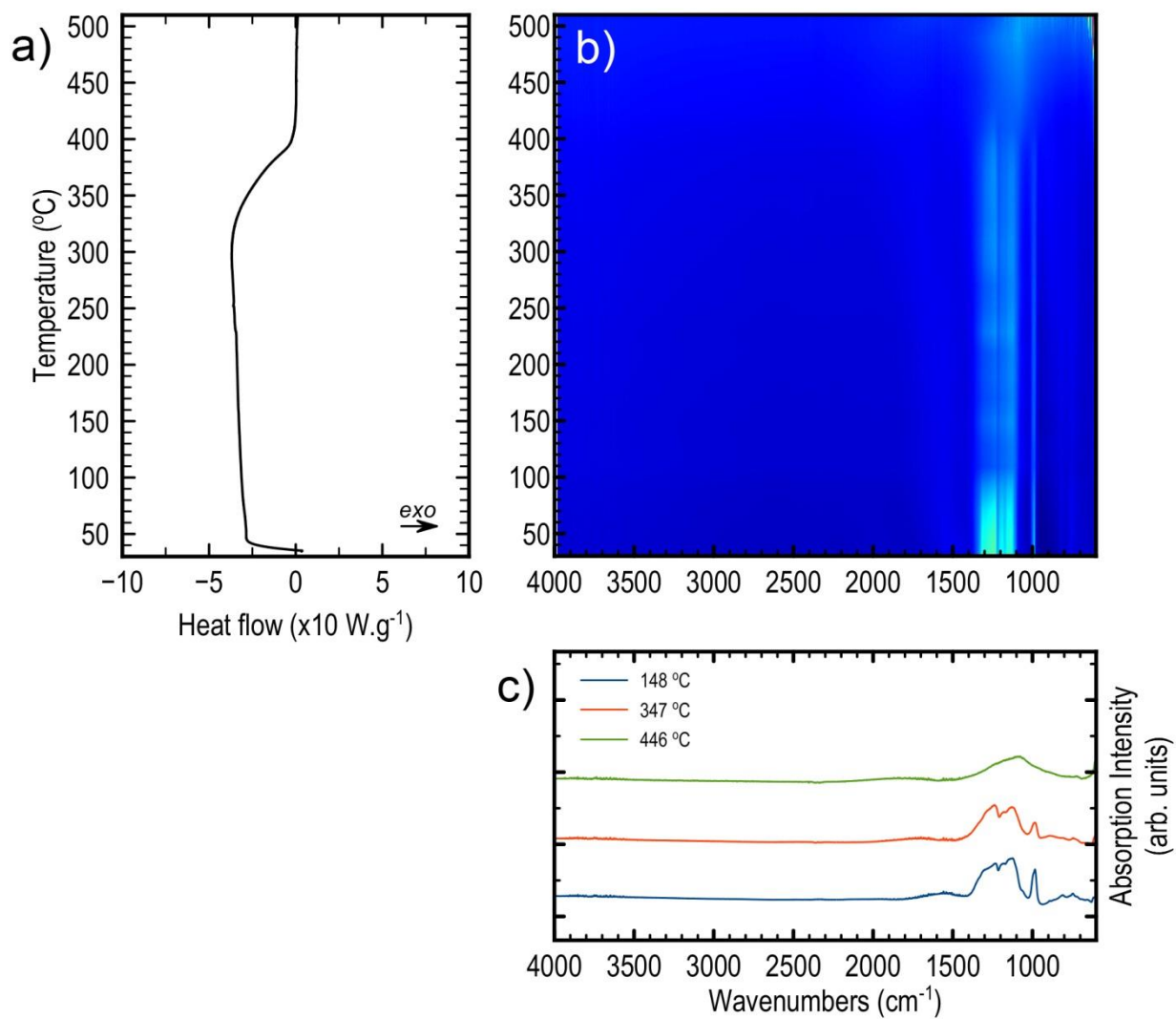


Figure B-6: Correlated 1D and 2D FTIR and DSC thermographs - blank PFPE in N₂.

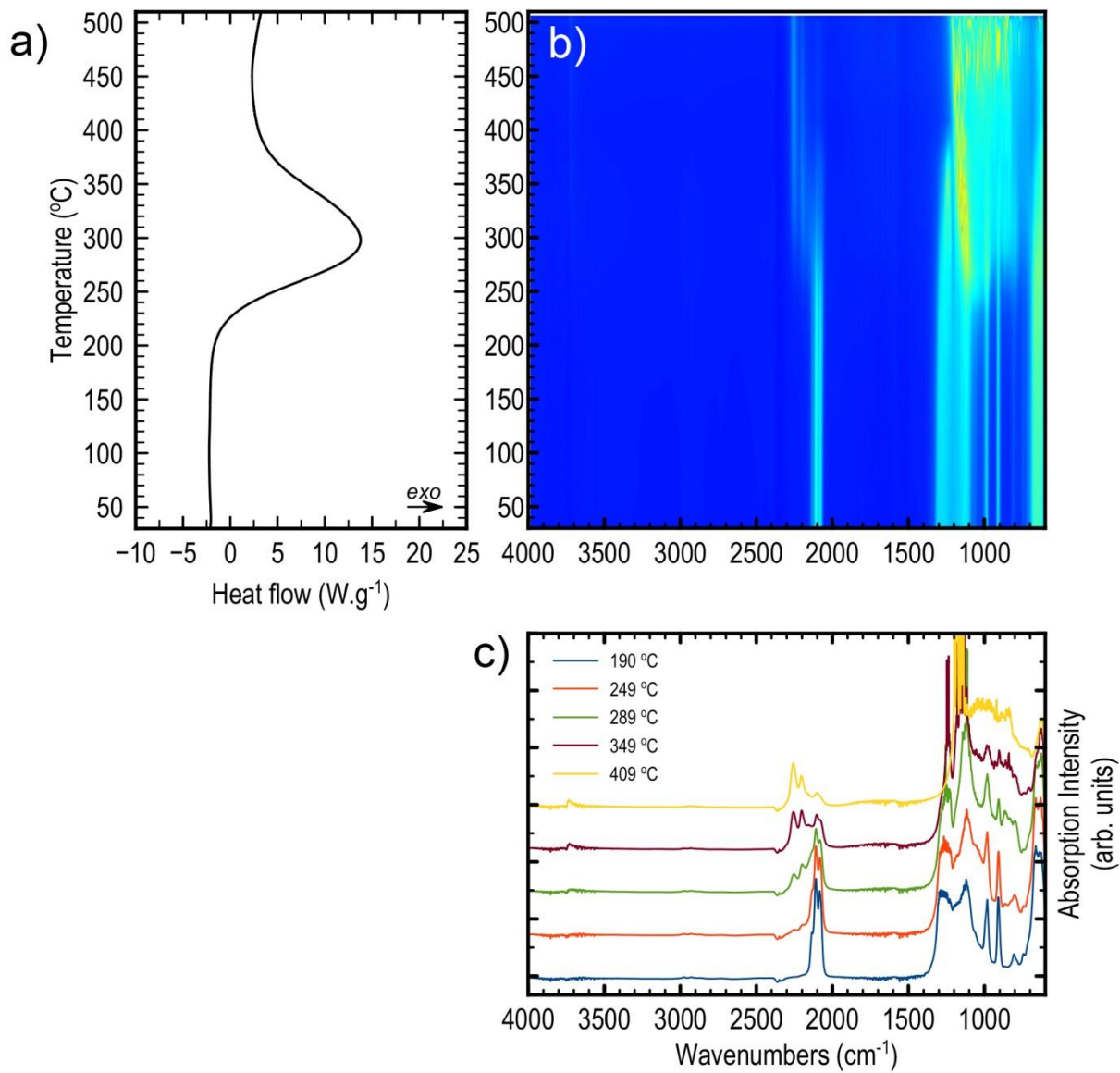


Figure B-7: Correlated 1D and 2D FTIR and DSC thermographs - pSi / PFPE energetic material in air.

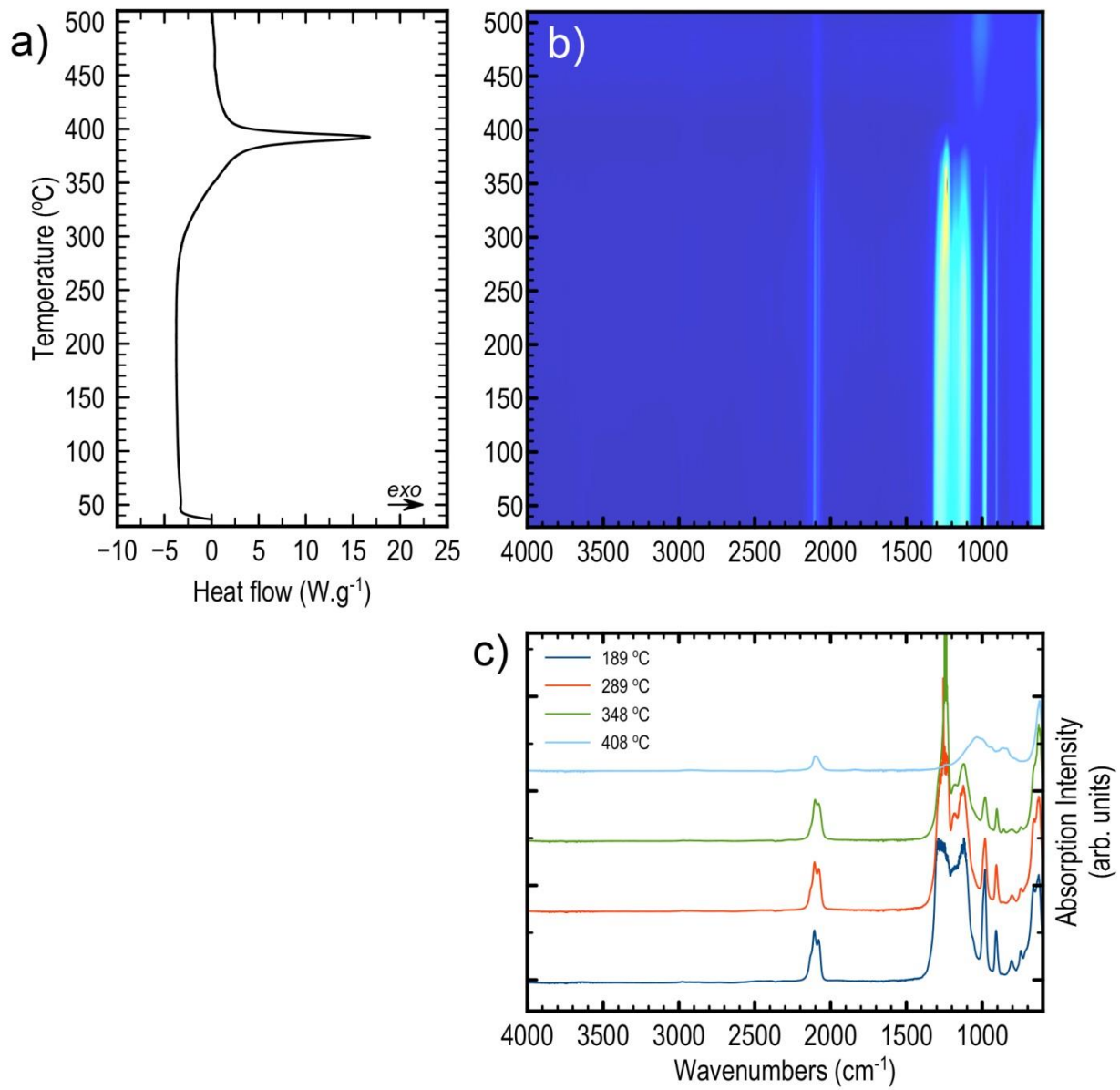


Figure B-8: Correlated 1D and 2D FTIR and DSC thermographs - pSi / PFPE energetic material in N₂.